Development of heterogeneously integrated photodiodes on silicon nitride, segmented waveguide photodiodes, and zero-bias photodiodes

A Dissertation

Presented to
the Faculty of the School of Engineering and Applied Science
University of Virginia

In Partial Fulfillment of the
Requirements for the Degree of
Doctor of Philosophy

By

Qianhuan Yu

March 2020

This dissertation is dedicated

to my parents, my wife and myself

Abstract

Photodiodes are being used in numerous applications nowadays. Depending on their use, photodiodes require various designs and optimization goals. In my work, I focus on photodiode developments for silicon photonics, integrated quantum optics, and microwave photonics. My work includes design, fabrication, and characterization of different structures based on these applications' requirements.

Starting with silicon photonics, I have developed a new die bonding process based on a very thin adhesive layer (SU-8). This technique enabled designs to achieve high-performance waveguide photodiodes on a silicon photonics platform. Using this technique, I developed record-high responsivity PIN photodiodes on silicon nitride waveguides. By further optimizing the epitaxial layer structure, the bonding, and the fabrication process, I was able to demonstrate a waveguide photodiode with 20 GHz bandwidth and even higher responsivity. Low dark current and a record-high quantum efficiency were achieved in single and balanced photodiodes. These photodiodes are promising candidates for high-speed Si_3N_4 photonic integrated circuit applications.

For integrated quantum optics, I developed a novel segmented waveguide photodetector based on a directional coupler design. By matching the imaginary parts of the propagation constants of the even and odd modes in the design, an integrated optical detector with near-unity quantum efficiency is achieved. This work represents a new approach for integrated photon number resolving (PNR) detectors.

Finally, bias-free photodiodes are required to reduce the power consumption and electrical cross-talk in data center applications. I demonstrated a bias-free photodiode with 40 GHz bandwidth and a record-high output power.

Acknowledgement

This dissertation is a summary work of all my research work in University of Virginia. During my study here, I've met great people around and I want to express my deepest gratitude to them.

First one definitely should be my advisor Andreas Beling. Without his support of my Ph.D. study and related research, I cannot finish my degree smoothly. His guidance helped me all of the time through my research and writing this thesis. What impressed me most is his rigorous scientific style on everything about research. I could not have imagined having a better advisor for my Ph.D. study ever.

Besides my advisor, I would like to thank the rest of my thesis committees: Prof. Joe C. Campbell, Prof. Olivier Pfister, Prof. Robert M. Weikle and Prof. Steven M. Bowers for their insightful comments and encouragement during my Ph.D. proposal. Especially for Joe, he is very nice and patient during my Ph.D. with sharing his knowledge and perceptive suggestions to my research. Moreover, I also appreciate Prof. Weikle for sharing the wafer bonding tool for my research. It is really a memorable experience to have collaborated with his research group.

I feel grateful to our group members: Keye Sun, Fengxin Yu, Ta-ching Tzu, Junyi Gao, Jesse Morgan, Nan Ye, Ze Wang, Zhanyu Yang, Ye Wang, Yang Shen, Xingjun Xue, Yiwei Peng, Andrew Jones, Min Ren, Qinglong Li, Yaojia Chen, Yuan Yuan, Xiaojun Xie and Jiyuan Zheng. They have given me los of suggestions during my research. I also really appreciate Linli Xie and Souheil Nadri from Prof. Weikle group for their useful suggestions during my own research.

Last, but not least, I would thank to my family: my father Ming Yu, my mother Liping Tian and my wife Qi Tang for supporting me spiritually through all my Ph.D. and my life in general.

Qianhuan Yu

Table of Contents

Chapter 1. Introduction

Photodiodes, being a ubiquitous technology, are being used in numerous applications such as optical communication systems, data centers, microwave photonics, and sensing [1.1-1.8]. The function of a semiconductor photodiode is to convert optical signals into electrical signals [1.9-1.12]. In digital optical networks, a high-bandwidth and a high-sensitivity photodiode is desirable [1.13]. In analog optical links, photodiodes that can handle high power are required [1.14]. A potential future application is quantum computing, in which it is crucial to have a high-quantum efficiency photodiode [1.15]. The power efficiency is needed to be further improved in data centers [1.16]. In silicon photonics, high-performance photodiodes are generally desired to move this promising technology forward [1.17]. Not any photodiode can meet all the requirements for all the applications at the same time, and hence, optimized designs are necessary depending on the various applications.

My research centers around high-performance heterogeneously integrated photodetectors. In my work, I developed a mature SU-8 wafer bonding process for heterogeneously integrated III-V photodiodes on silicon and silicon nitride platforms. I successfully designed, fabricated, and characterized photodiodes on silicon nitride with record-high efficiency which can be applied in a chip-scale frequency synthesizer [1.18]. I also designed and fabricated a novel segmented waveguide photodetector with high quantum efficiency. This device can potentially be used as in a novel photon number resolving (PNR) system [1.15]. In my work, I also demonstrated a zero-bias photodetector with over 40 GHz bandwidth.

In this thesis, chapter 2 includes the fundamentals of photodiodes and describes figure of merits, various photodiode structures, measurement setups, and fabrication processes. Chapter 3 demonstrates first-generation heterogeneously integrated photodiodes by using SU-8 as a bonding layer. My work verifies the feasibility that SU-8 can be used as a bonding medium for integration. In chapter 4, I discuss the optimization of the bonding process for photonic integration in order to achieve stable and thin bonding layers. Using the optimized process, chapter 5 describes photodiodes on silicon nitride waveguides with record-high responsivities and high bandwidth. Chapter 6 reports on the results of a novel segmented waveguide photodetector. Its near-unity quantum efficiency makes the device a promising candidate for integrated optical detectors that require very high efficiency. This chapter also includes the design of a segmented waveguide photodetector based on avalanche photodiodes that has potential applications in photon number resolving systems. Chapter 7 presents a bias-free photodiode with 40 GHz bandwidth achieving record-high output power for photodiodes working at zero bias in this frequency. The dissertation summary and future work are presented in chapter 8.

References

[1.1] D. R. Smith, R. C. Hooper, P. P. Smyth and D. Wake, “Experimental comparison of a germanium avalanche photodiode and InGaAs PINFET receiver for longer wavelength optical communication systems,” Electronics Letters, vol. 18, pp. 453-454, 1982.

[1.2] H. Yang, N. Ye, R. Phelan, J. O'Carroll, B. Kelly, W. Han, X. Wang, N. Nudds, N. MacSuibhne, F. Gunning, P. O'Brien, FH. Peters, B Corbett, “Butterfly packaged high-speed and low leakage InGaAs quantum well photodiode for 2000nm wavelength systems,” Electronics Letters, vol. 49, pp. 281-282, 2013.

[1.3] X. Xie, K. Li, Y. Shen, Q. Li, J. Zang, A. Beling, J. C Campbell, “Photonic generation of high-power pulsed microwave signals,” IEEE Journal of Lightwave Technology, vol. 33, pp. 3808-3814, 2015.

[1.4] X. Xie, Q. Zhou, K. Li, Y. Shen, Q. Li, Z. Yang, A. Beling, J. C Campbell, “Improved power conversion efficiency in high-performance photodiodes by flip-chip bonding on diamond,” Optica, vol. 1, pp. 429-435, 2014.

[1.5] B. Andreas, X. Xie, and J. C. Campbell. "High-power, high-linearity photodiodes." Optica 3, no. 3 (2016): 328-338.

[1.6] R. H. Hadfield, “Single-photon detectors for optical quantum information applications,” Nature Photonics, vol. 3, pp. 696–705, 2009.

[1.7] G. L. Mansell, T. G. McRae, P. A. Altin, M. J. Yap, R. L. Ward, B. J. J. Slagmolen, D. A. Shaddock, and D. E. McClelland, “Observation of squeezed light in the 2 um region,” Physical Review Letter, vol. 120, pp. 203603, 2018.

[1.8] M. Piels, J. E. Bowers. "Photodetectors for silicon photonic integrated circuits." In Photodetectors, pp. 3-20. Woodhead Publishing, 2016.

[1.9] J. C. Campbell, A. G. Dentai, W. S. Holden, and B. L. Kasper, “High-performance avalanche photodiode with separate absorption ‘grading’ and multiplication regions,” Electronics Letters, vol. 19, pp. 818-820, 1983.

[1.10] E. Kim, A. Madhukar, Z. Ye, and J. C. Campbell, “High detectivity InAs quantum dot infrared photodetectors,” Applied Physics Letters, vol. 84, pp. 3277, 2004.

[1.11] Z. Huang, J. E. Carey, M. Liu, X. Guo, E. Mazur, and J. C. Campbell, “Microstructured silicon photodetector,” Applied Physics Letters, vol. 89, pp. 033506, 2006.

[1.12] A. Wakatsuki, T. Furuta, Y. Muramoto and T. Ishibashia, “High-speed photodiode and optical receiver technologies,” OFC 2009, paper OMK1, 2009.

[1.13] D. Lavery, T. Gerard, S. Erkilinç, Z. Liu, L. Galdino, P. Bayvel, and R. I. Killey. "Opportunities for optical access network transceivers beyond OOK." IEEE/OSA Journal of Optical Communications and Networking 11, no. 2 (2019): A186-A195.

[1.14] Z. Yang, Q. Yu, X. Xie, P. Yao, C. Schuetz, J. C. Campbell, and A. Beling. "High-gain phase modulated analog photonic link using high-power balanced photodiodes." In Optical Fiber Communication Conference, pp. Th1A-5. Optical Society of America, 2017.

[1.15] R. Nehra, C. Chang, Q. Yu, A. Beling, and O. Pfister. "Photon-number-resolving segmented detectors based on single-photon avalanche-photodiodes." Optics Express 28, no. 3 (2020): 3660-3675.

[1.16] T. Umezawa, K. Akahane, N. Yamamoto, A. Kanno and T. Kawanishi. "Bias free operational UTC-PD above 110 GHz and its application to high baud rate fixed-fiber communication and W-band photonic wireless communication", Journal of Lightwave Technology, 2016, 34(13): 3138-3147, 2016.

[1.17] W. Ye, Z. Wang, Q. Yu, X. Xie, T. Posavitz, M. Jacob-Mitos, A. Ramaswamy, E. J. Norberg, G. A. Fish, and A. Beling. "High-power photodiodes with 65 GHz bandwidth heterogeneously integrated onto silicon-on-insulator nano-waveguides." IEEE Journal of Selected Topics in Quantum Electronics 24, no. 2 (2017): 1-6.

[1.18] D. T. Spencer, T. Drake, Travis C. Briles, J. Stone, L. C. Sinclair, C. Fredrick, Q. Li, D. Westly, B.R. llic, A. Bluesone, N. Volet, T. Komljenovic, L. Chang, S. Lee, D. Y. Oh, M. Suh, K. Y. Yang, M. H. P. Pfeiffer, T. J. Kippenberg, E. Norberg, L. Theogarajan, K. Vahala, N. R. Newbury, K. Srinivasan, J. E. Bowers, S. A. Diddams," An optical-frequency synthesizer using integrated photonics," Nature **557**(7703), 81 (2018).

Chapter 2. Photodiode fundamentals

The photodiode is a semiconductor device that converts an optical signal into an electrical current. Typically, photodiodes are PN or PIN structures. When a photon with sufficient energy is absorbed in the diode, an electron-hole pair will be generated. With the help of diffusion and/or drift, holes and electrons will be separated to the anode and cathode, and thus a photocurrent is produced. In this chapter, I will introduce fundamentals of photodiodes including figure of merits, structures, measurement setups, and basic fabrication processes.

2. 1 Photodiode figure of merits

Dark current

Dark current is the electric current that flows through a photodiode when no photons enter the device. Physically, the dark current is due to the random generation of electrons and holes and can be distinguished between bulk and surface dark currents [2.1]. The bulk dark current mainly comes from tunneling, generation-recombination, and diffusion currents [2.2-2.4]. For the surface dark current, the dark current sources can be surface trap-assisted-tunneling, surface diffusion, and surface generation-recombination currents [2.5-2.6]. Among them, trap-assisted-tunneling is related to defects in the material. Therefore, a low dark current indicates good material quality with fewer defects and low surface leakage and is desirable for improving the signal to noise ratio and making the device less susceptible to thermal failure.

Responsivity and quantum efficiency

Responsivity is defined as the ratio of photo-generated photocurrent to the incident optical power [2.7]. It can be expressed as

$$\mathrm{R} = \frac{I_{photo}}{P} = \frac{I_{total}-I_{dark}}{P} \tag{2-1}$$

where P represents the optical power, I_{photo} is the photocurrent which can be derived as the difference between total current and dark current. If the P represents the input optical power, the responsivity is defined as external responsivity. If the P represents the optical power illuminated onto the photodiode, the responsivity is defined as internal responsivity. As the photon energy is related to the optical frequency, another parameter to quantify the efficiency of converting optical power to electrical current is the quantum efficiency. Quantum efficiency can be defined as either external or internal to the device as well. The internal quantum efficiency (IQE) is defined as the number of generated electron-hole pairs to the number of absorbed photons in the device. For external quantum efficiency (EQE), the number of photons refers to the incident beam external to the device. It follows the definition:

$$\eta_{external} = \frac{N_e}{N_p} = \frac{I_p \cdot h\upsilon}{P \cdot q} \tag{2-2}$$

where h is the plank constant, υ is the optical frequency and q is the charge of an electron, N_e and N_p are the number of generated electrons and incident photons. According the definition of responsivity, the external quantum efficiency can be expressed as:

$$\eta_{external} = \mathrm{R} \cdot \frac{h\upsilon}{q} \tag{2-3}$$

100% quantum efficiency corresponds to a responsivity of 1.25 A/W and 0.86 A/W at 1550 nm and 1064 nm, respectively.

Bandwidth

The bandwidth is a parameter quantifying how fast a photodetector response to an optical intensity modulation. Typically, 3-dB bandwidth is defined as the frequency at which the RF power drops by 3 dB below the power at DC. If the device is much shorter than the electrical signal wavelength, the photodetector can be treated as a lumped circuit element. Therefore, the resistance-capacitance (RC)-time constant and carrier transit time are the two primary bandwidth limitations for a photodetector. The bandwidth can be represented by the following equation:

$$f_{3dB} \approx \sqrt{\frac{1}{\frac{1}{f_{RC}^2}+\frac{1}{f_t^2}}} \tag{2-4}$$

where f_{RC} and f_t are the RC-limited and carrier transit time limited bandwidths, respectively.

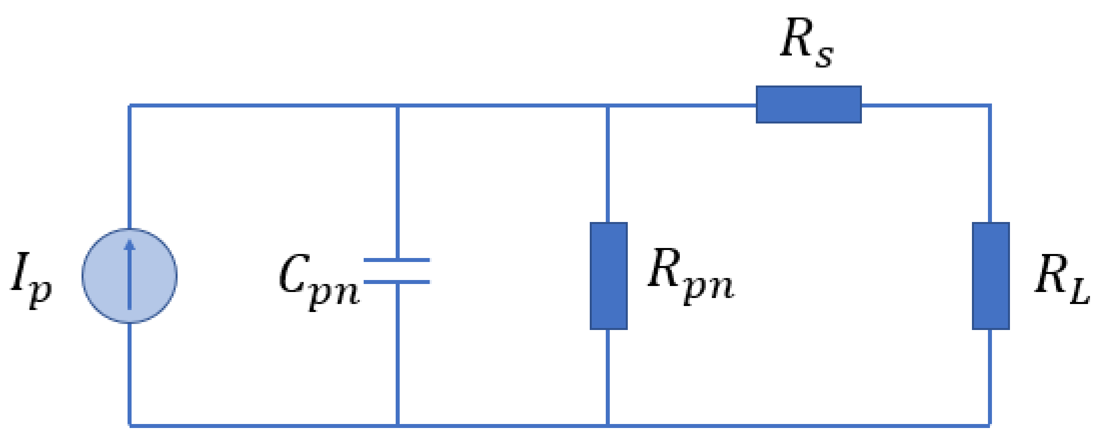

Figure.2-1 Equivalent circuit of a photodiode.

Figure. 2-1 shows the equivalent circuit of a photodiode, where C_{pn}, R_{pn}, R_s, R_L represent the junction capacitance, shunt resistance, series resistance, and load resistance. Then, the RC-limited bandwidth can be expressed as:

$$f_{RC} = \frac{1}{2\pi R_{tot} C_{pn}} \tag{2-5}$$

As the shunt resistance is the photodiode junction resistance, it is typically very large (around 10 MΩ for an InGaAs photodiode) and can be neglected. Here R_{tot} stands for the resistance seen by the junction capacitance which is equal to $R_s + R_L$. C_{pn} is the junction capacitance of the photodiode. For a photodiode with good ohmic contact, R_s typically is several Ohms. The external load resistance R_L normally is 50 Ω which is much larger than R_s. It can be seen that optimizing

R_{tot} to achieve high bandwidth is difficult. In order to improve the RC-limited bandwidth, reducing C_{pn} is more effective.

In eq. (2-4), f_t can be derived as the following equation:

$$f_t \approx \frac{3.5\,\bar{v}}{2\pi d_{abs}} \tag{2-6}$$

where $\bar{v}$ and d_{abs} are the average carrier drift velocity and thickness of the i-layer for a PIN structure. $\bar{v}$ can be calculated as:

$$\bar{v} = \sqrt[4]{2(\frac{1}{v_e^4} + \frac{1}{v_h^4})^{-1}} \tag{2-7}$$

where v_e and v_h are the electron and hole velocities [2.8]. As $C_{pn} \propto 1/d_{abs}$, a thick absorption layer not only provides large responsivity and small junction capacitance but also reduces the carrier transit time limited bandwidth. Consequently, there is a trade-off between these two parameters here. In sum, designing a PIN photodiode with both high bandwidth and high responsivity is challenging in a device where light absorption path and direction of carrier drift are collinear.

<u>RF Power</u>

The RF output power refers to the AC power the photodiode delivers to the load. The photocurrent of a photodiode can be divided into two parts:

$$I_{ph} = I_{DC} + I_{Ac} = I_{avg}(1 + \alpha \cdot \cos(2\pi f t)) \tag{2-8}$$

where I_{avg} is the average DC photocurrent, α is the AC modulation depth on the optical signal and f is the RF signal modulation frequency. By using a bias tee, the AC component can be separated from the DC photocurrent and measured directly by a RF power meter. As shown in Fig. 2-2, the output RF power increases quadratically with increasing optical input power at low input optical power as the dashed line shows in the figure. Since the vertical axial unit is dBm, the quadratic relation appears as a linear curve in the figure. The output RF power will start to deviate from the quadratic trend when the input optical power increases to some level. The output power at which it drops by 1 dB below the ideal power is called 1 dB saturation power. Many factors contribute to this photodiode saturation behavior [2.9-2.10]. Among them, the space charge effect is most important. In order to mitigate the space charge effect, different photodiode structures will be introduced in next section.

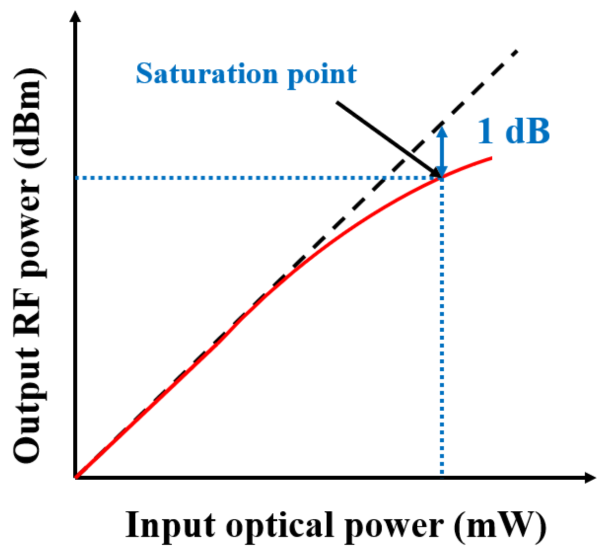

Figure.2-2 Power transfer plot of a typical photodiode showing power compression.

<u>Non-Linearity</u>

The linearity describes the extent to which the output of a system follows linearly with its input without distortion. Linearity performance of a photodiode is crucial to some applications such as analog links, photonic analog-to digital conversion (ADC), and optoelectronic oscillators. Three main physical mechanisms contribute to the linearity performance of a photodiode such as carrier velocity modulation, nonlinear capacitance, and nonlinear responsivity [2.11-2.12].

Figure 2-3 (a) shows the fundamental, second, third, and fourth harmonic signals with a single-tone input to the system. It can be seen that higher order harmonic signals are far away from the fundamental signal, which can be easily filtered out and may not degrade the system performance significantly. Figure 2-3 (b) shows the power spectrum when signals with two close frequencies $f1$ and $f2$ are fed into the system. In the figure 2-3(b), the third-order intermodulation (IMD3) signal lies close to the fundamental signal, which is hard to be filtered by follow-up circuit and seriously degrade the system performance. Therefore, IMD3 power is a crucial parameter when evaluating the device linearity performance. The output third order intercept point (OIP3) is used as a figure of merit to quantify the photodiode linearity performance. The OIP3 is defined as an extrapolation point where the output RF power of the fundamental tone meets the IMD3 power as shown in figure 2-4.

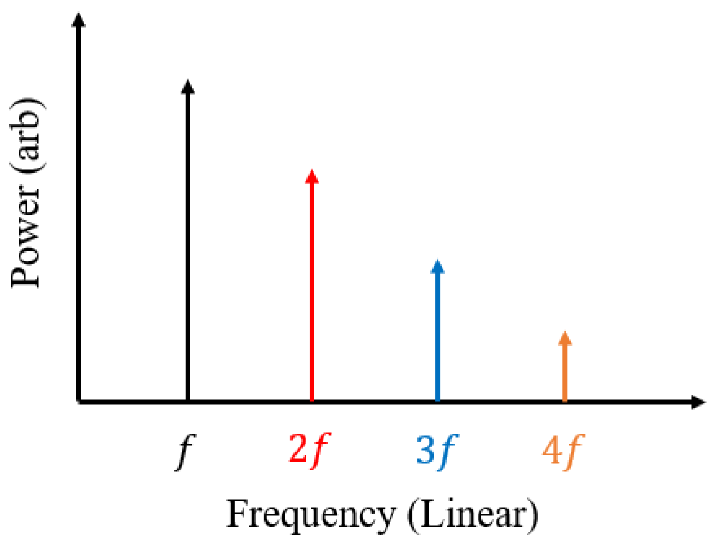

(a)

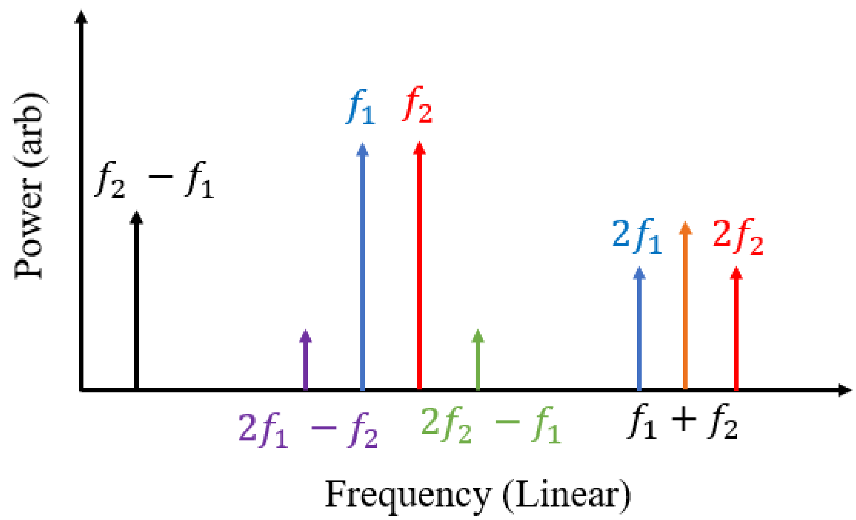

(b)

Figure.2-3 Plots of (a) power spectrum of fundamental, second, third and fourth harmonics signals in a single tone system; (b) power spectrum of fundamental, second and third order intermodulation distortion signals in a two-tone system.

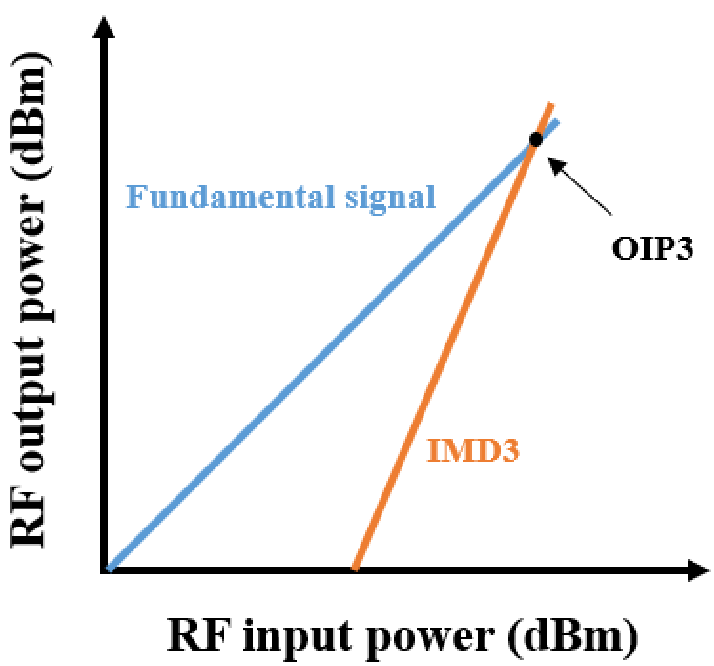

Figure.2-4 OIP3 definition.

2. 2 Photodiode structures

Various photodiode structures have been developed to improve the responsivity, bandwidth, and saturation power of photodiodes. The designs include the PIN structure, uni-traveling carrier (UTC) photodiode, and the modified uni-traveling photodiode (MUTC).

The PIN structure is the simplest design of a photodiode with an intrinsic layer as the absorber as shown in figure 2-5. The photo-generated holes and electrons move to anode and cathode with the help of an electrical field in the intrinsic layer. Both electrons and holes travels inside the device and hole mobility is usually low which leads to lower hole drift velocities. Table 2-1 summarizes carrier mobilities of several materials used in this dissertation. The carrier transit time is mainly limited by hole velocity. According to eq. (2-6) and eq. (2-7), the transit time-limited bandwidth is dominated by the hole velocity for a given thickness of the depletion region. Moreover, there is a trade-off between high responsivity and low bandwidth due to longer carrier transit times in thick absorbers as discussed before.

In terms of the power handling capabilities of photodiodes, the saturation power of PIN photodiodes tends to be low. Figure 2-6 shows the carrier distributions and electrical field profiles in the depletion region both in dark and under light illumination. The orange lines in the plots correspond to the electrical field profile under dark condition. For a PIN structure, an imbalanced carrier distribution in the intrinsic region is caused by different carrier velocities of electrons and holes. As electrons move faster than holes, the field collapses near the N-side. When the field drops to the point that carriers cannot maintain their saturation velocity, the bandwidth decreases and the output power becomes saturated. Therefore, the space charge effect originating from the slow holes limits the PIN structure’s bandwidth and saturation power.

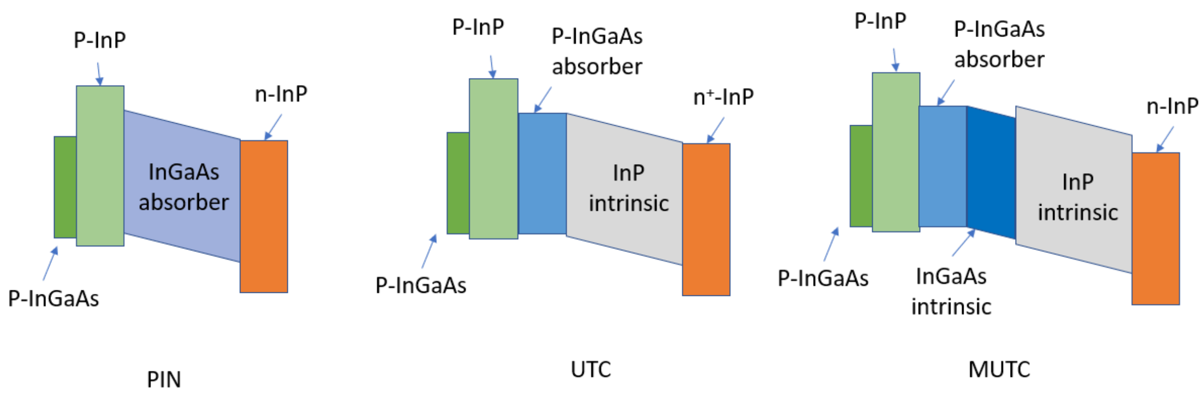

Figure.2-5 InP/InGaAs photodiodes with PIN, UTC, and MUTC structures.

Material	Electron mobility ($m^2/V\cdot s$)	Hole mobility ($m^2/V\cdot s$)
Si	0.14	0.05
InP	0.46	0.015
InGaAs	1	0.3

Table. 2-1 Electron and hole mobilities.

By limiting the optical absorption to P-type doped layers, the UTC structure has achieved higher bandwidths than the PIN structure. Here, the holes generated in the P-type absorber are collected very quickly within the dielectric relaxation time as they are the majority carriers. The electrons generated in the absorber will diffuse into the depletion region. The fast electrons are the only carrier traveling through the depletion region. For an InP/InGaAs-based photodiode, a typical UTC structure is shown in figure 2-5. The depletion region is chosen to be InP instead of InGaAs because InP is transparent in the telecommunication wavelength range and the electron saturation velocity in InP is higher than it is in InGaAs [2.13-2.14]. Moreover, the large-bandgap material InP also helps reducing the dark current. A UTC photodiode with 220 GHz has been demonstrated in ref [2.15]. One remaining issue for the UTC PD is the trade-off between high responsivity and high bandwidth. A high responsivity requires a thick absorber which in turn, significantly reduces the bandwidth due to the slow diffusion of electrons.

In order to further improve the responsivity, a depleted absorber is added to the UTC to form a MUTC as shown in figure 2-5. In the MUTC PD, the space charge effect in the intrinsic InGaAs layer is not significant as long as this layer is thin. This additional depleted absorber is also beneficial to increasing the RC-limited bandwidth since it reduces the junction capacitance. Hence, this design has the potential to simultaneously increase responsivity and bandwidth while preserving high output RF power if all layers are designed carefully. Since the MUTC has more design parameters than PIN and UTC, and the depleted absorber and drift layer can be adjusted separately, it can be better optimized towards specific application requirements.

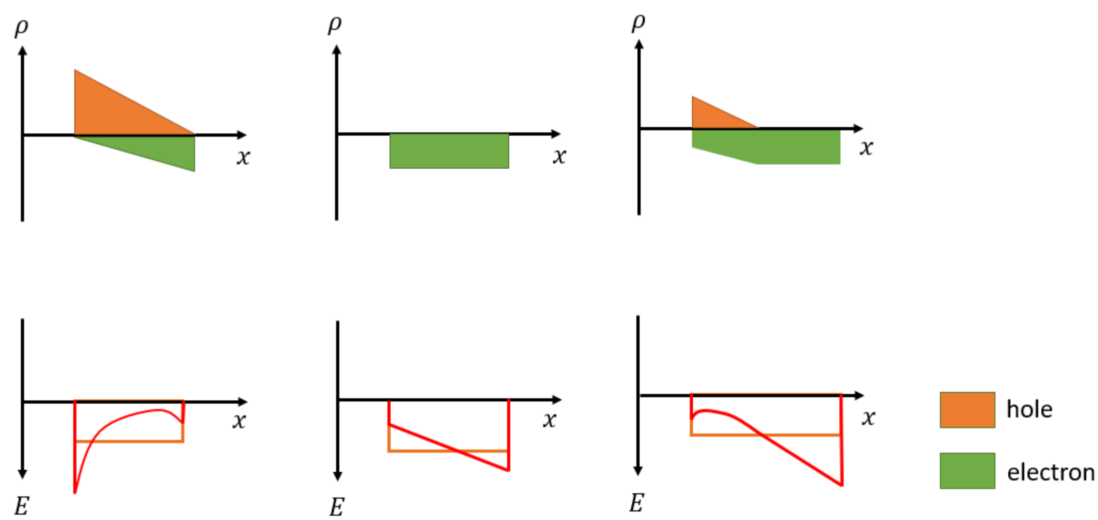

Fig. 2-6 Carrier distributions and electrical fields in depleted regions of PIN, UTC, and MUTC PDs.

2. 3 Photodetector characterization techniques

Current-voltage (I-V) and Capacitance-Voltage (C-V) measurements

In this work I used the HP4145B semiconductor parameter analyzer and on-wafer probe station to measure the photodiode’s current-voltage (I-V) characteristics. The analyzer measures the current while scanning the bias. Typically, dark currents were in the range of 10 nA to 1 μA under 5 V reverse bias for InP/InGaAs-based photodiodes. Moreover, a low series resistance is indicated if the current under forward bias is large. Typically, a photodiode with low resistance can achieve around 1 mA under 0.5 V forward bias. However, this measurement can only reflect whether the resistance is low or not but cannot quantify how much it is. This is because the photodiode is working under reverse bias, which is different from the measurement under forward bias.

I used a HP4275A LCR meter with the same probe station for capacitance-voltage (C-V) measurements by sweeping the bias and measuring the capacitance of the device.

RF response measurement

RF response measurements are carried out using several experimental setups that are described in the following section. This measurement records the output RF power of a photodiode for a modulated input optical signal at different RF frequencies. Therefore, one crucial part is to generate a calibrated modulated optical signal. In my work, the RF-modulated optical signal is generated either by a heterodyne setup with two lasers, or an optical modulator.

Optical heterodyning is a powerful method due to its wide modulation range. The setup is shown in figure 2-7. It includes two lasers with slightly different wavelength outputs that are superimposed to generate a beat signal. By adjusting one of the laser's wavelength, the modulation frequency can be tuned over a wide range. The optical signal is split into two branches. One branch is used for monitoring the beat frequency. For beat frequencies less than 50 GHz, I used a commercial photodetector followed by an electrical spectrum analyzer (ESA). For beat frequencies higher than 50 GHz (wavelength difference is larger than 0.4 nm), the beat frequency can be calculated by the wavelength difference measured by a wavelength meter. The other branch of the optical signal is amplified by an erbium-doped fiber amplifier (EDFA) and the output power is adjusted by an optical digital attenuator before reaching the device under test (DUT). With the help of a bias tee, the RF power is read out through an RF power meter. One advantage of the heterodyne setup is that it can reach 100% modulation depth by adjusting the powers and polarizations of lasers I and II. Optical signals with 100% modulation depth are also helpful for measuring the saturation performance of photodiode as it offers large-signal input optical power.

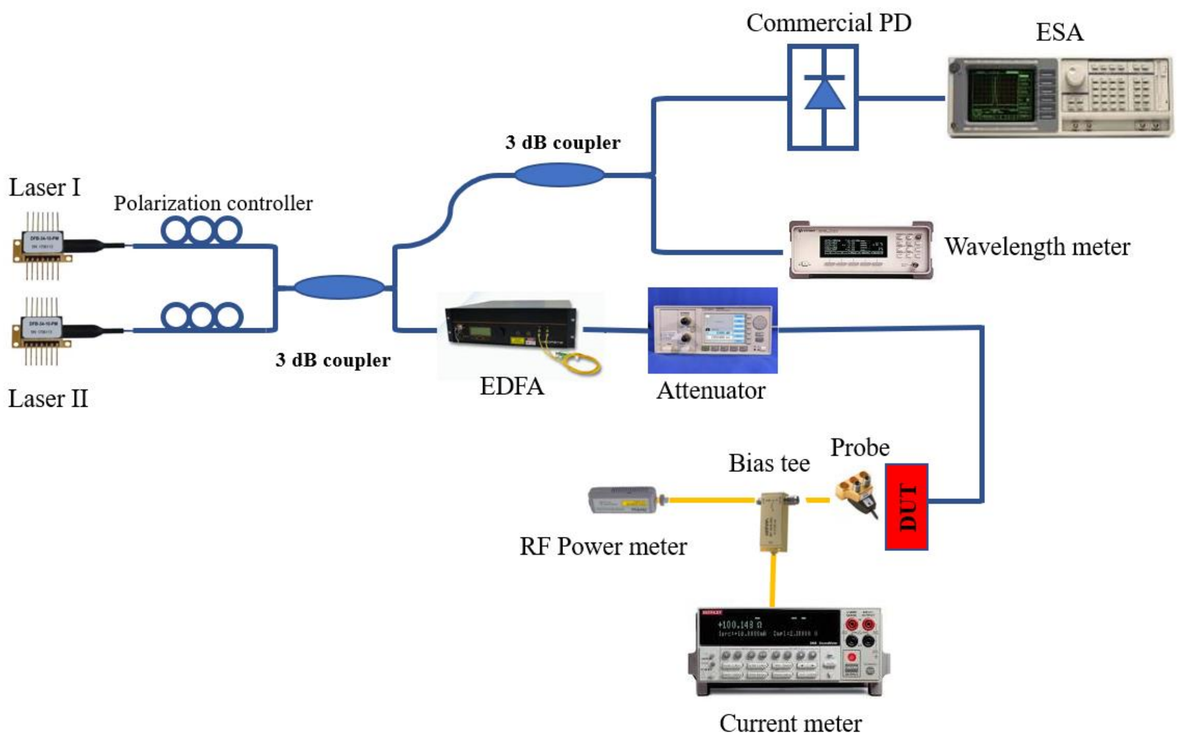

Fig. 2-7 Heterodyne setup for characterizing photodiode bandwidth.

Photodetector bandwidth can also be measured by using an optical modulator as shown in figure 2-8. The CW optical signal coming from the laser is modulated by a commercial optical intensity modulator driven by a signal generator. This method is somewhat simpler compared to the heterodyne setup but the modulator frequency response needs to be calibrated in order to de-embed its influence on the measured bandwidth. This setup has a clean electrical signal spectrum on the ESA, which makes it, together with the low noise floor of the ESA, an ideal measurement for small-signal response.

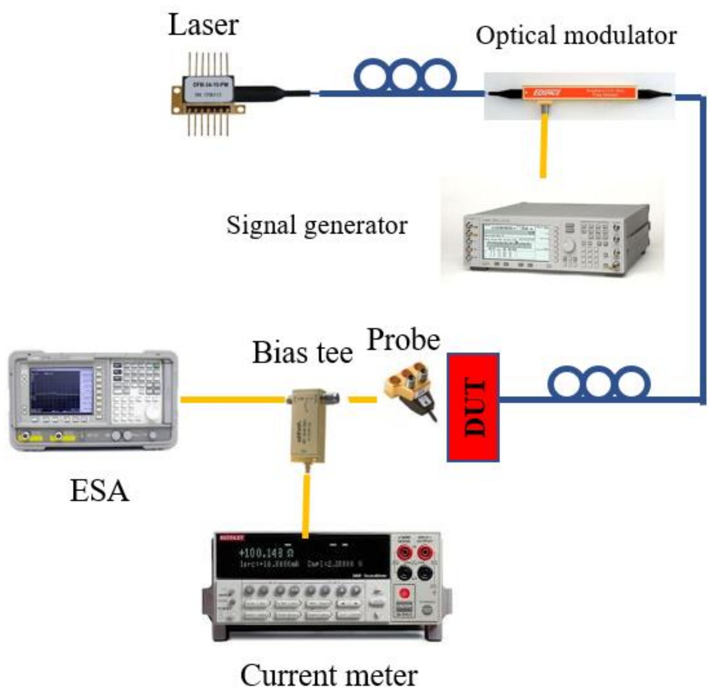

Fig. 2-8 Setup for characterizing photodiode bandwidth with an optical modulator.

Non-linearity measurement

In order to characterize the OIP3, it is necessary to measure the fundamental signal and IMD3. Figure 2-9 shows the setup for a three-tone OIP3 measurement setup. Three lasers are intensity-modulated by three Mach-Zehnder modulators (MZM) with close modulation frequencies f_1, f_2 and f_3. These three signals are combined by optical couplers and amplified by an EDFA before being detected by the photodiode. During the measurement, the signals at f_1, f_2 and f_3 should be kept at the same power level. The OIP3 is read for the tones at frequency $f_1 + f_2 - f_3$, $f_1 - f_2 + f_3$ and $-f_1 + f_2 + f_3$. Therefore, the fundamental frequencies should be chosen carefully to avoid the situation that any IMD frequencies coincide with fundamental frequency and other IMD frequencies. The OIP3 can be calculated by measuring the IMD3 power at different power levels of the fundamental frequency. The intercept point can be calculated by linear extrapolation as shown in figure 2-4.

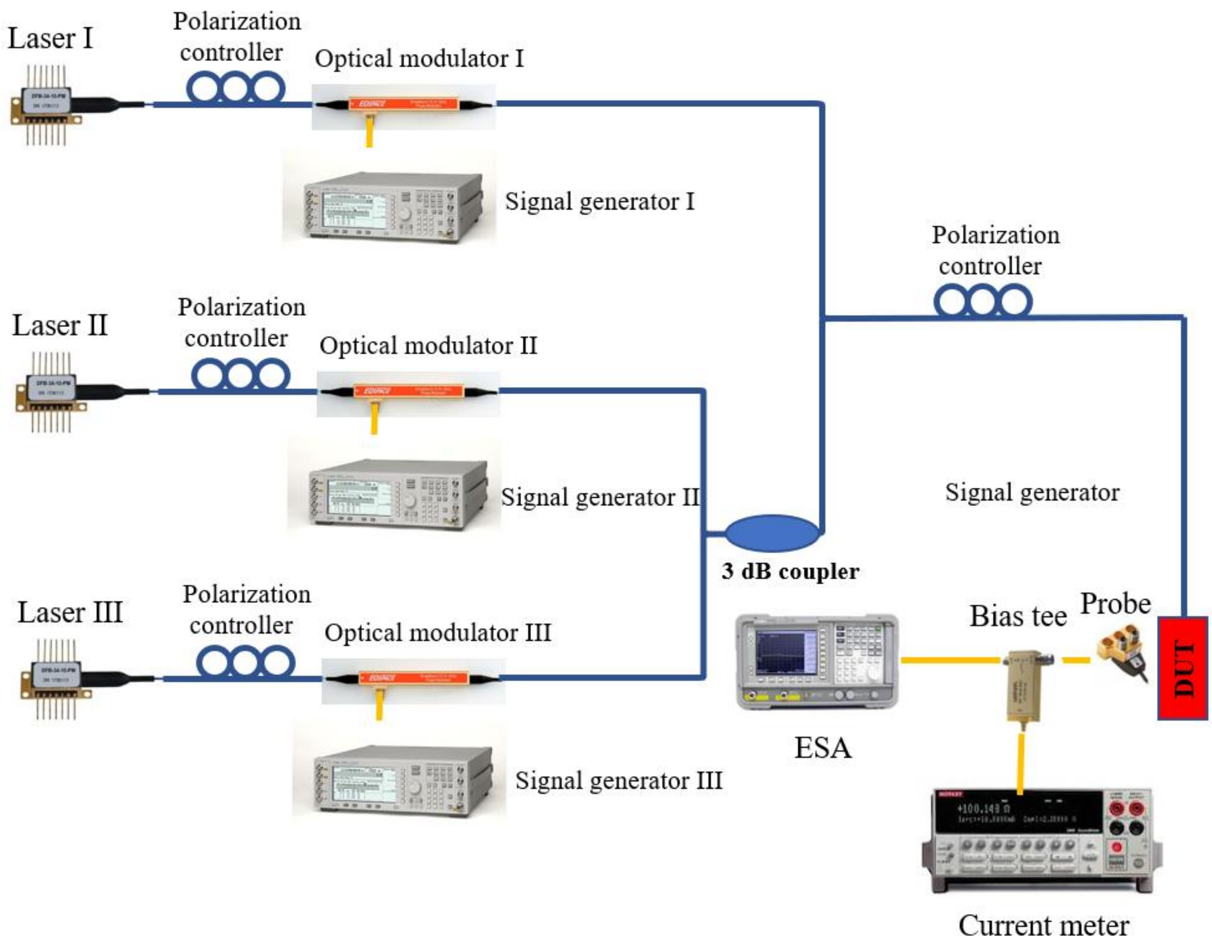

Fig. 2-9 A three-tone setup for characterizing photodiode nonlinearity.

2. 3 Photodiode fabrication process

Metal deposition

Metal deposition is a crucial process as it helps achieving good ohmic contact resulting in low series resistance. An electron beam (E-beam) evaporator is used for this process. Metal patterns are defined by photolithography and a lift-off process. In my process, Ti/Pt/Au are deposited on heavily P-type doped InP to achieve good ohmic contacts. Their thicknesses are 20 nm, 30 nm, and 50 nm. For the N-contact, typically AuGe/Ni/Au are chosen with 30 nm, 20 nm and 80 nm.

Mesa etching

During the fabrication process, most of the III-V material needs to be etched away to form the device mesa. Both wet and dry etch can be used. Both of them are widely used and have their own pros and cons. This will be addressed in chapter 4.

Etchant	**Material**					
	InP	InGaAs	InAlGaAs	InGaAsP	SiO_2	Si_3N_4
$HCl:H_2O$	Etch	Stop	Selectively etch	Selectively etch	Stop	Stop
$HCl:H_3PO_4$	Etch	Stop	Selectively etch	Selectively etch	Stop	Stop
$H_2SO_4:H_2O_2:H_2O$	Stop	Etch	Selectively etch	Selectively etch	Stop	Stop
$H_3PO_4:H_2O_2:H_2O$	Stop	Etch	Selectively etch	Selectively etch	Stop	Stop
$HF:H_2O$	Stop	Stop	Stop	Stop	Etch	Etch

Table. 2-2 Wet chemical etchants used in this dissertation.

For wet etch, different etchants work for different materials. The selectivity of the etchants used in this dissertation are summarized in table 2-2. From the table, it can be seen that some of the wet etchants have etching selectivity. This property can be used to control mesa etching precisely when etch stop layers are used. In addition, wet etch also produces smoother sidewalls and lower leakage current. However, due to its isotropic nature, wet etch may cause lateral undercuts during the process. This can be a problem for small-sized devices with diameters < 10 µm.

Another etching method with improved pattern transfer is dry etching which is carried out by an Oxford RIE-ICP system. The recipe I used is Cl_2: N_2 at around 50 °C under 4 mTorr pressure. The etch rates of this recipe are 90 nm/min for InP, 130 nm/min for InGaAs and 25 nm/min for

SiO_2. The difference in etching rates makes it possible to use silica as a hard mask to protect the regions that are not desired to be etched. Dry etching provides a more accurate pattern transfer from the mask into the material. However, it tends to lead to a higher surface leakage current due to surface damage. In practice, a combination of dry and wet etching can be used to mitigate each of its shortcomings.

SiO_2 deposition

As mentioned before, silica can be used as a hard mask. In our lab, SiO_2 can be deposited by two methods. One is plasma enhanced chemical vapor deposition (PECVD) with SiH_4 (400 sccm) and N_2O (105 sccm) gas mixture at 280 °C. The deposition rate is around 12 nm/min. This hard mask can be etched away by buffered oxide etchant (BOE) or in the Oxford dry etching machine with O_2 (60 sccm):CF_4 (2 sccm) gas mixture at room temperature. Moreover, the SiO_2 deposited by PECVD also can be used for sidewall passivation to reduce surface leakage current. Another method is turbo sputtering. However, this deposited silica cannot be used for sidewall passivation due to violent ion bombardment during the process. However, sputtering is a low-temperature process and it is suitable for devices that cannot survive high temperatures. These two kinds of deposited SiO_2 have similar etch rates in when using the Oxford dry etching recipe.

Gold plating

Electro-plating is used to build air-bridges and contact pads in the process. Five steps are involved in the process. First, the pad area and top contact part in the mesa are defined by photolithography. Secondly, a seed layer (Ti/Au) is deposited on the devices. Then another round of photolithography is needed to define the air-bridge and contact pads. Afterwards, plating the sample in plating solution until the gold thickness reaches around 2 µm. Finally, remove the top layer of photoresist by O_2 plasma and etch away Au seed layer by Au etchant. Then soak the sample in acetone and lift-off the metal not in the areas of the pads, air-bridges and contacts in ultra-sonic bath.

2.4 Summary

This chapter introduces the figure of merits of photodiodes and describes different photodiode structures. The experimental setups for characterizing the performance of photodiodes in this dissertation are discussed. Finally, critical steps of the photodiode fabrication process are also introduced. These fabrication methods will be modified and adjusted accordingly depending on the different photodiode structures in this dissertation and will be described in the following chapters.

References

[2.1] B. T. Marozas, W. D. Hughes, X. Du, D. E. Sidor, G. R. Savich, and G. W. Wicks. "Surface dark current mechanisms in III-V infrared photodetectors." Optical Materials Express 8, no. 6 (2018): 1419-1424.

[2.2] S. R. Forrest, M. DiDomenico Jr, R. G. Smith, and H. J. Stocker. "Evidence for tunneling in reverse-biased III-V photodetector diodes." Applied Physics Letters 36, no. 7 (1980): 580-582.

[2.3] X. D. Wang, W. D. Hu, X. S. Chen, W. Lu, H. J. Tang, T. Li, and H. M. Gong. "Dark current simulation of InP/In 0.53 Ga 0.47 As/InP pin photodiode." Optical and quantum electronics 40, no. 14-15 (2008): 1261-1266.

[2.4] S. Forrest. "Performance of In x Ga 1-x As y P 1-y photodiodes with dark current limited by diffusion, generation recombination, and tunneling." IEEE Journal of quantum Electronics 17, no. 2 (1981): 217-226.

[2.5] S. Alexander, S. B. Rafol, A. Khoshakhlagh, J. Nguyen, L. Hoglund, A. M. Fisher, S. A. Keo, D. Z-Y. Ting, and S. D. Gunapala. "Proton radiation effect on performance of InAs/GaSb complementary barrier infrared detector." Applied Physics Letters 107, no. 26 (2015): 261102.

[2.6] X. Du, G. R. Savich, B. T. Marozas, and G. W. Wicks. "Suppression of lateral diffusion and surface leakage currents in nBn photodetectors using an inverted design." Journal of Electronic Materials 47, no. 2 (2018): 1038-1044.

[2.7] S. M. Sze and Kwok K. Ng. Physics of semiconductor devices. John wiley & sons, 2006.

[2.8] K. Kato, S. Hata, K. Kawano, and A. Kozen. "Design of ultrawide-band, high-sensitivity pin photodetectors." IEICE Transactions on Electronics 76, no. 2 (1993): 214-221.

[2.9] D.A. Tulchinsky, J. B. Boos, D. Park, P. G. Goetz, W. S. Rabinovich and K. J. Williams, “High-Current Photodetectors as Efficient, Linear, and High-Power RF Output Stages”. Lightwave Technology, Journal of, 2008. 26(4): p. 408-416.

[2.10] K.J. Williams, and R.D. Esman, “Design considerations for high-current photodetectors”, Lightwave Technology, Journal of, 1999. 17(8): p. 1443-1454

[2.11] Z. Li, Y. Fu, M. Piels, H. Pan, A. Beling, J. E. Bowers, and Joe C. Campbell. "High-power high-linearity flip-chip bonded modified uni-traveling carrier photodiode." Optics express 19, no. 26 (2011): B385-B390.

[2.12] Y. Fu, H. Pan, Z. Li, A. Beling, and J. C. Campbell. "Characterizing and modeling nonlinear intermodulation distortions in modified uni-traveling carrier photodiodes." IEEE Journal of Quantum Electronics 47, no. 10 (2011): 1312-1319.

[2.13] K. Kato, S. Hata, K. Kawano, and A. Kozen, "Design of UltrawideBand, High-Sensitivity p-i-n Photodetectors," IEICE Trans. Electron., Vol.E76-C, No. 2, February 1993, pages: 214-221.

[2.14] K. J. Williams, "Comparisons between dual-depletion region and uni-travelling-carrier p-i-n photodetectors," IEE Proc.-Optelectron., Vol. 149, No. 4, August 2002, pages: 131-137.

[2.15] H. Ito, T. Furuta, S. Kodama, N. Watanabe, T. Ishibashi, *"InP/InGaAs uni-travelling-carrier photodiode with 220 Ghz bandwidth".* Electronics Letters, 1999. **35**(18): p. 1556-1557.

Chapter 3. High-performance III-V photodiodes on silicon

3.1. Introduction

Silicon photonics is a promising platform to integrate low-cost and high-performance passive photonic components for data centers and many other applications. However, since silicon is an indirect bandgap material and transparent at telecom wavelengths, active optical silicon components are not available. In order to achieve high-performance active optical components in silicon photonics, heterogeneous integration is a promising technology. For the integration of group III-V photodiodes on silicon, various integration approaches have been reported, including adhesive wafer bonding [3.1], direct molecular wafer bonding [3.2], and direct III-V material growth on Si [3.3]. Among the bonding techniques, SU-8 bonding is attractive since it requires a low-temperature process and can tolerate a considerable amount of surface roughness. SU-8 is a high contrast, epoxy-based common photoresist, which is transparent from 400 nm up to 1600 nm. In my work, I use SU-8 as the adhesive layer between the III-V die and the silicon substrate.

Previously, Ye Wang, in collaboration with Linli Xie and Souheil Nadri from Prof. Weikle's group successfully proved the feasibility of bonding an III-V PD die on silicon with a 1.4 µm-thick layer of SU-8. They successfully fabricated a single mesa PD with reasonable dark current. This result indicated that high material quality can be maintained during the heterogeneous integration by SU-8. However, whether such bonding mechanism can yield high-performance PDs using an established fabrication process for a double-mesa photodiode with coplanar waveguide was still questionable at the time. Moreover, the thickness of the SU-8 was 1.4 µm in the previous process. This large thickness of the SU-8 poses an issue for evanescently-coupled waveguide PDs suitable for photonic integration as optical coupling from a waveguide into the active region of a PD through the 1.4 µm-thick low-index SU-8 layer is very inefficient. As will be discussed in chapter 4, a thin SU-8 bonding layer is desired for waveguide photodiodes.

In this chapter, I demonstrate back-illuminated high-power modified uni-traveling carrier photodiodes on silicon by using SU-8 as a bonding layer for the first time. In my work, SU-8 6000.5 was adopted to reduce the SU-8 thickness to 250 nm. The developed fabrication process is similar to the one for PDs on native substrate which demonstrates that such integration is feasible for PDs for high power applications on Si.

3.2 PDs on silicon

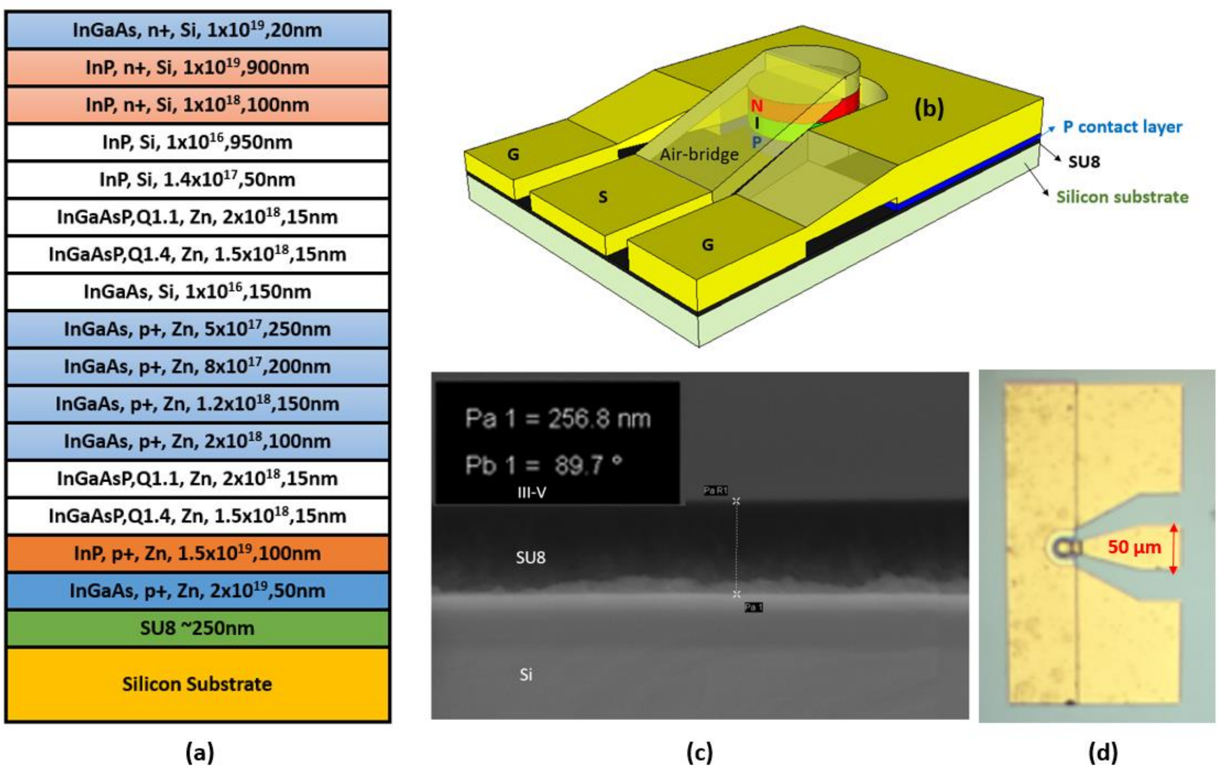

Fig. 3-1 (a) Epitaxy layer structure; (b) schematic view of back-illuminated PD with ground-signal-ground (GSG) microwave pad; (c) SEM cross-sectional image; (d) top-view of fabricated PD.

For my work I adopted the MUTC-4 epitaxial layer structure, which previously has been shown to have high-power performance [3.4]. Figure 3-1 (a) shows the layer structure of the modified uni-traveling carrier photodiode bonded onto silicon after substrate removal. The III-V epitaxial structure was grown on InP by metal organic chemical vapor deposition (MOCVD) and consists of a 700 nm graded doped P-type InGaAs absorber, a 150 nm depleted InGaAs absorber and a 950 nm InP drift layer. The quaternary InGaAsP layers were designed to reduce the bandgap discontinuity at the heterojunction interface between the InP and InGaAs layers [3.4]. The die bonding process is based on the process in [3.6] and is summarized in appendix I. It includes SU-8 spin coating, soft bake at 110℃, UV exposure followed by a 40-minute outgas, and curing at 130℃ under 10 Psi for 30 min in the bonding machine shown in Fig. 3-2. The final adhesive layer of SU-8 was approximately 250 nm thick (figure. 3-1c). After using hydrochloric acid to selectively etch the InP substrate, I fabricated double-mesa photodiodes using conventional wet and dry etching techniques. Microwave probe pads were deposited on SU-8 and connected to the PD n-contacts through air-bridges (figure. 3-1(b) and (d)). The fabrication process is similar to the fabrication process of MUTC PDs on native substrate. The only difference is that the SiO_2 hard mask was deposited using RF sputtering instead of using PECVD. This is because the PECVD process requires a temperature of 285 °C, which is higher than the degradation temperature (200 °C) of SU-8.

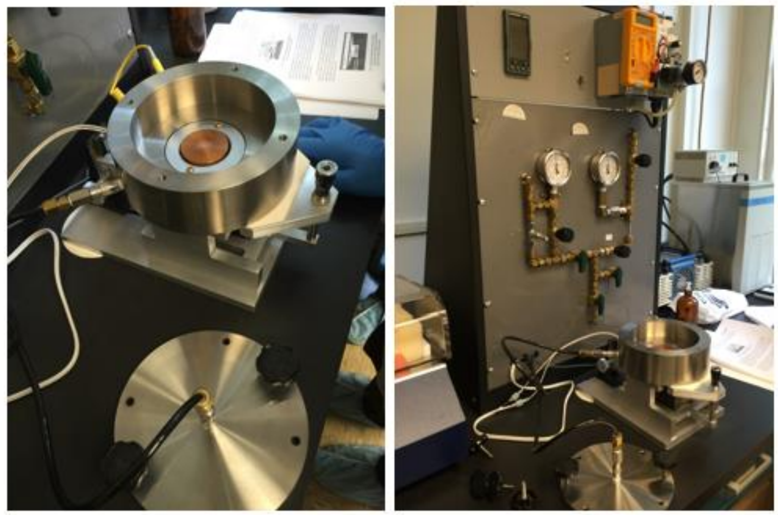

Fig. 3-2 UVA wafer bonder. Left: bonding chamber, right: control panel).

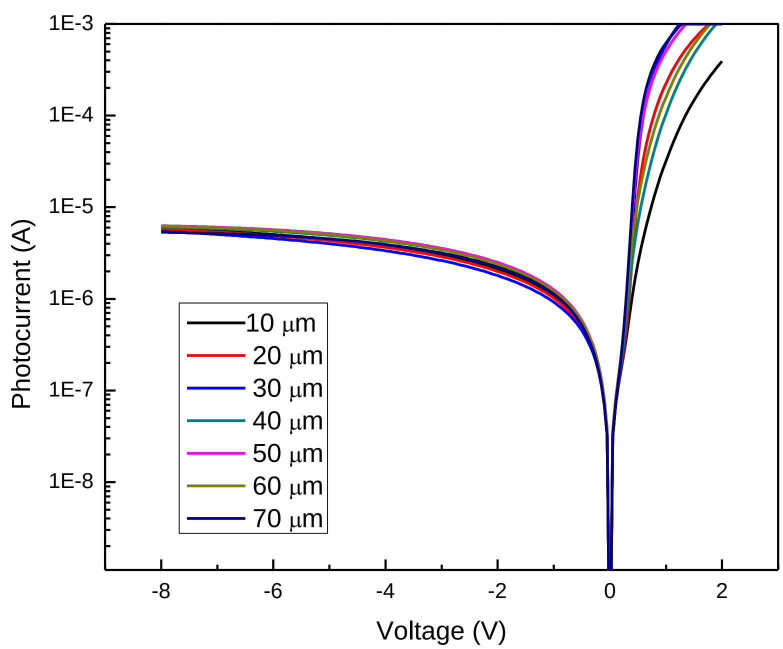

Fig. 3-3 Measured dark currents for different diameter PDs.

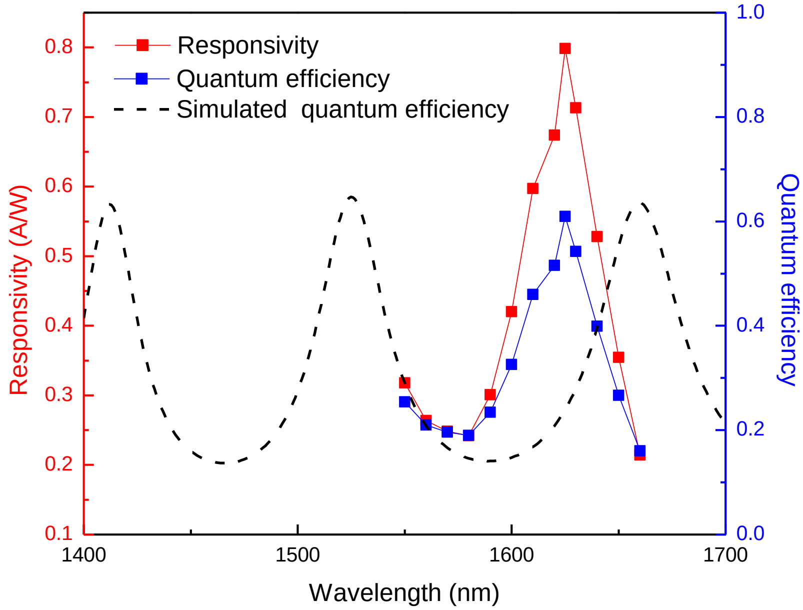

Fig. 3-4 Measured responsivity (red line), quantum efficiency (blue line) and simulated quantum efficiency versus different wavelength.

As shown in Fig. 3-3, around 5 μA dark current was achieved for different-sized photodiodes. Using a fiber collimator for back-illumination through the silicon substrate I measured a responsivity of 0.49 A/W at 1550 nm wavelength with sputtering SiO_2 as anti-reflection (AR) coating. A responsivity of 0.7 A/W can be achieved at 1550 nm for the same epitaxial layer structure on native substrate with AR coating. One of the possible reasons for the lower responsivity is that the 50 nm-thick InGaAs P-contact layer at the bottom absorbs around 5% of the input light but will not fully contribute to the photocurrent because of the band discontinuity and carrier recombination due to the high doping level between InP and InGaAs. Another reason is that the responsivity is wavelength dependent. During the responsivity measurement, I found that there is wavelength dependence on responsivity for this bonded device. This dependence has not been seen in photodiodes with identical layer stack on native substrate. In the measurement, 0.8 A/W responsivity at 1620 nm was achieved. The quantum efficiency is 61%, which is larger than the 56 % quantum efficiency measured from photodiodes grown on native substrate. As the absorption coefficient in InGaAs is even smaller at longer wavelength, it can be concluded that there is a responsivity enhancement effect in this heterogeneously integrated photodiode.

By using a general transform-matrix for optical multilayer system [3.5], it can be calculated that this responsivity dependence on wavelength is caused by the resonant cavity formed by the silicon (n = 3.48), SU-8 (n = 1.57) and the III-V layers (InP: n = 3.16; InGaAs: n = 3.56) which promotes the generation of a standing wave. As a result, this resonant cavity enhances the responsivity at some definite wavelengths and reduces it at others. To show this, I tuned the input laser wavelength and measured the responsivity that is shown in the Fig. 3-4. The quantum efficiency is also calculated and is shown in the plot as blue dotted curve. The dashed line shows the simulated quantum efficiency by transfer-matrix method. It can be seen that the measured result agrees well with the simulation. The wavelength shift is caused by SU-8 thickness variations and some uncertainty in the photodiode layer thicknesses. By adjusting the layer thicknesses and the SU-8 thickness, the resonance can be tuned to shorter wavelength and will further improve the responsivity at 1550 nm.

The PDs' frequency responses are shown in fig. 3-5 (a) and were obtained under large-signal modulation using an optical heterodyne setup at 1550 nm wavelength. At 8 V reverse bias and 10 mA, I measured bandwidths of 18 GHz and 11 GHz for a 10 μm and 20 μm diameter PD, respectively. The frequency responses of the 20 μm diameter PD under different average photocurrents are shown figure. 3-5 (b). I observed a bandwidth enhancement effect from 5 GHz to 11 GHz when the photocurrent increases from 1 mA to 20 mA which can be attributed to the self-induced field in the un-depleted absorber [3.7].

RF output power and compression were measured at a fixed beat frequency and different reverse voltages (figure. 3-6). For the 20-μm and 10-μm diameter PDs, we recorded RF output power levels at the 3 dB cut-off frequencies as high as 5.8 dBm and 3.9 dBm, respectively. For the 10 μm PD, the saturation currents at 1 dB compression were 12 mA, 10 mA and 7.5 mA at 8 V, 6 V and 4 V, respectively. The saturation current reached 20 mA at 8 V for the 20 μm diameter PD. It should be mentioned that no thermal device failure was observed during these measurements.

To characterize photodiode linearity, I used an optical three-tone setup with each laser modulated by a Mach-Zehnder modulator as discussed in chapter 2. I determined the equivalent two-tone output third order intercept point (OIP3) from the measured intermodulation distortions (IMD3) as mentioned in chapter 2 [3.8]. At 15 mA, the OIP3 reached 28.5 dBm and 22.5 dBm at 1 GHz and 9 GHz, respectively (figure. 3-7 (a)). The OIP3 versus photocurrent for a 20-μm diameter PD is summarized in figure. 3-7 (b). Consistent with previous measurements from uni-traveling carrier type PDs we found that the OIP3 increases with higher photocurrents [3.9].

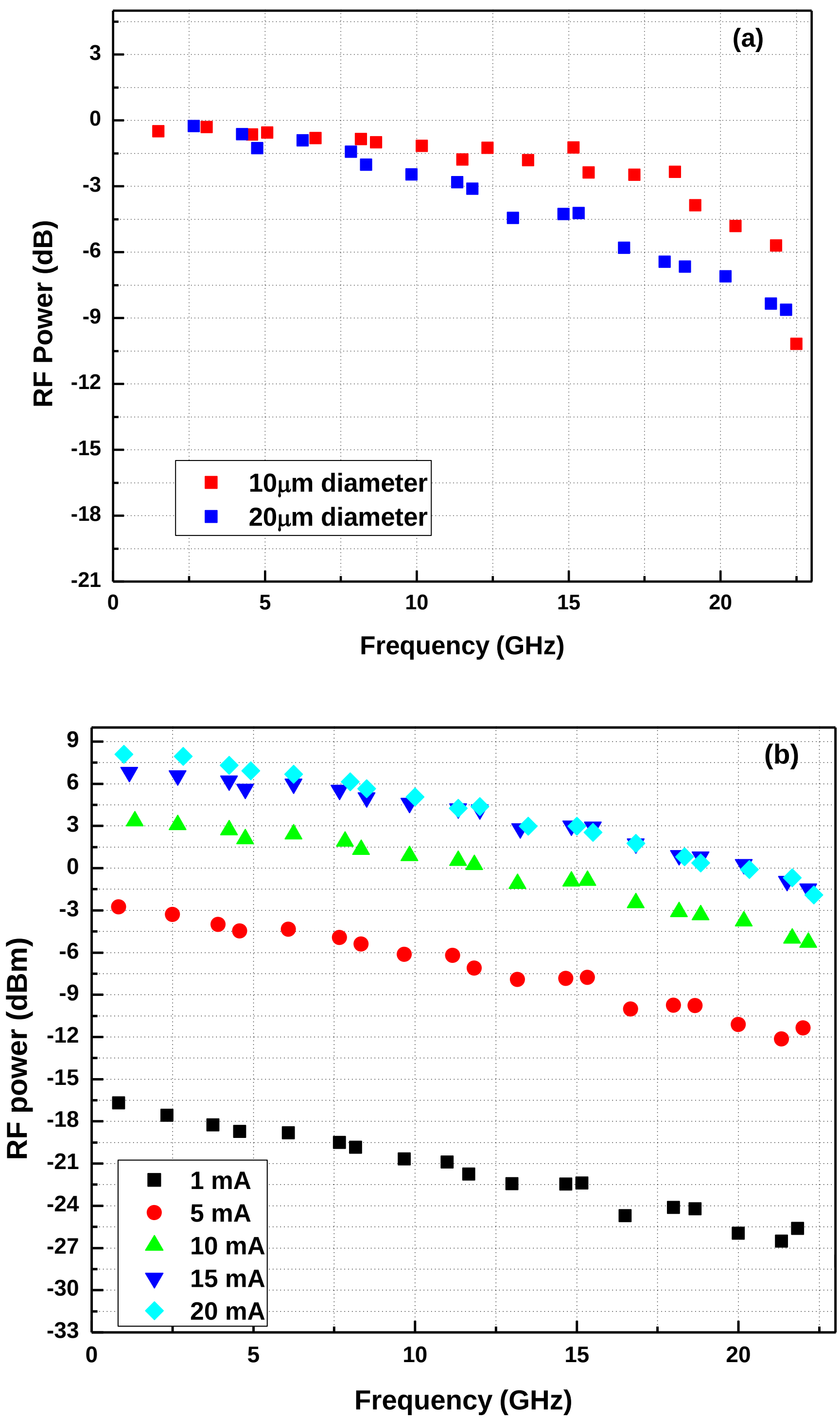

Fig. 3-5 (a) Measured frequency responses of 10-µm and 20-µm diameter PDs at 8 V reverse bias and 10 mA average photocurrent. (b) Frequency responses under different photocurrents for a 20-µm diameter PD at 8V reverse bias.

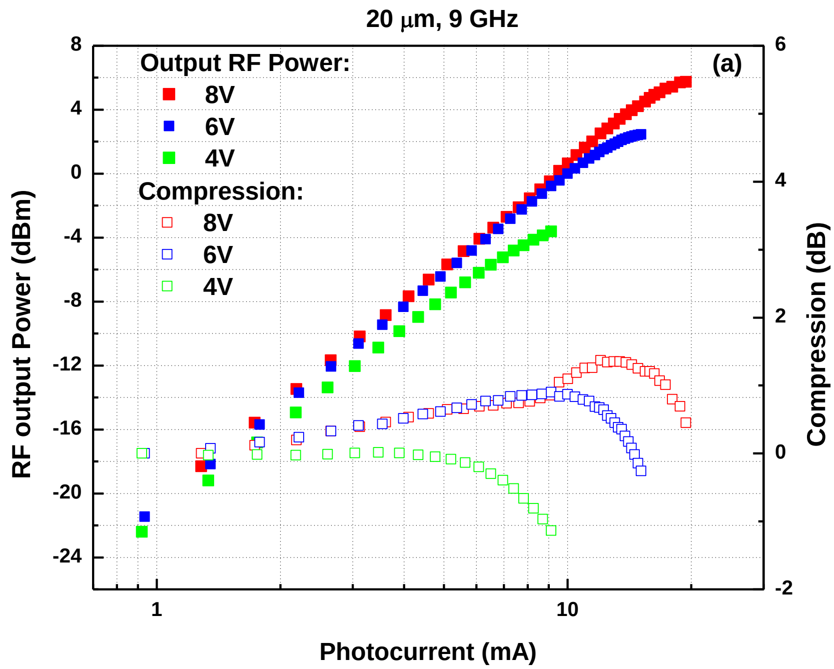

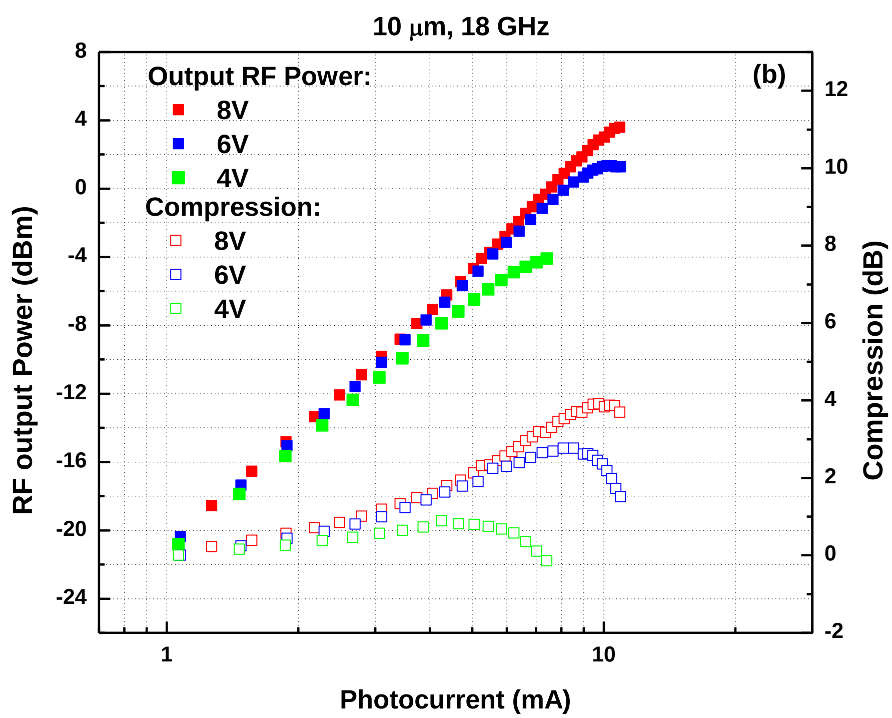

Fig. 3-6 RF output power and compression curve versus average photocurrent at (a) 9 GHz for a 20-μm PD; and (b) 18 GHz for a 10-μm PD.

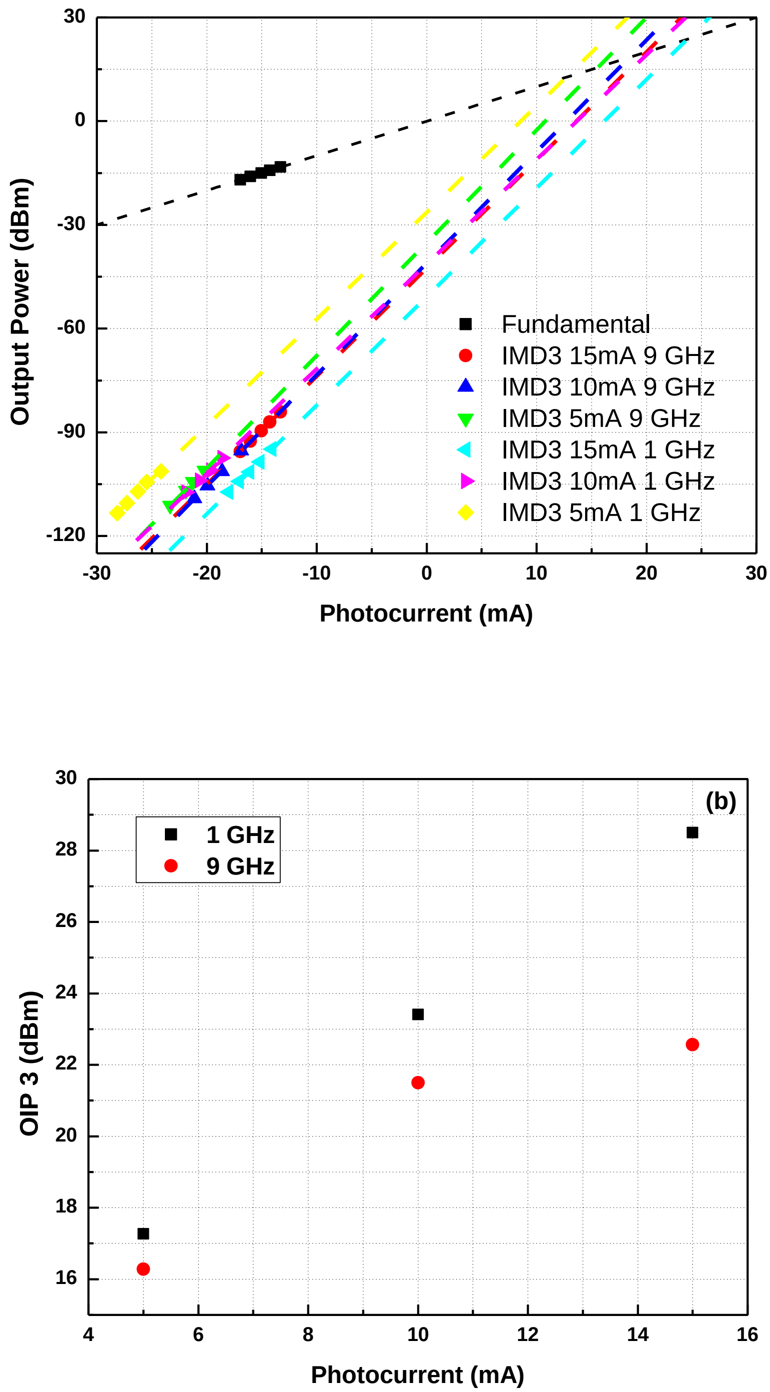

Fig. 3-7 20 µm diameter device (a) 1 GHz and 9 GHz IMD3 with different photocurrent; (b) OIP3 at 1 GHz and 9 GHz versus photocurrent.

3.3 Summary

InP-based modified uni-traveling carrier photodiodes heterogeneously integrated on silicon substrate using a low-temperature SU-8 bonding process are demonstrated in this chapter. The photodiodes reach bandwidths up to 18 GHz, large saturation currents up to 20 mA, and an OIP3 as high as 28.5 dBm at 1 GHz. The measured RF output power levels of 5.8 dBm at 9 GHz and 4 dBm at 18 GHz compare favorably to published results from top-illuminated uni-traveling carrier type germanium PDs on Si (3.7 dBm at 3 GHz, [3.10]) and III-V PDs that were directly grown on Si (-3.4 dBm at 8 GHz, [3.3]). An RCE effect was also noticed with 0.8 A/W at 1620 nm. This responsivity enhancement can be further used to improve photodiode's responsivity.

In my work, the thickness of the SU-8 bonding layer has been successfully thinned from 1.4 μm to 250 nm, which represents an important step towards heterogenous waveguide photodiode that are described in chapter 4.

References

[3.1] D. Liang, G. Roelkens, R. Baets, and J. E. Bowers, "Hybrid integrated platforms for silicon photonics," Materials, vol. 3, p. 1782, 2010.

[3.2] Y. Wang, Z. Wang, Q. Yu, X. Xie, T. Posavitz, M. Jacob-Mitos, A. Ramaswamy, E. J. Norberg, G. A. Fish, A. Beling, "High-Power Photodiodes With 65 GHz Bandwidth Heterogeneously Integrated Onto Silicon-on-Insulator Nano-Waveguides," in IEEE Journal of Selected Topics in Quantum Electronics, vol. 24, no. 2, pp. 1-6, March-April 2018.

[3.3] K. Sun, D. Jung, C. Sheng, A. Liu, J. E. Bowers, A. Beling, "Low-Dark Current III-V Photodiodes Grown on Silicon Substrate" IEEE Photonics Conference (IPC), 2017 IEEE. paper: MA3.1.

[3.4] Z. Li, H. Pan, H. Chen, A. Beling and J. C. Campbell, "High-saturation current modified uni-traveling-carrier photodiode with cliff layer," Quantum Electronics, IEEE Journal of, vol. 46, no. 5, pp. 626-632, 2010.

[3.5] C. C. Katsidis, and D. I. Siapkas. "General transfer-matrix method for optical multilayer systems with coherent, partially coherent, and incoherent interference." Applied optics 41, no. 19 (2002): 3978-3987.

[3.6] L. Xie, S. Nadri, N. Alijabbari, M. Cyberey, M. F. Bauwens, A. W. Lichtenberger, N. S. Barker, R. M. Weikle, "An Epitaxy Transfer Process for Heterogeneous Integration of Submillimeter-Wave GaAs Schottky Diodes on Silicon using SU-8", accepted, IEEE Electron Device Letters, 2017,doi: 10.1109/LED.2017.2756920

[3.7] T. Furuta, H. Ito, T. Ishibashi. "Photoresponse dynamics of uni-travelling-carrier and conventional pin-photodiodes", Conference Series Institute of Physics. Philadelphia; Institute of Physics; 1999, 2000, 166: 419-422.

[3.8] A. Ramaswamy, J. Klamkin, N. Nunoya, L. A. Johansson, L. A. Coldren, J. E. Bowers, "Three-tone characterization of high-linearity waveguide uni-traveling-carrier photodiodes." Lasers and Electro-Optics Society, 2008. LEOS 2008. 21st Annual Meeting of the IEEE. IEEE, 2008.

[3.9] A. Beling, H. Pan, H. Chen, and J. C. Campbell, "Linearity of Modified Uni-Traveling Carrier Photodiodes," JOURNAL OF LIGHTWAVE TECHNOLOGY, VOL. 26, NO. 15, AUGUST 1, 2008.

[3.10] C. Li, C. Xue, Z. Liu, H. Cong, B. Cheng, Z. Hu, X. Guo, W. Liu, "High-responsivity vertical-illumination Si/Ge uni-traveling-carrier photodiodes based on silicon-on-insulator substrate," Scientific Reports 6, Article number: 27743 (2016).

Chapter 4. Development of wafer bonding technique

4.1 Introduction

In chapter 3, the feasibility of integrating III-V epi on silicon by SU-8 has been verified. As mentioned in chapter 3, the SU-8 thickness is crucial for optical coupling in waveguide photodiodes. However, at the time, the thinnest SU-8 thickness produced so far in our group was around 250 nm. Thus, the bonding process still needs to be optimized for high efficiency photonic integration applications. It should be mentioned that another research group at Ghent University previously demonstrated a bonding layer of benzocyclobutene (BCB) with 45 nm thickness [4.1]. In this chapter, the process development of SU-8 bonding layers with thickness below 100 nm will be discussed.

4.2 Why thin SU-8

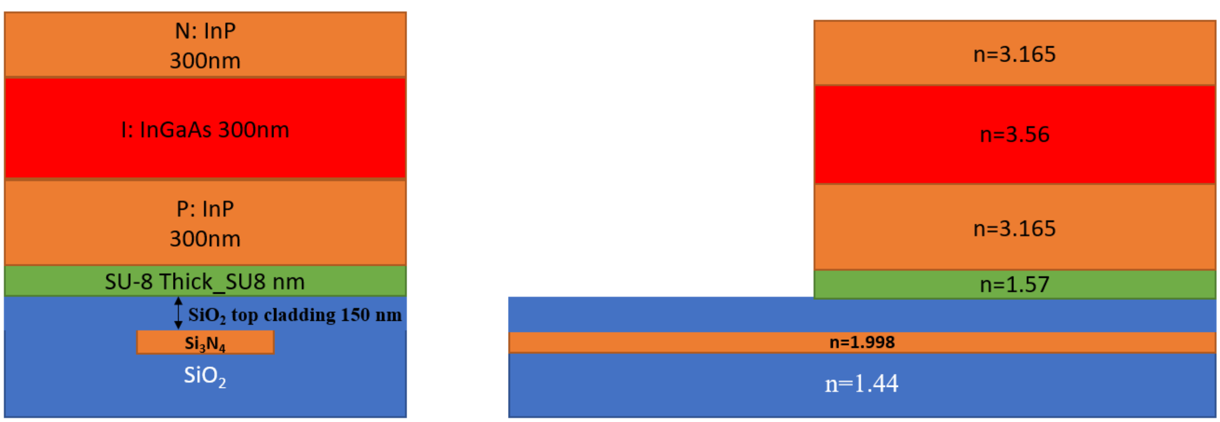

Fig. 4-1 PIN photodiode cross section (left) and side view (right) used in optical simulations on silicon nitride platform for SU-8 thickness investigation.

In heterogeneously integrated waveguide photodiodes, the SU-8 bonding layer is located between the waveguide and the active photodiode layers as shown in Fig.4-1. In the following chapters I will discuss photodiodes on the silicon nitride platform. To this end, I simulated photodiodes on silicon nitride waveguides to evaluate what maximum thickness of SU-8 layer can be tolerated. Silicon nitride waveguides have been demonstrated with low loss and the possibility for integration with a photodiode [4.2-4.3]. Starting with a simple structure (a PIN photodiode) on silicon nitride as shown in figure 4-1, the quantum efficiency for this structure is simulated in Fig. 4-2 by scanning different SU-8 thickness in Rsoft. The photodiode's dimensions are 10 µm wide and 20 µm long. In Fig. 4-2, it can be seen that once the thickness of SU-8 is larger than 200 nm, the quantum efficiency will be below 60%. Therefore, it is crucial to make the thickness of SU-8 layer below 150 nm in order to achieve a high QE photodiode.

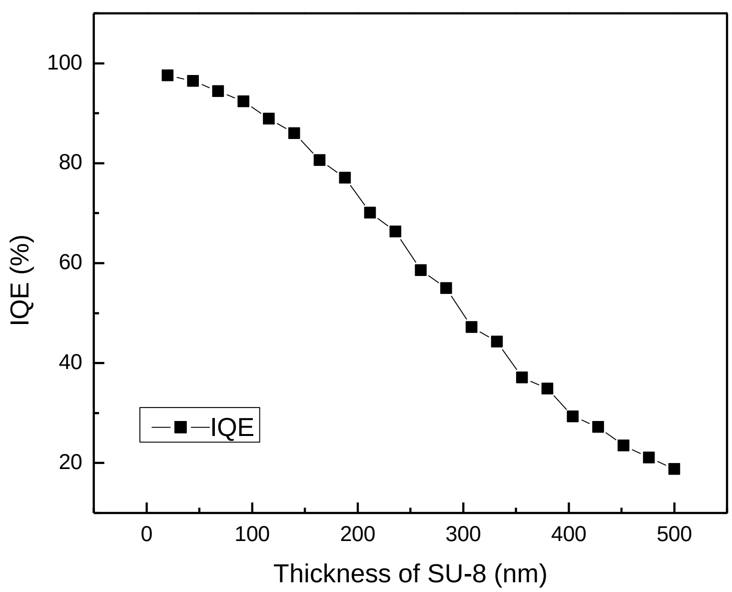

Fig. 4-2 Simulated quantum efficiency vs. SU-8 thickness for a 10 x 30 µm^2 PD.

4.3 SU-8 thickness

In the bonding process, SU-8 is spin coated on the sample. The thickness of the SU-8 is dependent on many factors, which can be derived as : [4.4]

$$h = \left(1 - \frac{\rho_A}{\rho_{A0}}\right) \cdot \left(\frac{3 \cdot \eta \cdot m}{2 \cdot \rho_{A0} \cdot \omega^2}\right)^{1/3} \quad (4\text{-}1)$$

where h is the thickness, ρ_A is the density of volatile liquid, ρ_{A0} is the density of volatile liquid at the beginning, η is viscosity of solution, m is rate of evaporation and ω is angular speed. From this equation, it can be seen that a higher spin speed and a lower viscosity of the solution lead to a thinner layer of SU-8 during spin coating.

Figure 4-3 shows a spin curve for an example of SU-8 6000.5 solution. It predicts how spin speed changes spin coating thickness. However, the spin speed already reached 9000 rpm in our previous recipe as described in appendix I. This is close to the maximum spin speed for our spin coating machine (10000 rpm). Therefore, reducing SU-8 viscosity is an option to further reduce SU-8 thickness.

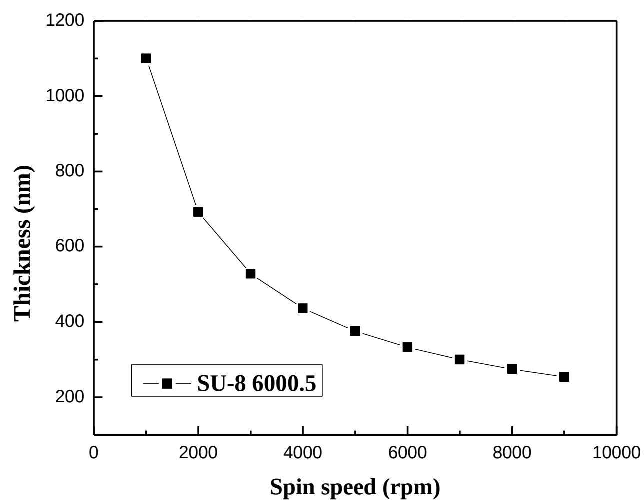

Fig. 4-3 Spin curve for an example solution of SU-8 6000.5.

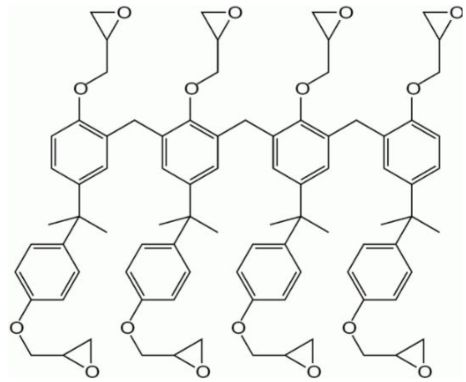

Fig. 4-4 SU-8 molecule.

SU-8 as shown in Fig. 4-4 is a widely used epoxy-based negative photoresist and commonly diluted by gamma-butyrolactone or cyclopentanone. In order to reduce viscosity of SU-8, diluting SU-8 by cyclopentanone is tried here. Table 4-1 summarizes known SU-8 thicknesses with different concentrations of SU-8 by cyclopentanone diluting. It can be seen that diluting SU-8 makes thinner spin coatings possible.

SU-8 type	2010	2005	2002	2000.5
SU-8 concentration	58%	45%	29%	14.3%
SU-8 thickness (3000 rpm)	7 µm	5 µm	2 µm	500 nm

Table 4-1 SU-8 thicknesses with different SU-8 2000 concentrations.

However, it has not been reported yet that chemically and physically stable SU-8 with thicknesses below 100 nm for wafer bonding has been achieved. I further diluted SU-8 with cyclopentanone with ratios: 1:1, 1:2 and 1:3 to investigate spin coating thickness of the diluted SU-8. I spin coated SU-8 with various dilution ratios on silicon for test and then deposited metal on the top by E-beam. The cleaning and bake processes are identical to the ones described in appendix II. The samples were then put into SEM to verify the thickness variation. Depositing metal on the top of SU-8 is helpful to obtain high contrast images in the SEM. The sample's cross-section can be seen in figure 4-4. SEM pictures for these three samples are all shown in figure 4-5.

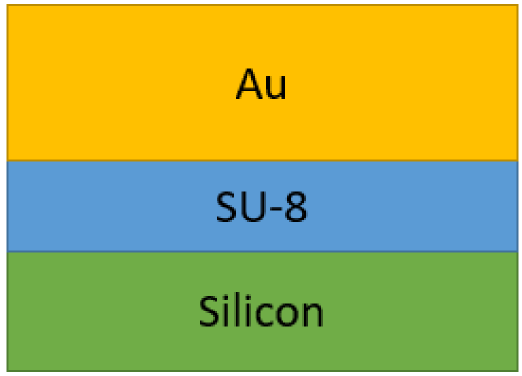

Figure 4-4 Samples' structure for SU-8 thickness investigation.

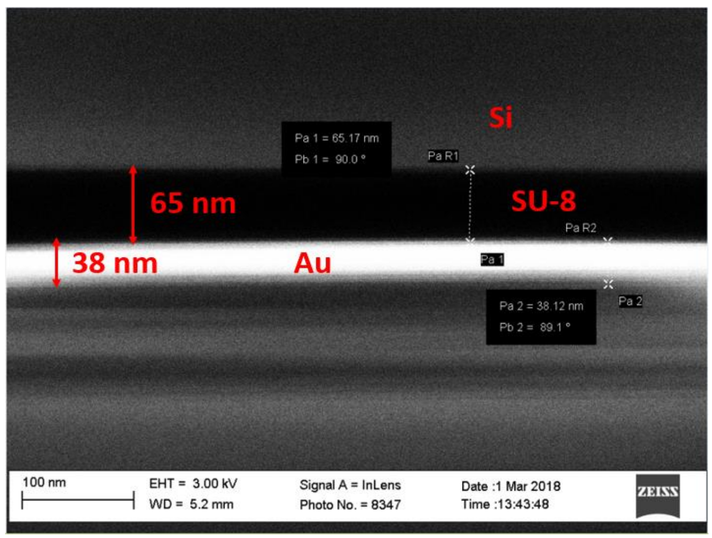

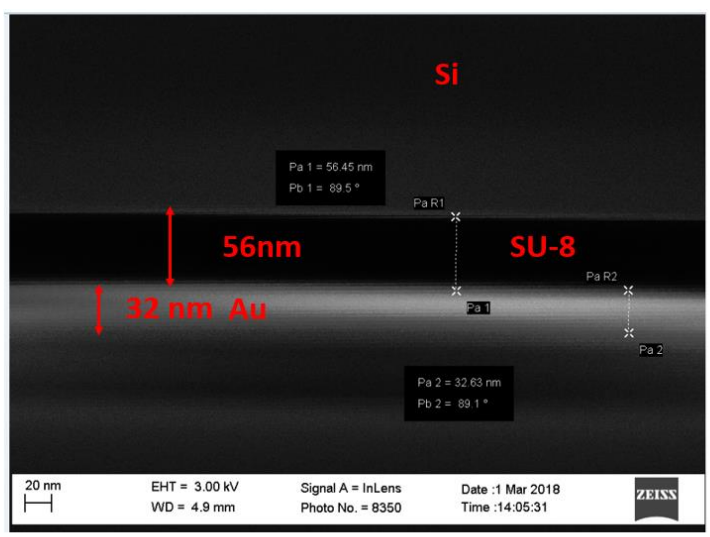

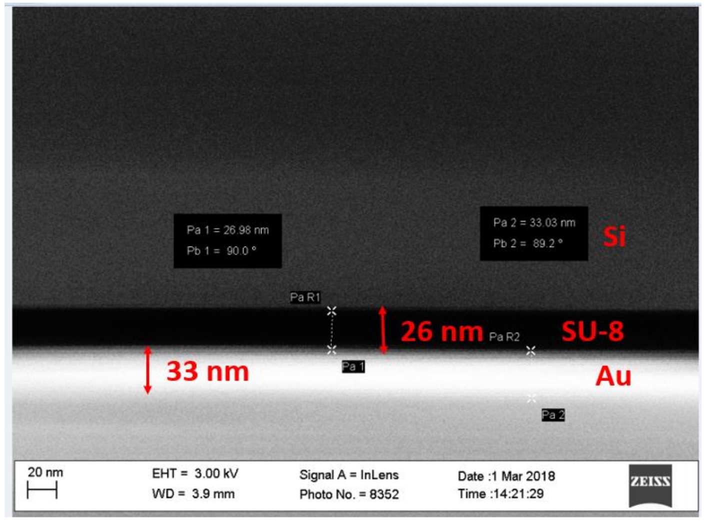

Figure 4-5 SEM pictures of the three samples shown in Table 4-2.

SU-8: cyclopentanone	1:1 (SU-8_1)	1:2 (SU-8_2)	1:3 (SU-8_3)
SU-8 thickness (nm)	65	56	26

Table 4-2 SU-8 thicknesses for different diluted SU-8 samples.

From the SEM results, it can be concluded that diluting SU-8 by cyclopentanone is able to provide SU-8 layers below 30 nm. It should be mentioned that the process that was used for the test sample is different from the real bonding process. In the bonding process, the III-V die should be bonded on silicon after UV exposure. In the test process, however, the samples were put into the E-beam chamber for air-evacuation overnight after UV exposure. Therefore, these test sample have a much longer outgassing time than the real bonded samples. While a change in SU-8 thickness can be expected due to extended outgassing time, the results are still valid to prove whether further diluted SU-8 can lead to a relatively thinner SU-8.

Following the bonding recipe in Appendix II, I first bonded a III-V epi on silicon with SU-8_1 (Table 4-2) at 9000 rpm as shown in Fig. 4-6. It can be seen that the SU-8_1 thickness is around 100 nm which is 35-nm thicker than the previous test sample with metal deposited on the top. This can be explained by the fact that the solvent is not totally evaporated in the bonding process. This also suggests that increasing outgassing time in the bonding process may lead to a more solid SU-8.

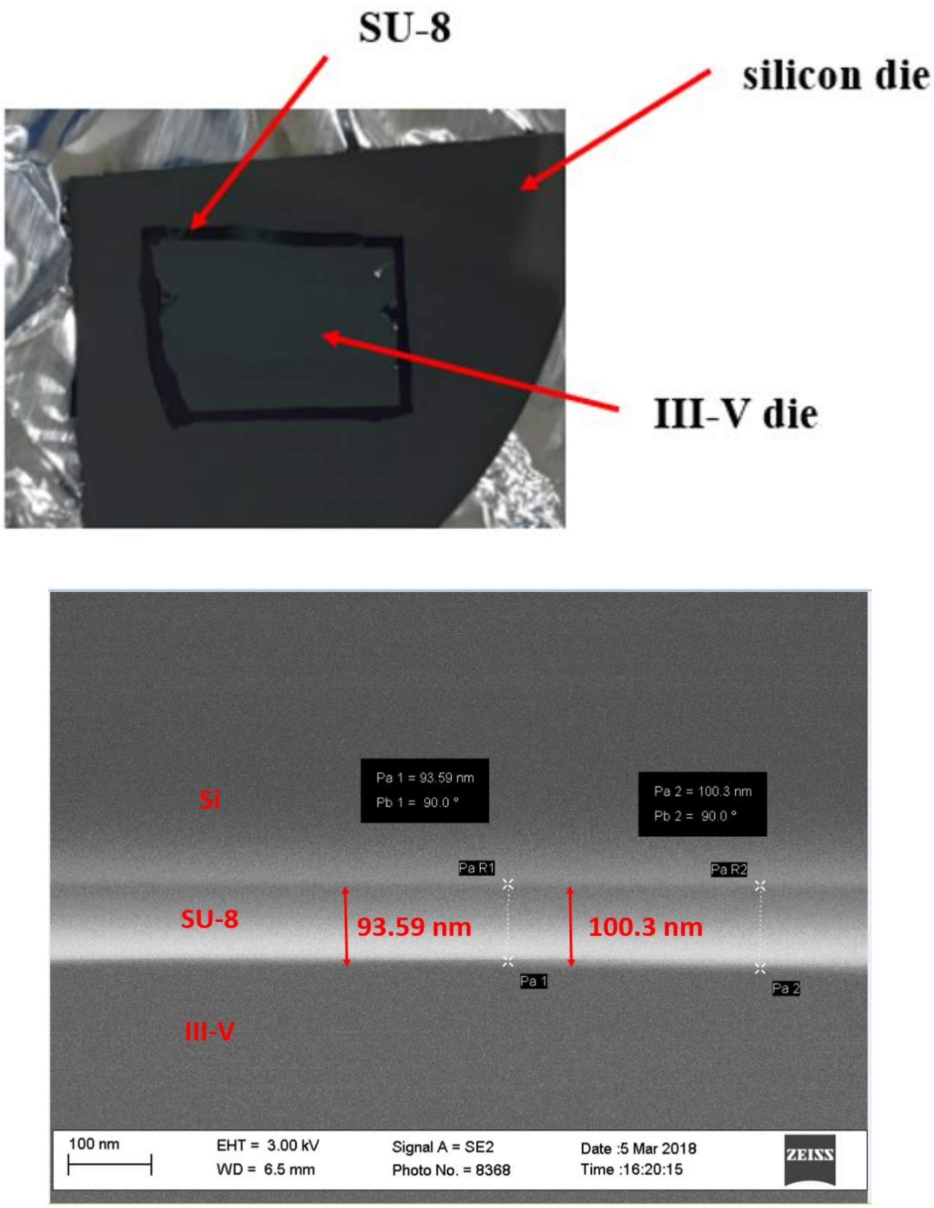

Figure 4-6 Image of SU-8_1 bonding sample (top) and its SEM pictures (bottom).

In order to further verify the thickness of the SU-8, an energy dispersive X-ray (EDX) spectroscopy was used in the SEM. SEM-EDX is an analytical technique used for elemental analysis of a sample. It relies on an interaction of X-ray excitation and a sample. Its characterization capabilities are due in large part to the fundamental principle that each element has a unique atomic structure allowing a unique set of peaks on its electromagnetic emission spectrum. The EDX result is shown in figure 4-7. Silicon atoms (red dots) and carbon atoms (green dots) were scanned in the SEM. In Fig. 4-7, the bottom figure is the identical SEM image as the top one but showing the mapping of silicon and carbon atoms. As carbon should only exist in SU-8 for this sample and silicon should be all in the carrier, the SU-8 thickness is verified to be around 88 nm This will be sufficient for high efficiency waveguide PDs.

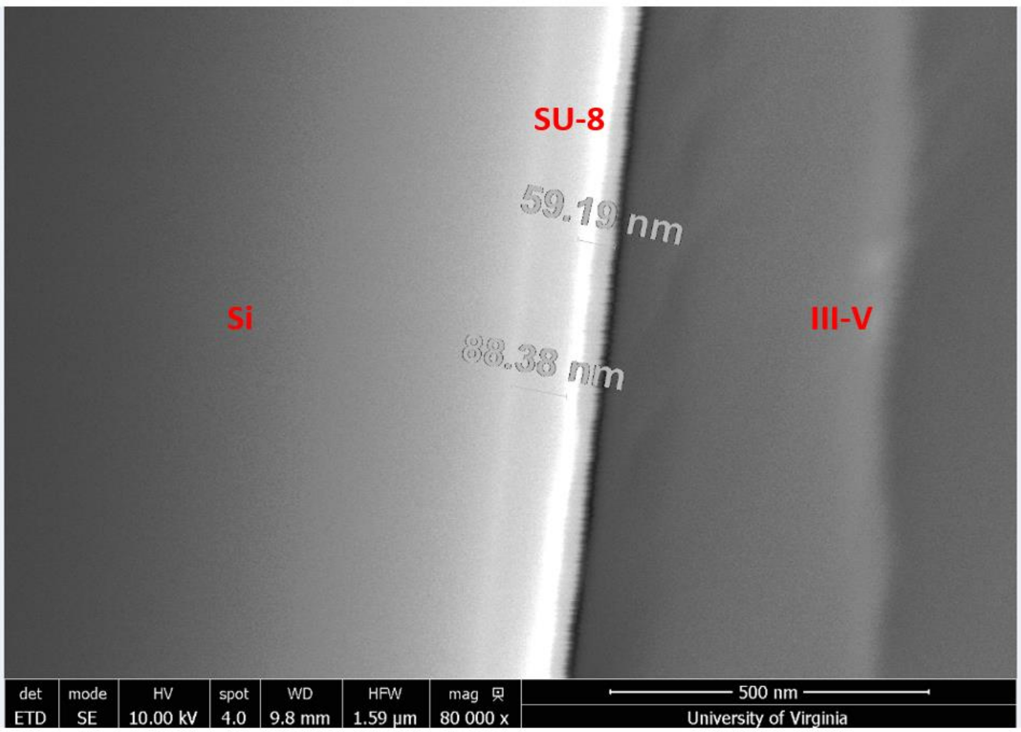

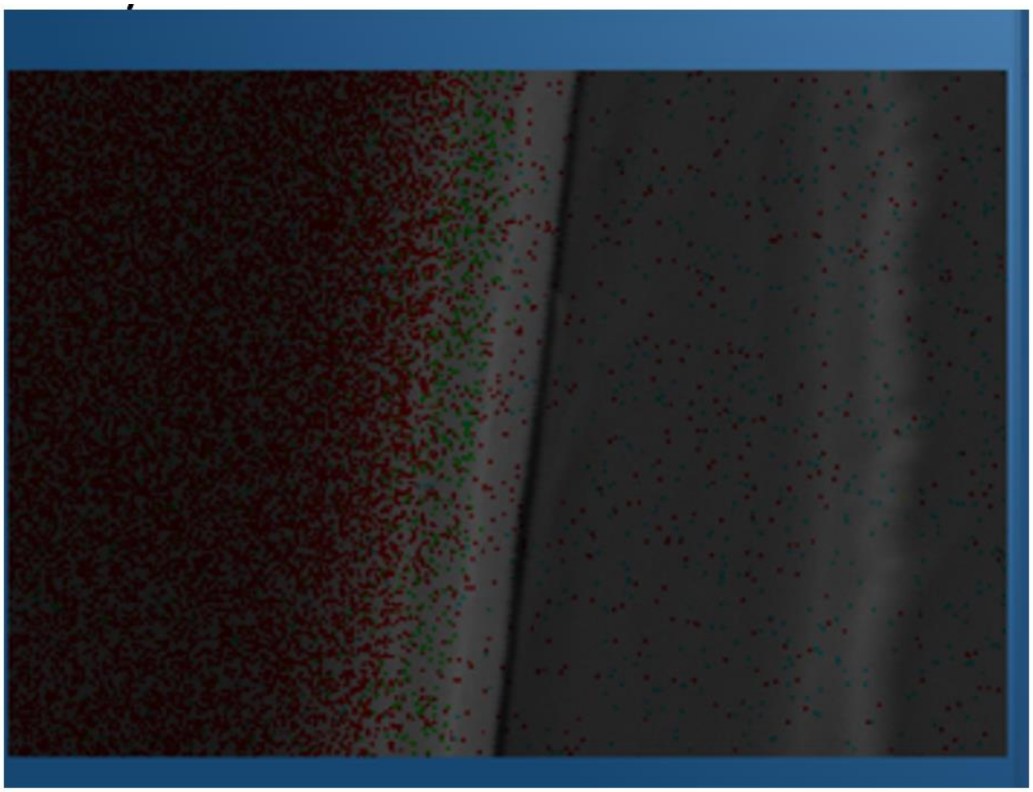

Figure 4-7 SEM-EDX picture of SU-8_1 bonding result at 9000 rpm. The top figure indicates the thickness while the bottom figure includes carbon and silicon atoms mapping.

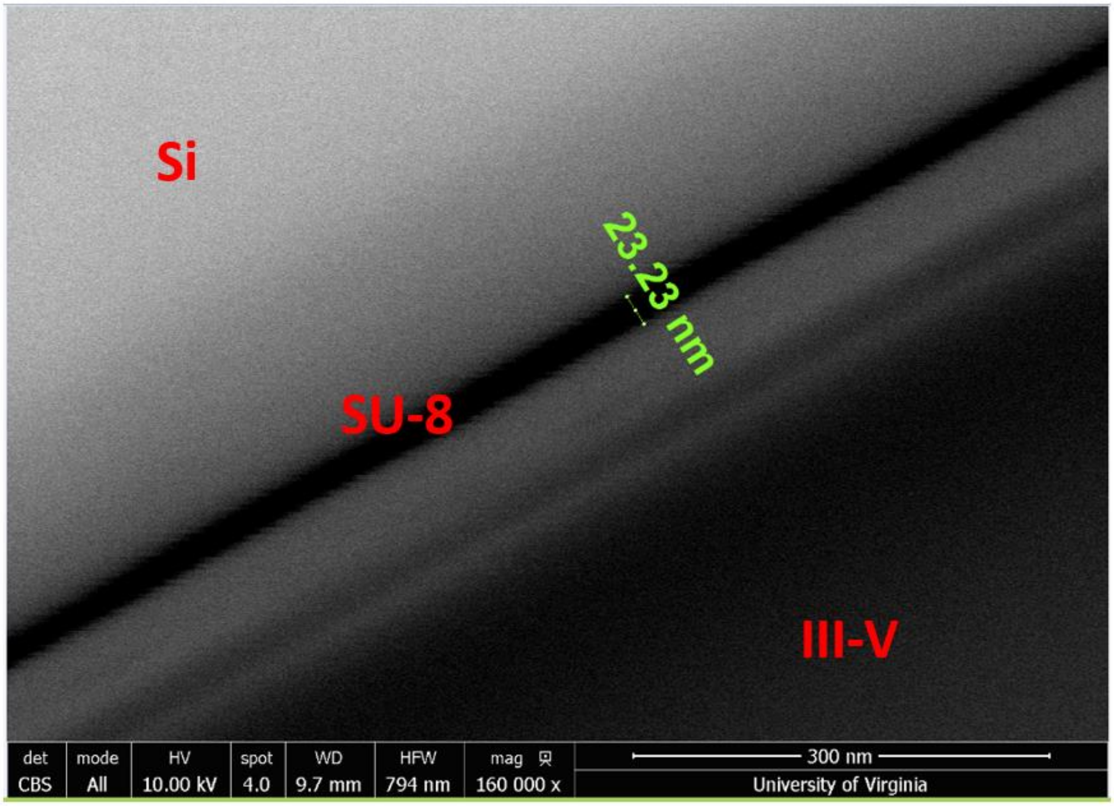

Figure 4-8 Image and SEM of SU-8_3 bonding result for 9000 rpm.

By using a similar bonding process as described in Appendix II, SU-8_3 was also spin coated on a silicon sample and bonded with III-V. The SU-8 thickness was 23 nm as shown in Fig. 4-8.

4.4 Summary

In this chapter, I developed a new bonding process based on very thin SU-8. Optimization of the bonding process includes bake time, bake temperature, UV exposure time, and outgassing time. Details can be found in appendices II and III. I successfully demonstrated thin bonding layers by using cyclopentanone for dilution. Two recipes have been verified to achieve 88 nm and 23 nm SU-8. These techniques will be used in the next chapter for heterogenous waveguide photodiodes.

References

[4.1] S. Stanković, D. V. Thourhout, G. Roelkens, R. Jones, J. Heck, and M. Sysak. "Die-to-die adhesive bonding for evanescently-coupled photonic devices." ECS Transactions 33, no. 4 (2010): 411-420.

[4.2] D. Blumenthal, R. Heideman, D. Geuzebroek, A. Leinse, and C. Roeloffzen, “Silicon nitride in silicon photonics,” Proceedings of the IEEE 106(12), 2209-2231 (2018).

[4.3] M. Piels, J. F. Bauters, M. L. Davenport, M. JR. Heck, and J. E. Bowers, “Low-loss silicon nitride AWG demultiplexer heterogeneously integrated with hybrid III–V/silicon photodetectors,” Journal of Lightwave Technology 32(4), 817-823 (2013).

[4.4] N. T. Phuong, R. Sami, C.M. Ouellet-Plamondon, “Nanomaterials-Based Coating”, 2019.

Chapter 5. Heterogeneously integrated waveguide photodiodes on silicon nitride platform

5. 1 Introduction

Photonic integration has been proven to enable an increasing number of applications in telecommunications [5.1], bio sensing [5.2], quantum information science [5.3], and microwave photonics [5.4]. As a complementary platform to silicon-on-insulator and InP-based photonic integrated circuits, the silicon nitride (Si_3N_4) photonic platform has attracted wide attentions in recent years due to its unique optical properties that are difficult to achieve in other material systems [5.5]. First, Si_3N_4 strip waveguides have demonstrated high power handling properties and a propagation loss below 0.1 dB/cm [5.5-5.6], even with very small bend radius [5.7]. Two photon absorption in the telecommunication band is virtually zero because of the large bandgap of Si_3N_4 (5.3 eV). Second, using Si_3N_4 waveguides, there have been numerous demonstrations of frequency comb generation [5.8-5.9], supercontinuum generation [5.10-5.11], and wavelength conversion [5.12]. Moreover, the fact that the transparency window of the Si_3N_4 platform ranges from visible to mid-infrared wavelengths makes it possible to generate an octave-spanning frequency comb, which is a crucial component in a chip-scale optical synthesizer [5.13].

To date, devices for efficient on-chip light generation, amplification, and detection continue to be dominated by group III-V semiconductors. While the Si_3N_4 platform lacks monolithic active devices, heterogeneously integrated III-V components have the potential to complement the platform and enhance functionality. For optical detectors, only few heterogeneous photodetectors on Si_3N_4 waveguides have been published to date, and are summarized in Table 5-1.

Detector structure	Measured external responsivity (A/W)	Bandwidth (GHz)	Dark Current	Ref.
h-BN/MoS2/graphene	0.24	28	< 10 nA at 10 V	5.14
InGaAsP/InP MUTC	0.15	3.5	1 µA at 1 V	5.15
InGaAs/InP PIN	0.36	30	650 µA at 2 V	5.6
InGaAs/InP PIN	(0.68*)	25	2 nA at 4 V	5.16

Table 5-1 Optical detectors on Si_3N_4 waveguide at 1550 nm wavelength reported in the literature. (*): Estimated internal responsivity.

In this chapter, I will first introduce a heterogeneously integrated InGaAs/InP PIN photodiode on silicon nitride waveguide. The photodiodes are designed for a chip-scale optical synthesizer as shown in figure 5-1 [5.13]. In the system, photodiodes on silicon nitride waveguide with high responsivity and 15 GHz bandwidth are required to detect weak signals from an optical comb and second harmonic generator (SHG). Based on these PIN photodiode results, I optimized the bonding process and the photodiode structure and finally achieved higher responsivity and higher bandwidth with MUTC photodiodes.

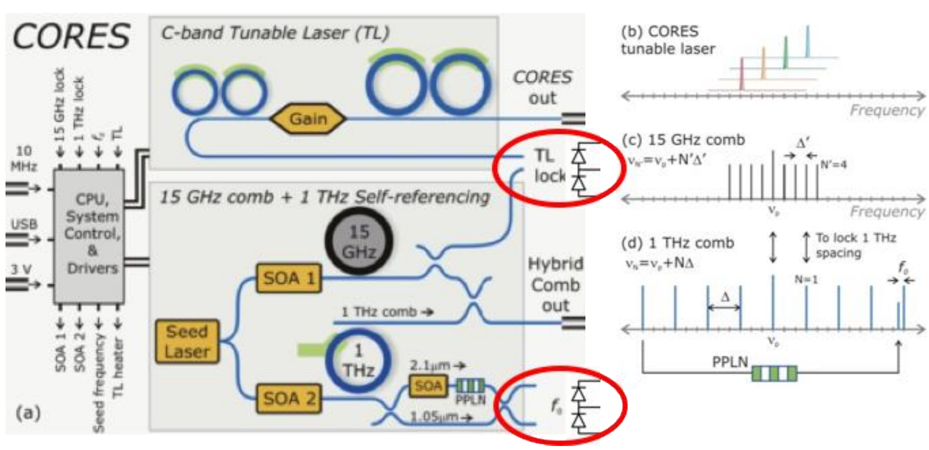

Fig. 5-1 Frequency synthesizer system design.

5. 2 PIN photodiode design

The Si_3N_4 strip waveguides were deposited by our collaborator Ligentec using low pressure chemical vapor deposition (LPCVD) with a thickness of 400 nm and widths of 1, 2 and 4 μm. The thicknesses of the top and lower SiO_2 claddings were 3 μm and 4 μm, respectively. The 3 μm top cladding is too thick to achieve efficient coupling. For bonding the InGaAs/InP photodiode material, the top SiO_2 cladding was selectively reduced to around 80 nm in an area of 6.5 x 5.5 mm^2 which defined the bonding window. Schematic cross sections and an illustration of the chip are shown in Figs. 5-2 and Fig. 5-3. The PD structure was grown on a 2″ InP wafer and included a 200 nm-thick P-doped InP contact layer, a 1250 nm-thick InGaAs absorption layer, and a 600 nm-thick N-doped InP contact layer as shown in figure 5-4. Low-temperature adhesive bonding described in last chapter was used to attach the 5 x 4 mm^2 die with the epitaxial photodiode layer stack in the bonding window (Fig. 5-5(a) and (b)). The thickness of the SU-8 (refractive index: 1.57 at 1550 nm) bonding layer was expected around 100 nm resulting in 180 nm distance between Si_3N_4 waveguide and photodiode layers. After InP substrate removal by hydrochloric acid, I used conventional wet etching techniques to fabricate double mesa single and balanced photodiodes. Microwave probe pads were deposited on SiO_2 and connected to the PD contact metals through air-bridges. An image of the fabricated chip is shown in Fig. 5-5 (c).

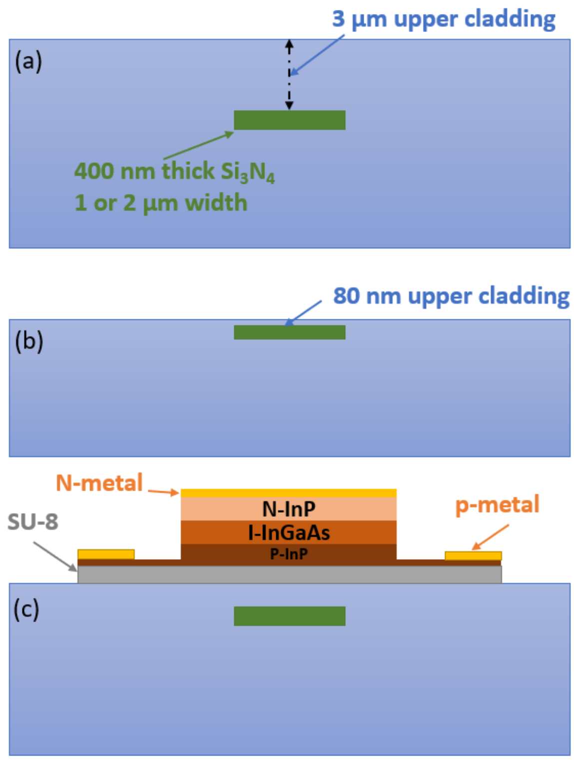

Fig. 5-2 Schematics of (a) Si_3N_4 waveguide, (b) Si_3N_4 waveguide with reduced top cladding, and (c) integrated photodiode.

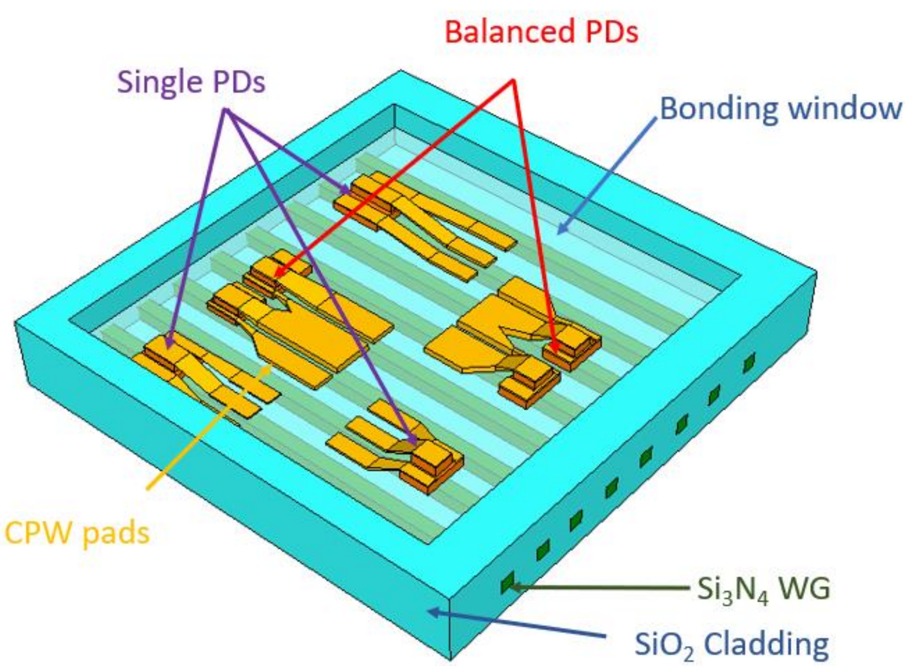

Fig. 5-3 Schematic overview of the chip.

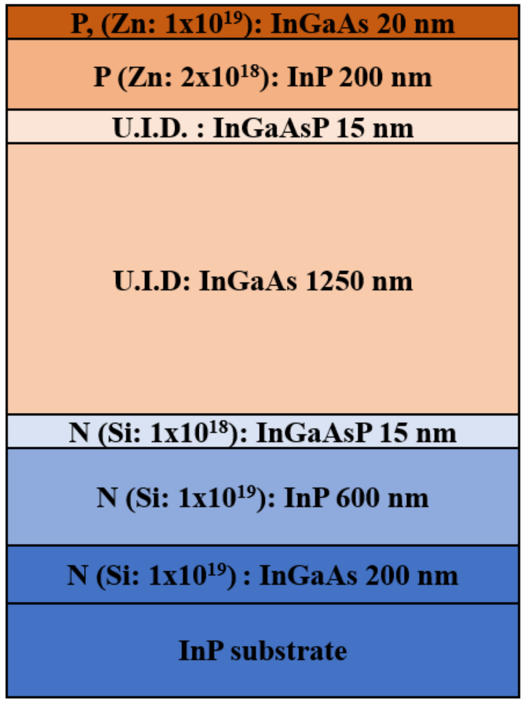

Fig. 5-4 Epitaxial layer structure of PIN photodiode on silicon nitride with doping concentrations in cm^{-3}.

Fig. 5-5 (a) chip with patterned waveguides, and (b) after InGaAs/InP die bonding; (c) finished chip with heterogeneous photodiodes.

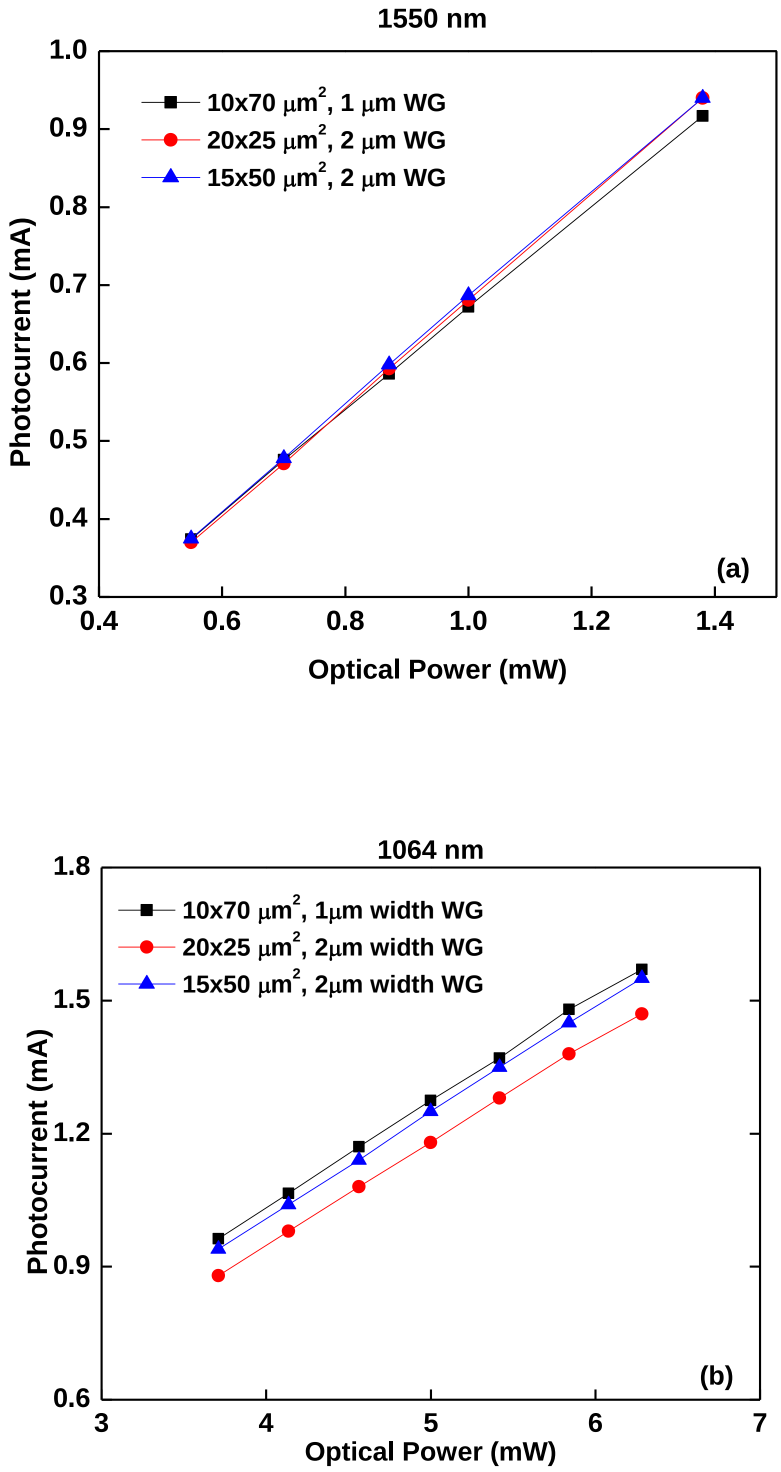

Fig. 5-6. Measured photocurrent vs. fiber-coupled input optical power for different PDs with different dimension (width x length). (a) Laser wavelength 1550 nm, (b) Laser wavelength 1064 nm.

The responsivities at 1550 nm and 1064 nm were both measured with single mode tapered fibers with a spot size of 2.5 μm. The fiber-coupled responsivities for a 25 μm long PD were 0.68 A/W and 0.24 A/W at 1550 nm and 1064 nm, respectively. From Fig. 5-6 (a), it can be found that the responsivity at 1550 nm did not have a strong dependence on the PD length implying that even shorter PDs with similar responsivity should be possible. At 1064 nm, the optical mode in the Si_3N_4 waveguide is more confined which makes the coupling into the absorption layer less efficient than at 1550 nm. This explains why photocurrent scales with photodiode length for a given optical input power in Fig. 5-6 (b). A maximum responsivity of 0.26 A/W was measured for a 10 x 70 μm^2 PD. I found no significant difference between PDs on 1 μm and 2 μm-wide Si_3N_4 waveguides in this measurement. The fiber-chip coupling loss was determined from simulations and was 0.7 dB at 1550 nm and 4 dB at 1064 nm. This large difference is due to a stronger mode confinement at shorter wavelengths, which results in smaller mode size and thus larger mismatch with the 2.5 μm input spot. Once I took the coupling loss into account, the internal responsivities were 0.8 A/W and 0.6 A/W, corresponding to 64% and 69% internal quantum efficiency at 1550 nm and 1064 nm, respectively. The polarization dependent loss was 0.45 dB at 1550 nm and only 0.08 dB at 1064 nm for PDs on 2 μm wide Si_3N_4 waveguides.

In my design, I also included some balanced photodiodes. Balanced photodiodes are two PDs configured in an anti-parallel way with the result that common mode input signals are suppressed while differential mode input signals are added up. Hence, a balanced PD has the potential to cancel common mode relative intensity noise (RIN) and amplified spontaneous emission (ASE) noise. As shown in Fig. 5-7 (a), the dark currents of both photodiodes (PD1 and PD2) in a balanced photodetector were 10 nA at 4 V reverse bias. A relatively large series resistance around 1.25 kΩ can be derived from the curves in forward bias, which is due to a relatively low doping level (1 x

$10^{18}/cm^3$) in the P-doped contact layer. Nevertheless, and as shown in Fig. 5-7 (b), a bandwidth of 7 GHz was achieved for both 20 x 10 um^2 PDs under large-signal modulation using an optical heterodyne setup at 1550 nm wavelength. A higher bandwidth can be expected once the series resistance is reduced by using a higher doping in the contact layer.

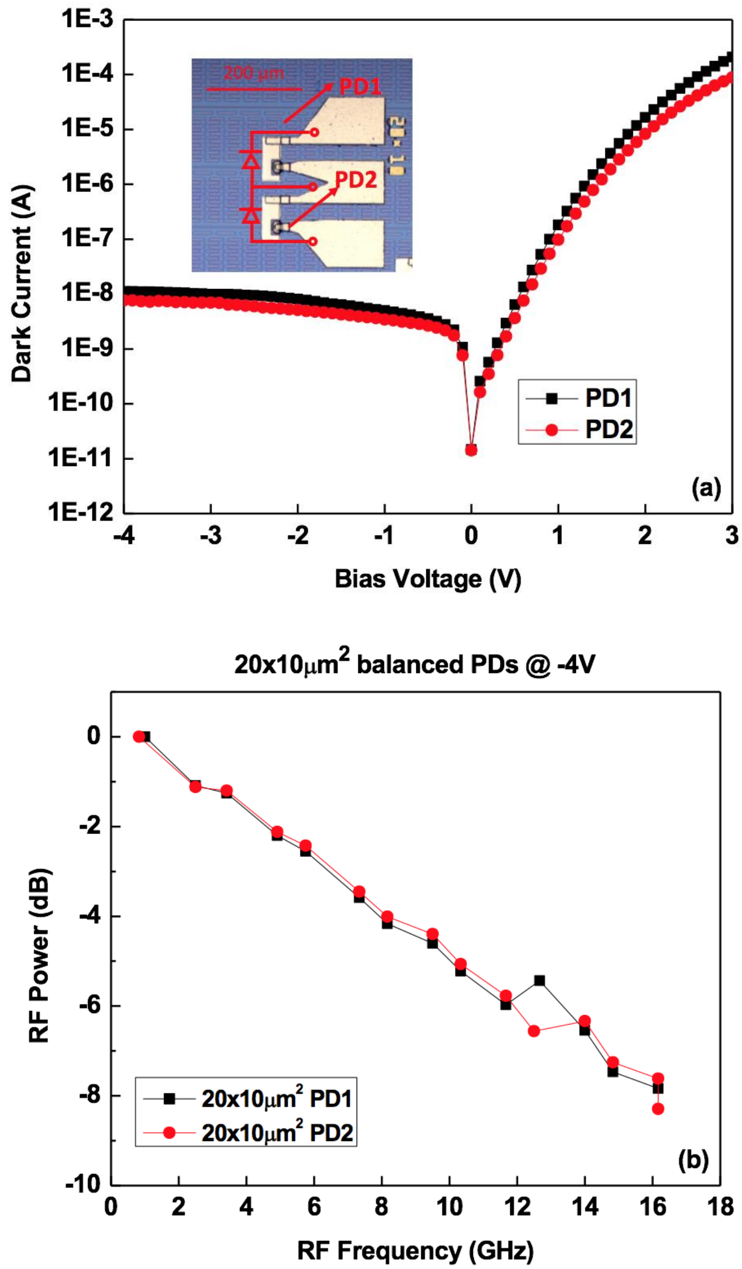

Fig. 5-7. (a) Dark I-V curves of PD1 and PD2 in the balanced photodetector; the inset shows a balanced PD pair; (b) Measured frequency responses of both PDs with an active area of 20 x 10 μm^2 at 0.1 mA and -4V.

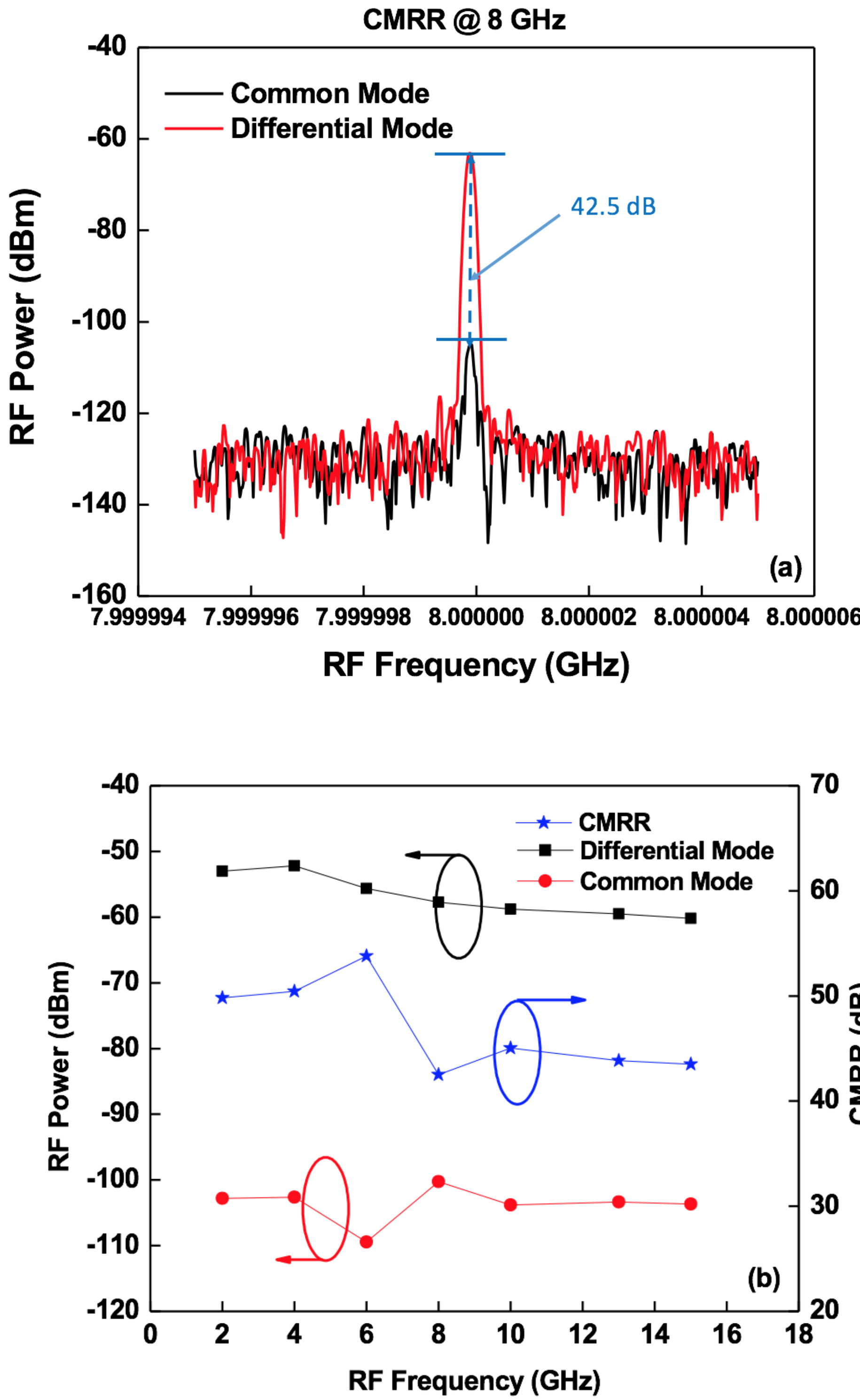

Fig. 5-8 (a) Common mode and differential mode RF powers at 8 GHz, (b) Common and differential mode powers and CMRR from 2 GHz to 15 GHz.

In order to characterize the common mode rejection ratio (CMRR) at 1550 nm, light was modulated by an optical modulator and split by a fiber-based 3 dB coupler into two branches before being launched into the waveguides of PD1 and PD2 through a fiber array. We used variable optical delay lines in both branches to adjust the RF phase of the modulated optical signal to be either in phase (common mode) or out of phase (differential mode). The CMRR was then calculated by subtracting the measured power in common mode from the power in differential mode. Figure 5-8 (a) shows the RF powers in common and differential modes at 8 GHz as measured with an electrical spectrum analyzer indicating a CMRR of 42.5 dB. As shown in Fig. 5-8 (b), the CMRR of the balanced photodetector was characterized from 2 GHz to 15 GHz with 0.1 mA photocurrent and 4 V reverse bias. The differential mode bandwidth agreed well with our bandwidth measurements that were obtained from individual measurements of PD1 and PD2. The CMRR was 50 dB within the 3-dB bandwidth and over 40 dB up to 15 GHz indicating an excellent symmetry of both PDs.

5. 3 Optimization of the bonding process

In the previous section, a photodiode on Si_3N_4 with record-high responsivity has been demonstrated. However, there are still some issues regarding the bonding stability that will be addressed in the following sections.

Bonding process

One issue is the SU-8 thickness. The SEM image of the photodiode's cross-section is shown in figure 5-9. The SU-8 thickness is verified to be 120 nm, which is thicker than what I expected. A second issue were bubbles, caused by outgassing, which appeared after the post-baking process during photolithography as shown in figure 5-10. These phenomena indicated that the SU-8 has not been cured well enough in the bonding process. During the photodiode fabrication process, it is necessary to etch away most of III-V in order to isolate every photodiode from others. After this process the SU-8 layer can be seen under the microscope as shown in figure 5-11. It can be seen from the interference pattern that the SU-8 thickness may not be uniform after the bonding process which further verifies the assumption that the SU-8 was not well cured.

In order to optimize the bonding process, the SU-8 exposure time, the post bake time, and outgassing and bonding times have been extended moderately to ensure that the SU-8 is completely cured during the bonding process. By using the optimized process described in Appendix III, the SU-8 bonding layer is more uniform and smoother as shown in figure 5-12. It is worth mentioning that surface treatment is very crucial to the bonding process since SU-8 is hardly spread evenly on a hydrophobic surface. O_2 plasma activation can help making the silicon nitride chip and the III-V die to be hydrophobic, which in turn makes the SU-8 smoothly coated on the sample.

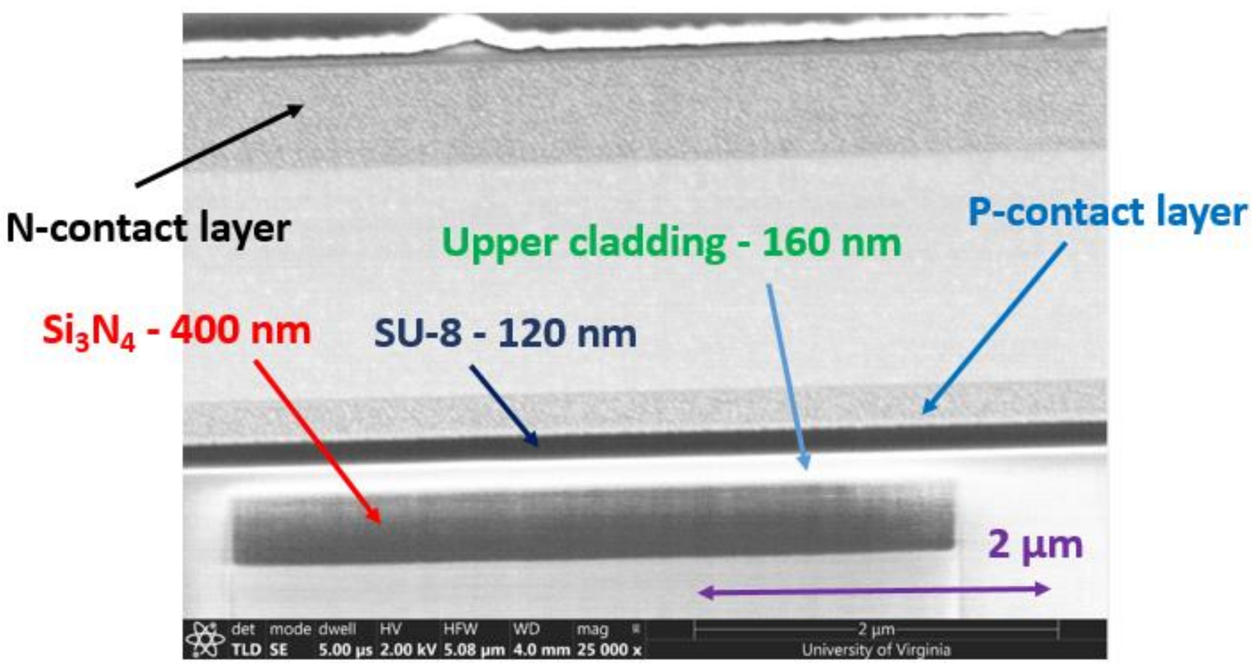

Fig. 5-9 SEM image of photodiode cross-section.

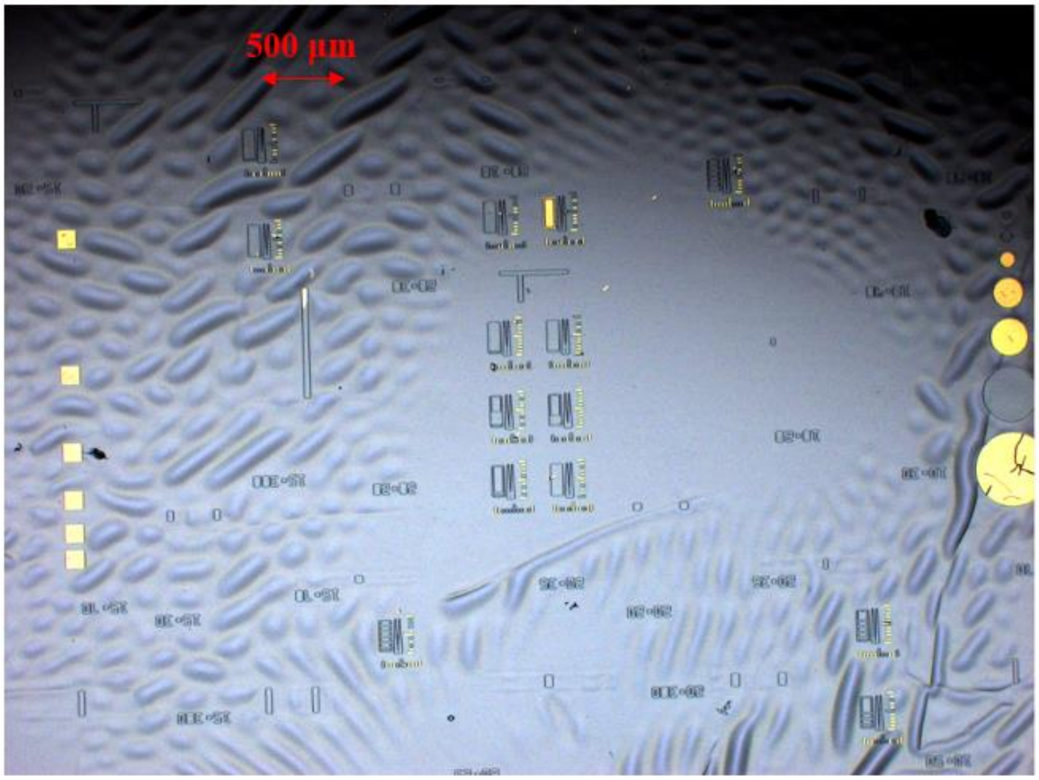

Fig. 5-10 Bubbles appeared after post-bake during the photolithography process.

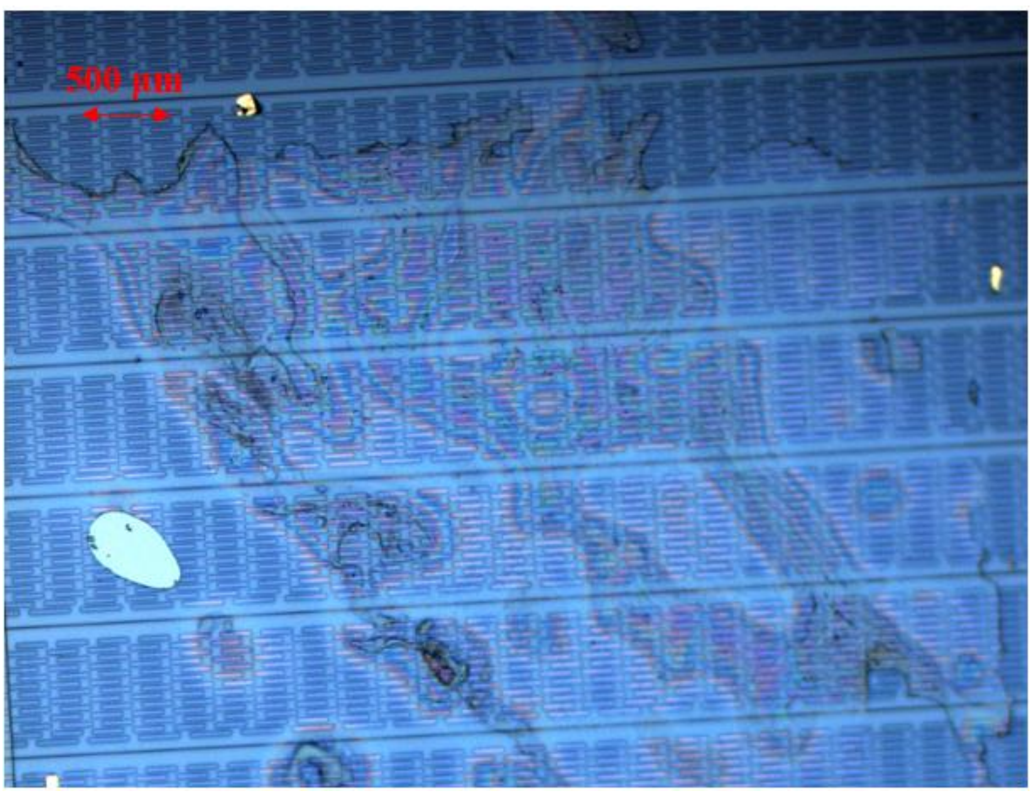

Fig. 5-11 SU-8 bonding layer after etching away the III-V die. The process is described in Appendix II.

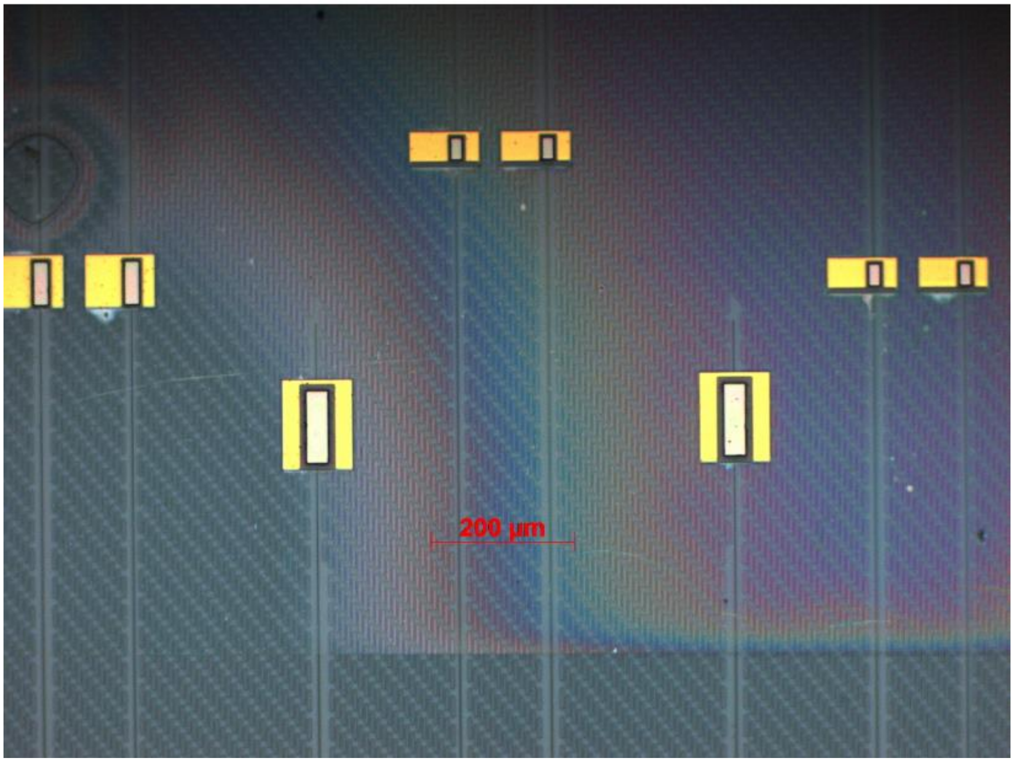

Fig. 5-12 SU-8 bonding layer after etching away the III-V die with the process shown in Appendix III.

Etching process

For the silicon nitride chip, a SiO_2 hard mask cannot be used due to the fact that SiO_2 is also used as the waveguide cladding. Hence, it is difficult to control precisely the dry etching process without harming the cladding of the silicon nitride waveguide. To address this, I adopted a wet etching process for the PIN photodiodes. However, InP cannot be etched isotropically in any acid. The PIN photodiode after wet etching is shown in figure 5-13. From the figure, it can be seen that the mesa width shrank from 10 µm to 7 µm. This under-cut makes it very difficult to fabricate small sized photodiodes. In order to overcome the issue, I developed a method using palladium (Pd) as the hard mask. The etching rate of Pd is below 5 nm/min when using the mesa etching recipe (see Chapter 2) in 200 W ICP. In the following run, 80 nm Pd was added during the N-metal deposition to be used as the hard mask. The total metal stack is AuGe/Ni/Au/Pd with thicknesses of 30 nm, 20 nm, 80nm and 80 nm, respectively.

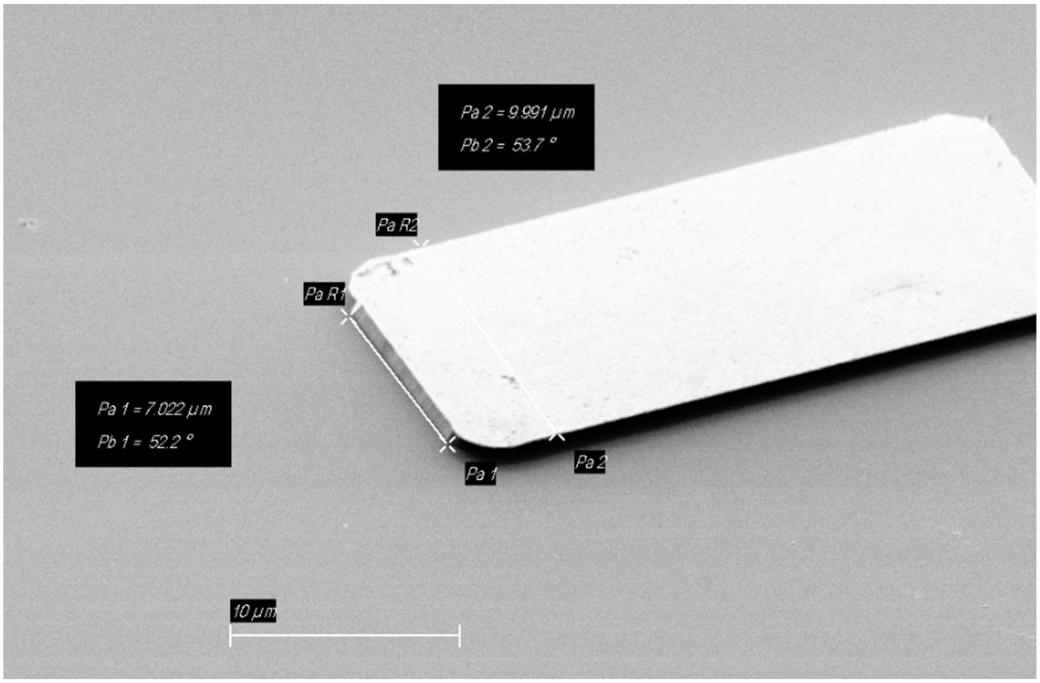

Fig. 5-13 SEM image of photodiode mesa after wet etching.

Responsivity and bandwidth

The bandwidth of the previously described PIN photodiode was only 7 GHz which is below the expected 20 GHz. This is caused by the 200 nm P contact InP layer, which causes high contact resistance and sheet resistance. I proposed several ways to further improve the bandwidth performance. For instance, it can be improved by using a MUTC structure instead of the PIN structure, which allows for having a thicker P-contact layer for better sheet resistance and changing the P-contact layer to be InGaAs. Due to concerns of loss in responsivity by changing the P-contact layer to be InGaAs, I decided to design a MUTC structure with thick P-contact layer.

The MUTC epitaxial structure with 400 nm P-contact layer bonded on the silicon nitride waveguide is shown in figure 5-14. The SU-8 thickness and SiO_2 cladding layer are set to be 120 nm and 160 nm, respectively, which are consistent with the previous SEM results in Fig. 5-9. In the design process, the thicknesses of the absorber and the drift layer were the variables determining photodiode responsivity.

Figure 5-15 shows the simulated quantum efficiency of a 10 x 50 μm^2 photodiode using the layer structure in Fig. 5-14. The color bar on the right indicates the residual optical power at the end of the photodiode. That means, the lower the residual power, the higher the quantum efficiency assuming that all lost photons are converted to electron hole-pairs. From the figure, it can be seen that the purple regions define the parameter space for achieving high quantum efficiency photodiodes. At the same time, the RC limited bandwidth and the transit time limited bandwidth also need to be taken into consideration. The drift layer can neither be too thin in order to achieve high RC limited bandwidth nor too thick for high transit-time limited bandwidth. Once taking this trade-off into account, I chose the final design to be a photodiode with 450 nm thick absorber (Thick_I) and 820 nm drift layer (Thick_N). The simulated transit time limited bandwidth of this structure is 40 GHz.

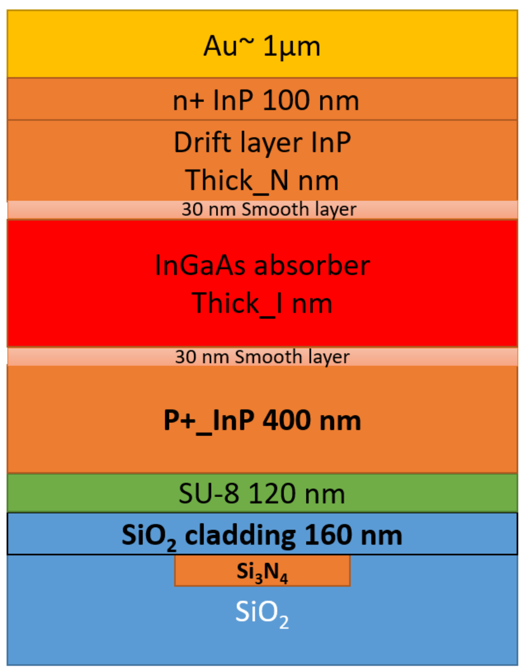

Fig. 5-14 New MUTC structure with variable thicknesses of absorber (Thick_I) and drift (Thick_N) layers.

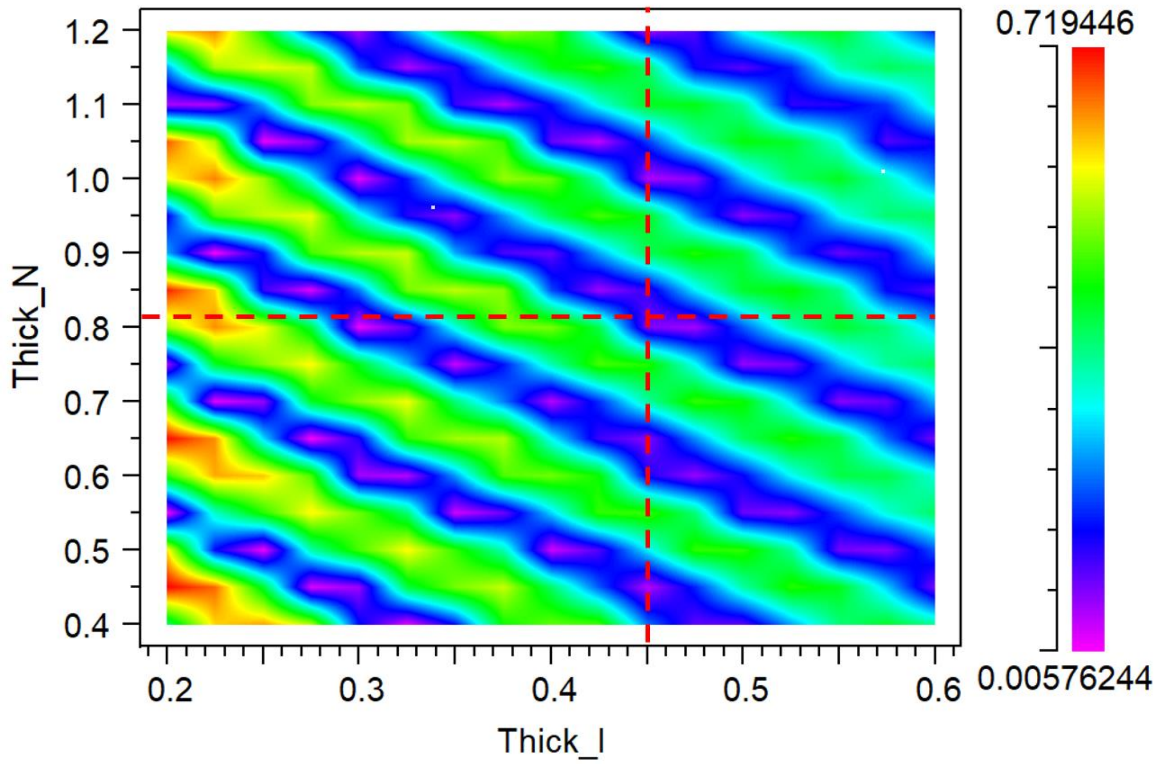

Fig. 5-15 Simulated residual power as function of various thicknesses of absorber and drift layer in MUTC PD. The red dashed lines point out the final design.

Once setting down the thicknesses of the absorber and the drift layer, I also investigate the thickness of SU-8 bonding layer and top cladding layer for optical coupling. In Fig. 5-16 and Fig. 5-17, the simulated structure and a result with various thicknesses of SU-8 and silica top cladding are shown. From the figures, it can be concluded that both, a thinner SU-8 bonding layer and a thinner silica top cladding layer are always desirable to achieve high QE. Specifically, a high quantum efficiency photodiode up to 70% can be achieved once the total thickness of SU-8 and top cladding layer is below 250 nm for a 10 x 50 μm^2 photodiode.

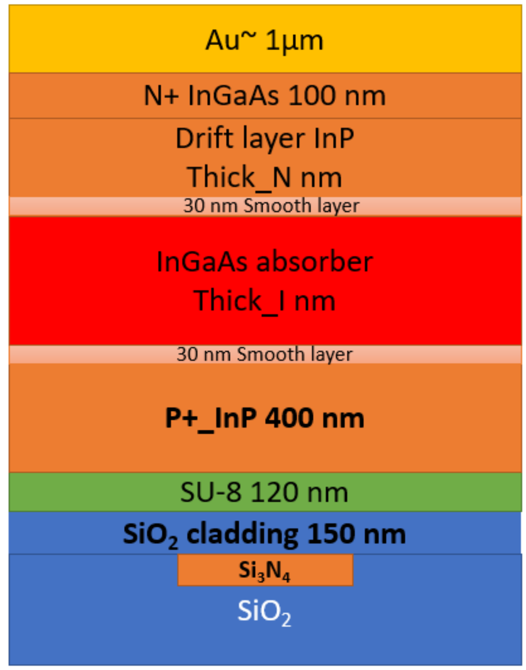

Fig. 5-16. MUTC epitaxial structure with various thicknesses of SU-8 (Thick_SU8) and SiO_2 top cladding (Thick_cladding) layers.

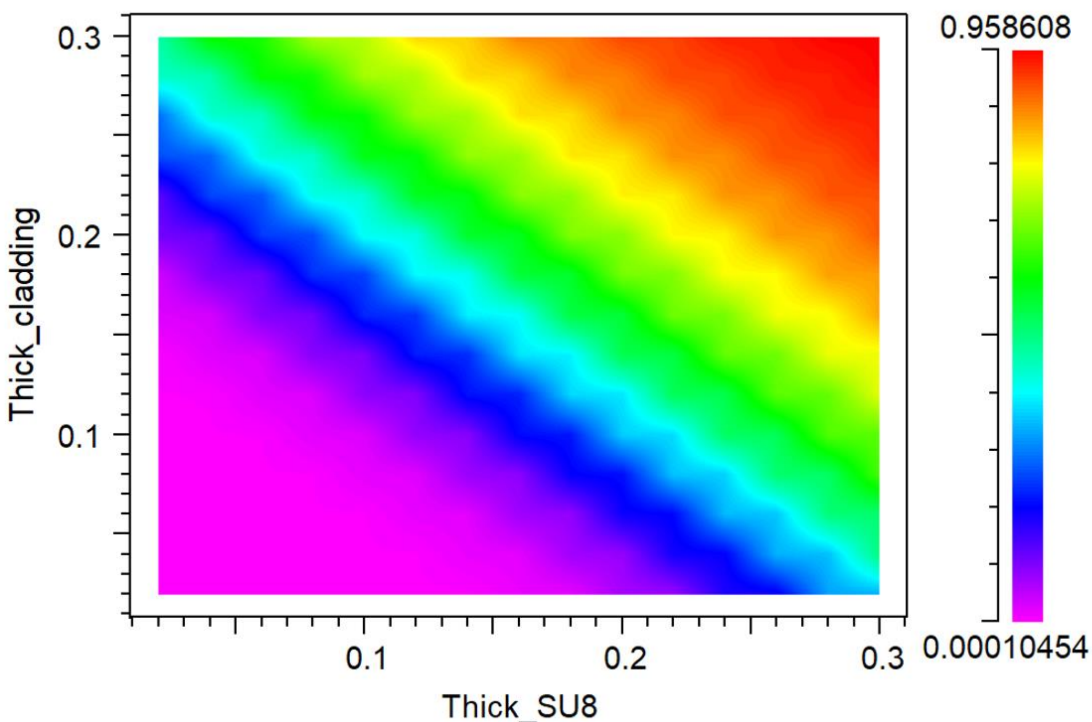

Fig. 5-17 MUTC simulated residual power as function of SU-8 bonding layer thickness and SiO_2 top cladding layer thickness.

5. 4 MUTC photodiode on silicon nitride waveguide

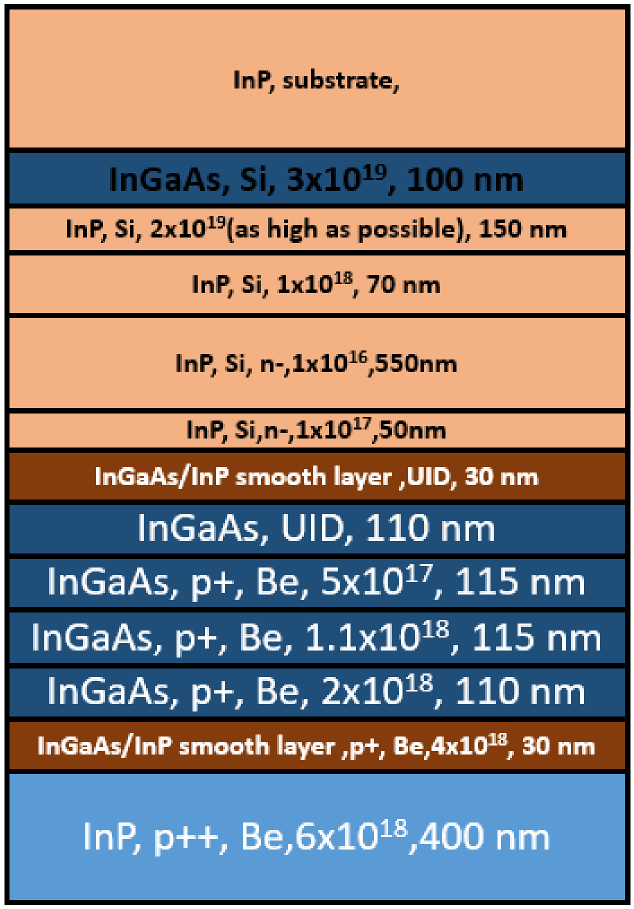

Fig. 5-18 epitaxial structure of PD with doping concentrations in cm^{-3}.

The designed MUTC PD's epitaxial structure is shown in Fig. 5-18. The layers were grown on semi-insulating InP substrate and consist of a 150 nm-thick N-type doped InP contact layer, a 400 nm P-type doped InP contact layer, a depleted InP electron drift layer, and a 450 nm-thick InGaAs depleted and un-depleted absorption layer. According to my simulation, the carrier transit-time limited bandwidth for this MUTC PD is 40 GHz. As described in Appendix III, an optimized adhesive bonding technique including SU-8 spin coating (SU-8 thickness 70 nm), soft bake at 110 ºC for 40s, 16 seconds UV exposure followed by a 40-minutes outgas, and curing at 130 ºC under 10 psi for 60 min was adopted to integrate an InGaAsP/InP die onto the bonding window.

Then, a mixture of hydrochloric acid and DI water was used to remove the InP substrate. MUTC PDs were fabricated as double mesa structures by conventional dry and wet etching techniques. Ground-signal-ground (GSG) microwave probe pads were deposited and connected to the PD N-contact through an Au electro-plated air-bridge. Figure 5-19 shows the finished MUTC PDs with single (Fig. 5-19(a)) and balanced (Fig. 5-19 (b)) PDs fabricated on the same chip. A scanning electron microscope (SEM) picture of the PD's cross-section with a 4 µm-wide waveguide and 69 nm-thick SU-8 layer is shown in Fig. 5-19 (c).

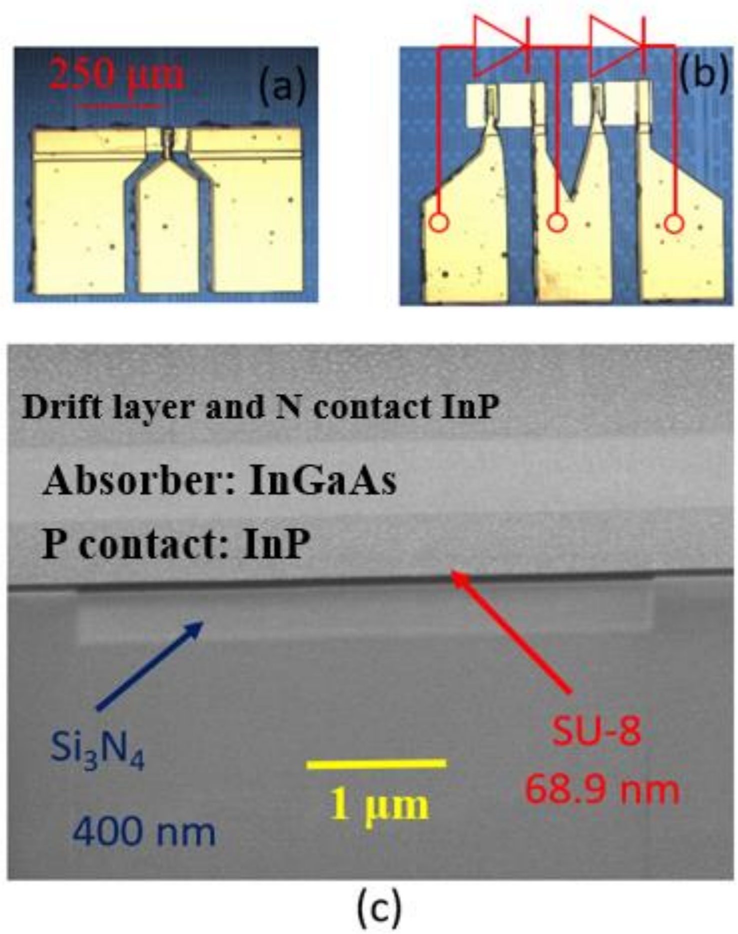

Fig. 5-19 Microscope pictures of (a) single PD and (b) balanced PDs with circuit representation; (c) SEM picture of the PD's cross-section.

5. 5 MUTC results and discussion

Typical dark currents were around 20 nA at 8 V reverse voltage. Figure 5-20 shows the current-voltage characteristics for a pair of balanced PDs. It should be mentioned that the dark currents of our heterogeneous PDs are at the same level or below as similar devices on native substrate [5.17]. One of the benefits of the Si_3N_4 platform is its wide transparency window. To this end we characterized the responsivities of the PDs at wavelengths of 1550 nm and 1064 nm. The waveguides were input-coupled by single mode tapered fibers with a spot size of 2.5 µm optimized for 1550 nm and 1064 nm, respectively. The Si_3N_4 waveguides have inverse tapers at the chip facets to aid with the input coupling. According to our simulation, the fiber-chip coupling loss due to mode mismatch is 0.7 dB at 1550 nm and 4 dB at 1064 nm, respectively. Based on these values,

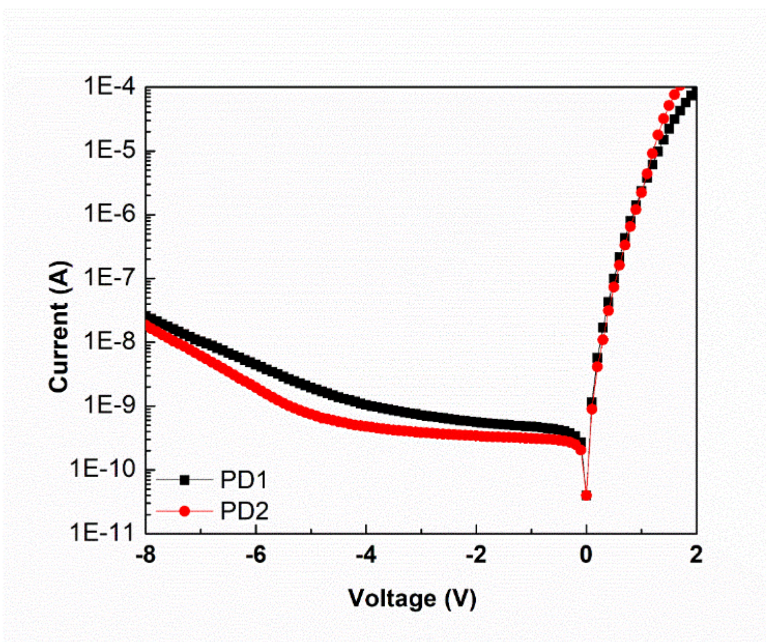

Fig. 5-20 Dark current measurements of a pair of balanced PDs.

the blue solid lines in Figs. 5-21 and 5-22 illustrate the PD's external (fiber-coupled) responsivities corresponding to 100 % internal quantum efficiency. The red symbols in Figs. 5-21 and 5-22 show the measured data of different PDs. For a 30 µm-long PD, the measured external responsivities are

0.8 A/W and 0.33 A/W at 1550 nm and 1064 nm, respectively. Once we take the fiber input coupling loss into account, the internal responsivity is as high as 0.94 A/W and 0.83 A/W corresponding to 75 % and 96 % internal quantum efficiencies at 1550 nm and 1060 nm, respectively. The polarization dependence loss was measured to be only 0.67 dB and 0.26 dB at 1550 nm and 1064 nm, respectively. It should be mentioned that the responsivity has only a weak dependence on PD length between 20 μm and 60 μm. For a 10 μm-long PD, the external responsivity can be as high as 0.68 A/W at 1550 nm which indicates that most of the light is absorbed in the first 10 μm. Moreover, we found that the PD responsivity did not show any significant dependence on waveguide widths between 1 and 4 μm.

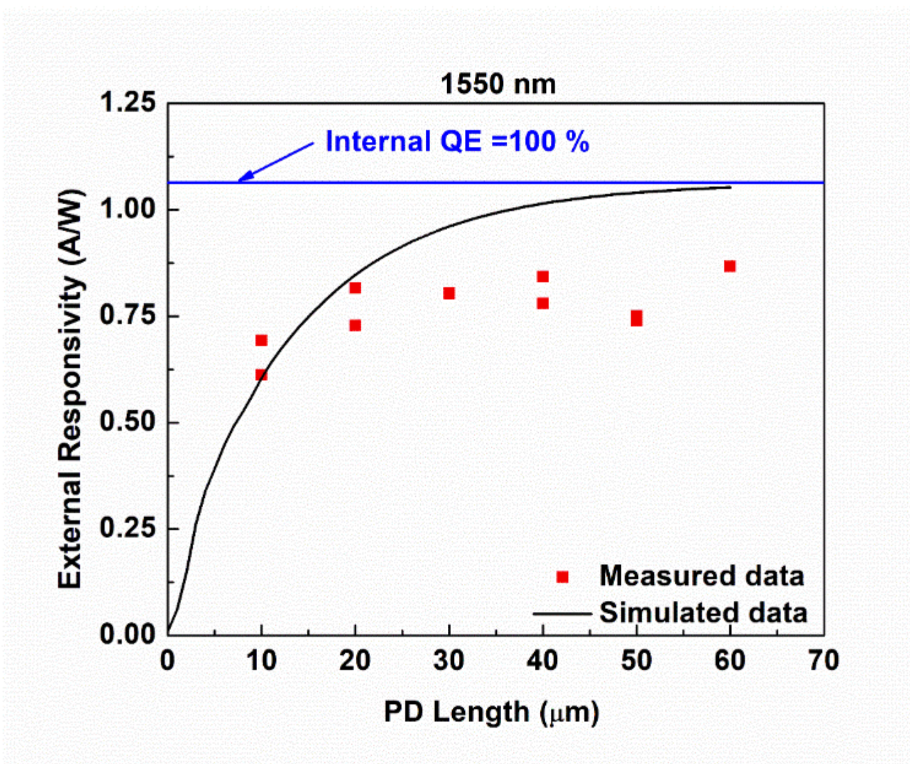

Fig. 5-21 Measured and simulated external responsivity for PDs of various lengths at 1550 nm at 8 V reverse bias.

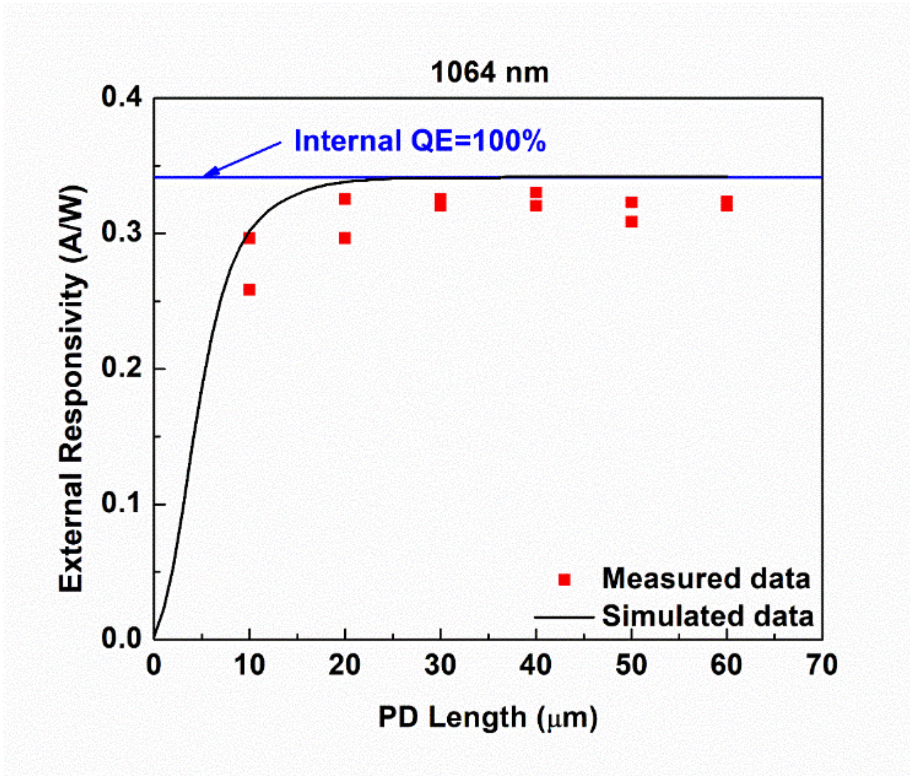

Fig. 5-22 Measured and simulated external responsivity for PDs of various lengths at 1064 nm at 8 V reverse bias.

In order to further study device characteristics, I used a commercial software and estimated the responsivity based on the total optical loss in the photodiode. In the simulation I used 7000 cm^{-1} (9000 cm^{-1}) and 870890 cm^{-1} (841632 cm^{-1}) as the absorption coefficients for InGaAs and gold at 1550 nm (1060 nm), respectively, and assumed all other layers to be transparent. By further assuming that all absorbed photons are converted into photocurrent, the black solid lines in Figs.5-21 and 5-22 illustrate the responsivity after considering the fiber-chip coupling loss. While the simulated curve matches well the measured data at 1064 nm (Fig. 5-22), we found that the simulation overestimates the responsivity by 20 % at 1550 nm and PD lengths larger than 40 μm. We believe that this discrepancy can be explained by the difference in optical mode intensity distributions in the PD. In Fig. 5-23, the mode intensity distributions in the PD at 1550 nm and 1064 nm are shown. As the index contrast between Si_3N_4 and silica is similar at these two wavelengths, the mode distributions in the PD region are strongly dependent on the wavelength. For our 400 nm thick Si_3N_4 waveguide, the mode at 1550 nm is less confined in the waveguide and extends significantly towards the top gold contact. The proximity with the metal creates additional optical loss, which, however, does not contribute to the photocurrent.

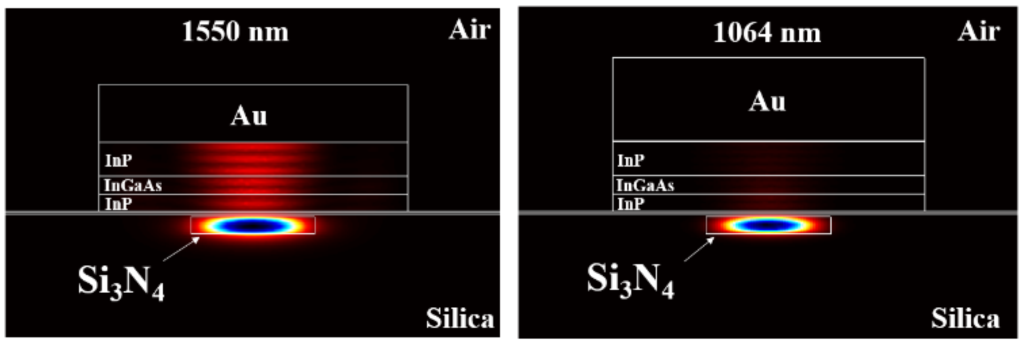

Fig. 5-23 Simulated mode intensity distributions in the PD at 1550 nm (left panel) and 1064 nm (right panel).

Using an optical heterodyne setup with modulation depth close to 100 %, the frequency responses of the PDs were measured (Fig. 5-24). For a 10×30 μm^2 PD, the bandwidth can reach 20 GHz at 8 V reverse bias with 2 mA photocurrent. For larger sized PDs, the bandwidth decreases due to the resistance-capacitance (RC) limit.

We also measured the non-return-zero eye diagram by using a 40 Gbit/s pseudo random binary sequence generator and a 40 GHz Mach-Zehnder (MZ) modulator as the signal source. The pattern length was 2^{31}-1. The output of our photodiode was connected to a high-speed sampling oscilloscope through a bias-T and a short RF cable. Figure 5-25 shows the detected eye diagrams using a PD with 10×30 μm^2 active area. We recorded a clearly opened eye pattern which demonstrates the PD's high-speed capability for 40 Gbit/s systems.

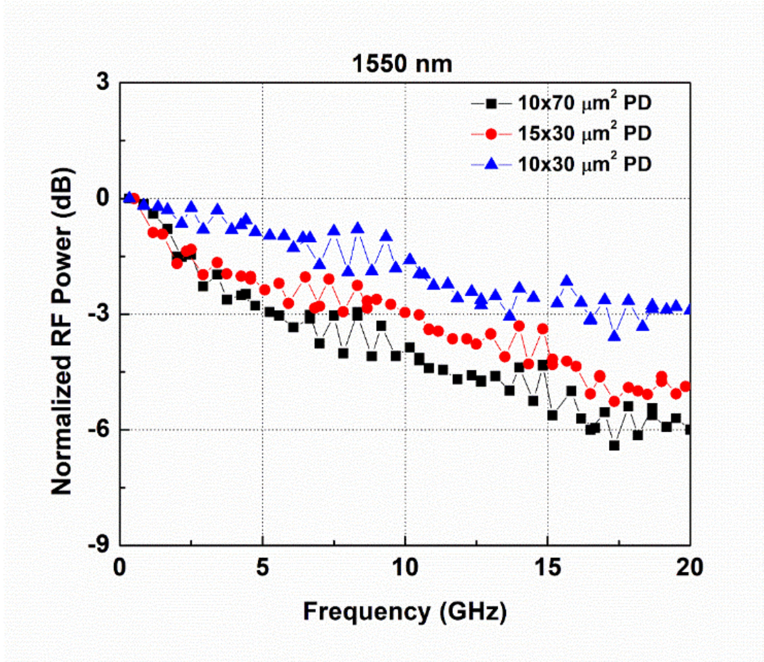

Fig. 5-24 Measured frequency responses of various sized PDs at 1550 nm with 8 V reverse bias and 2 mA photocurrent.

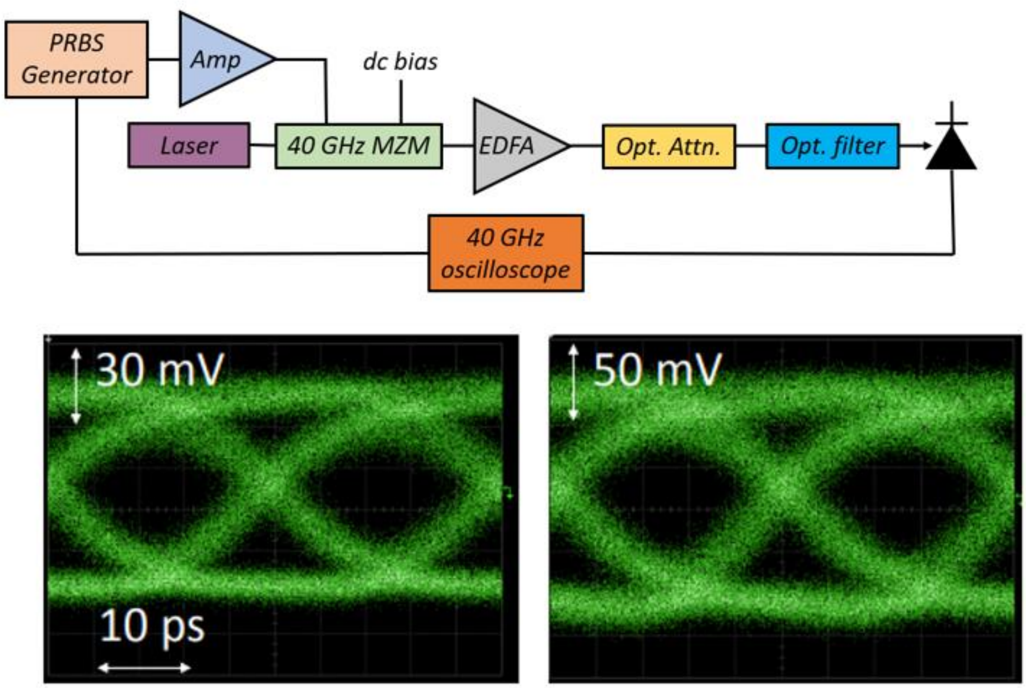

Fig.5-25 Eye diagram set-up and detected 40 Gbit/s eye diagram at 0.5 mA (left panel) and 2 mA (right panel) average photocurrents.

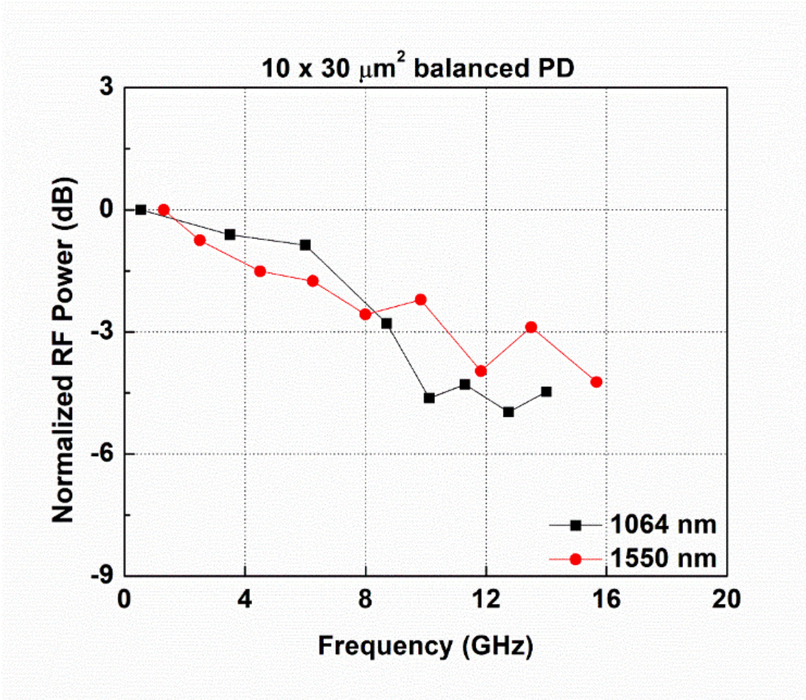

Fig. 5-26 Measured frequency responses of balanced PDs at 1550 nm and 1064 nm with 8 V reverse bias and 2 mA photocurrent.

It is well known that balanced photodiodes can suppress common mode noise and therefore can help to increase the signal to noise ratio. To measure the balanced photodetector performance, the optical heterodyne signal was split into two branches before being launched into the waveguides of both PDs, PD1 and PD2, through a fiber array. We used variable optical delay lines in both branches to adjust the radio frequency (RF) phase of the modulated optical signal to be either in-phase (common mode) or out-of-phase (differential mode). Figure 5-26 shows the frequency responses in differential mode for a $10 \times 30\ \mu m^2$ balanced PD pair at 8 V reverse bias and 2 mA photocurrent. The bandwidth is 10 GHz, half of the bandwidth of a single PD, which is expected due to the doubled capacitance of the PD pair. A similar measurement at 1064 nm showed no significant difference in bandwidth (Fig. 5-26).

To measure CMRR we replaced the optical heterodyne source by a Mach-Zehnder modulator. CMRR was calculated by subtracting the measured RF power in common mode from the RF power in differential mode. Figure 5-27 shows the RF powers in common and differential modes at 10 GHz as measured with an electrical spectrum analyzer indicating a CMRR of more than 40 dB at 1550 nm. As shown in Fig. 10, the CMRR for this balanced PD pair was larger than 30 dB from DC to 10 GHz which indicates excellent symmetry between PD1 and PD2.

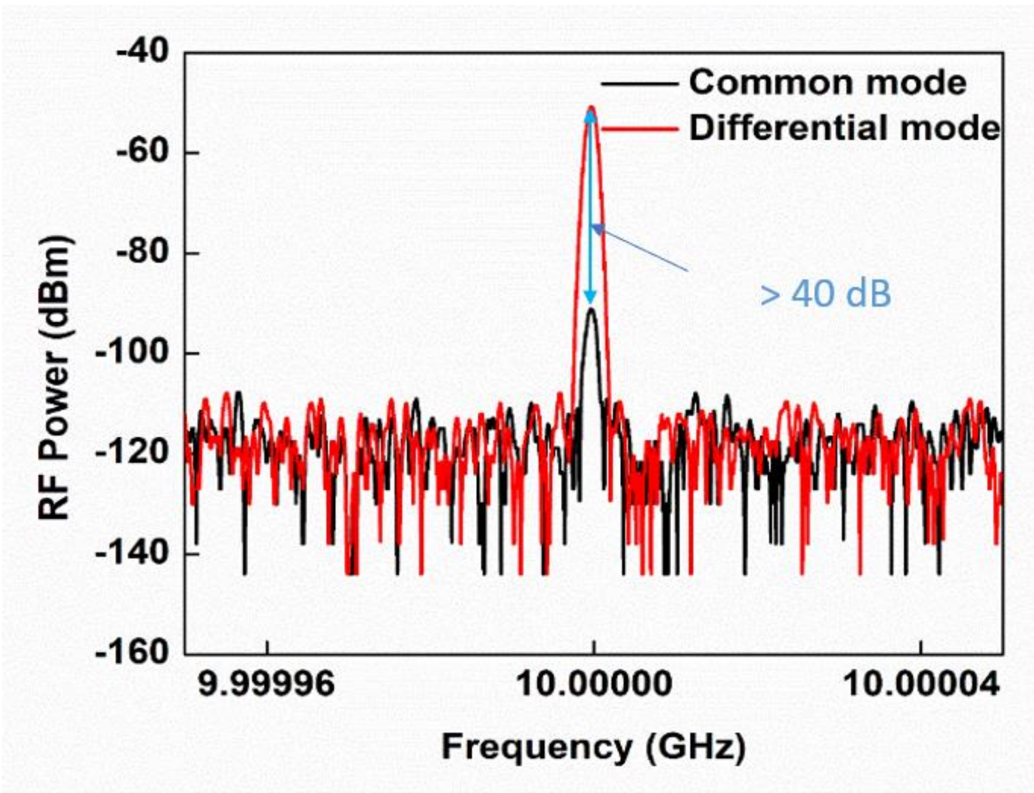

Fig. 5-27 Common and differential mode powers of balanced PDs at 10 GHz at 8 V reverse bias and 2 mA photocurrent for each PD at 1550 nm.

5.6 Summary

Detector structure	Measured external responsivity (A/W)	Bandwidth (GHz)	Dark Current
h-BN/MoS2/graphene	0.24	28	< 10 nA at 10 V
InGaAsP/InP MUTC	0.15	3.5	1 µA at 1 V
InGaAs/InP PIN	0.36	30	650 µA at 2 V
InGaAs/InP PIN	(0.68*)	25	2 nA at 4 V
InGaAs/InP PIN	**0.68**	**7**	**10 nA at 4 V**
InGaAsP/InP MUTC	**0.8**	**20**	**20 nA at 8 V**

Table 5-2 Optical detectors on Si_3N_4 waveguide at 1550 nm wavelength reported in the literature. (*): Estimated internal responsivity. Results of my work in bold.

In this chapter, record-high responsivity PIN photodiodes on silicon nitride were fabricated and characterized. By further optimizing the epi-structure, the bonding and fabrication process, an even higher responsivity photodiode with 20 GHz bandwidth has been demonstrated. Table 5-2 shows the results of my work compared to the state-of-the-art reported in the literature. Low dark current, a record-high responsivity and a bandwidth of 20 GHz have been achieved. Based on their excellent performance, our heterogenous MUTC photodiodes are promising candidates for high-speed Si_3N_4 photonic integrated circuit applications.

References

[5.1] C. R. Doerr, "Silicon photonic integration in telecommunications," Frontiers in Physics **3** (2015), 37.

[5.2] D. V. Katrien, I. Bartolozzi, E. Schacht, P. Bienstman, and R. Baet, "Silicon-on-Insulator microring resonator for sensitive and label-free biosensing," Opt. Express **15**(12), 7610-7615 (2007).

[5.3] Poloti, M. J. Cryan, J. G. Rarity, S. Yu, and J. L. O'brien, "Silica-on-silicon waveguide quantum circuits," Science **320**(5876), 646-649 (2008).

[5.4] G. H. Roeloffzen, L. Zhuang, C. Taddei, A. Leinse, R. G. Heideman, P. W. L. van Dijk, R. M. Oldenbeuving, D. A. I. Marpaung, M. Burla, and K. J. Boller, “Silicon nitride microwave photonic circuits;” Opt. Express **21**(19), 22937-22961 (2013).

[5.5] Blumenthal, R. Heideman, D. Geuzebroek, A. Leinse, and C. Roeloffzen, “Silicon nitride in silicon photonics,” Proceedings of the IEEE **106**(12), 2209-2231 (2018).

[5.6] M. Piels, J. F. Bauters, M. L. Davenport, M. JR. Heck, and J. E. Bowers, “Low-loss silicon nitride AWG demultiplexer heterogeneously integrated with hybrid III–V/silicon photodetectors,” Journal of Lightwave Technology **32**(4), 817-823 (2013).

[5.7] M.H. Pfeiffer, J. Liu, M. Geiselmann, T.J Kippenberg, “Coupling ideality of integrated planar high-Q microresonators,” Physical Review Applied **7**(2), 024026 (2017).

[5.8] Y. Xuan, Y. Liu, L. T. Varghese, A. J. Metcalf, X. Xue, P. Wang, K. Han, J. A. Jaramillo-Villegas, A. A. Noman, C. Wang, S. Kim, M. Teng, Y. J. Lee, B. Niu, L. Fan, J. Wang, D. E. Leaird, A. M. Weiner, and M. Qi, “High-Q silicon nitride microresonators exhibiting low-power frequency comb initiation,” Optica **3**(11), 1171- 1180 (2016).

[5.9] A. L. Gaeta, M. Lipson, and T. J. Kippenberg, “Photonic-chip-based frequency combs,” Nature Photonics **13**(3), 158 (2019).

[5.10] R. Halir, Y. Okawachi, J. S. Levy, M. A. Foster, M. Lipson, and A. L. Gaeta, “Ultrabroadband supercontinuum generation in a CMOS-compatible platform,” Opt. Letters **37**(10), 1685-1687 (2012).

[5.11] D.D. Hickstein, G.C. Kerber, G.C., D.R. Carlson, L. Chang, D. Westly, K. Srinivasan, A. Kowligy, J.E. Bowers, S.A. Diddams, and S.B. Papp, “Quasi-phase-matched supercontinuum generation in photonic waveguides,” Physical review letters, **120**(5), p.053903 (2018).

[5.12] C. J. Krückel, P. A. Andrekson, D. T. Spencer, J. F. Bauters, M. JR. Heck, and J. E. Bowers, “Continuous wave-pumped wavelength conversion in low-loss silicon nitride waveguides,” Opt. Letters **40**(6), 875-878 (2015).

[5.13] D. T. Spencer, T. Drake, Travis C. Briles, J. Stone, L. C. Sinclair, C. Fredrick, Q. Li, D. Westly, B.R. llic, A. Bluesone, N. Volet, T. Komljenovic, L. Chang, S. Lee, D. Y. Oh, M. Suh, K. Y. Yang, M. H. P. Pfeiffer, T. J. Kippenberg, E. Norberg, L. Theogarajan, K. Vahala, N. R. Newbury, K. Srinivasan, J. E. Bowers, S. A. Diddams,” An optical-frequency synthesizer using integrated photonics,” Nature **557**(7703), 81 (2018).

[5.14] Y. Gao, G. Zhou, H.K. Tsang, C. Shu, “High-speed van der Waals heterostructure tunneling photodiodes integrated on silicon nitride waveguides,” Optica **6**(4), 514-517 (2019).

[5.15] Y. Shen, S. Feng, X. Xie, J. Zang, S. Li, T. Su, K. Shang, W. Lai, G. Liu, S.J.B. Yoo, J.C. Campbell, “Hybrid integration of modified uni-traveling carrier photodiodes on a multi-layer silicon nitride platform using total reflection mirrors,” Opt. Express **25**(9), 9521-9527 (2017)

[5.16] P. R. A. Binetti, X. J. M. Leijtens, A. M. Ripoll, T. D. Vries, E. Smalbrugge, Y. S. Oei, L. Di Cioccio, J.-M. Fedeli, C. Lagahe, R. Orobtchouk, D. Van Thourhout, P.J. van Veldhoven, R. Nötzel, M.K. Smit, “InP-based photodetector bonded on CMOS with Si3N4 interconnect waveguides,” In 2009 IEEE LEOS Annual Meeting Conference Proceedings, pp. 139-140. IEEE, 2009

[5.17] Q. Li, K. Sun, K. Li, Q. Yu, P. Runge, W. Ebert, A. Beling, and J. C. Campbell,” High-power evanescently coupled waveguide MUTC photodiode with> 105-GHz bandwidth,” Journal of Lightwave Technology **35**(21), 4752-4757 (2017).

Chapter 6. High-quantum efficiency waveguide segmented photodetector

6. 1 Introduction

High speed and high quantum efficiency photodiodes are key devices in optical communications, sensing, and microwave photonics. To overcome the well-known bandwidth-efficiency trade-off in normal incidence PDs, side-illuminated or waveguide-photodiodes have been developed [6.1-6.2]. Waveguide PDs provide high responsivity and short carrier transit time since electrical and optical transports are not collinear. As most waveguide PDs are butt- or evanescently coupled, their responsivity primarily scales with the length of the absorption layer which can negatively impact the bandwidth and dark current in high-responsivity PDs.

In this chapter, I first describe a novel monolithically integrated InP-based PIN segmented waveguide photodetector consisting of 6 PDs that are coupled to one waveguide. Optical coupling from the waveguide into the PD absorber and back into the waveguide was accomplished by using a vertical directional coupler design. Light that is not absorbed by the first PD couples back into the waveguide and is absorbed in one of the following PDs. I show that the segmented photodetector can achieve near-unity quantum efficiency by using an array of 32 μm long photodiodes with an absorber thickness as small as 30 nm. This type of photodetector has applications in velocity-matched travelling wave PDs [6.3] and low dark-count photon-number resolving (PNR) detectors [6.4] which require minimized absorber volumes and high quantum efficiency.

After a proof-of-concept of this design, I propose a new avalanche photodiode (APD) design with AlInAsSb for over 50 PDs in series for a novel photon-number resolving system.

6. 2 Device design

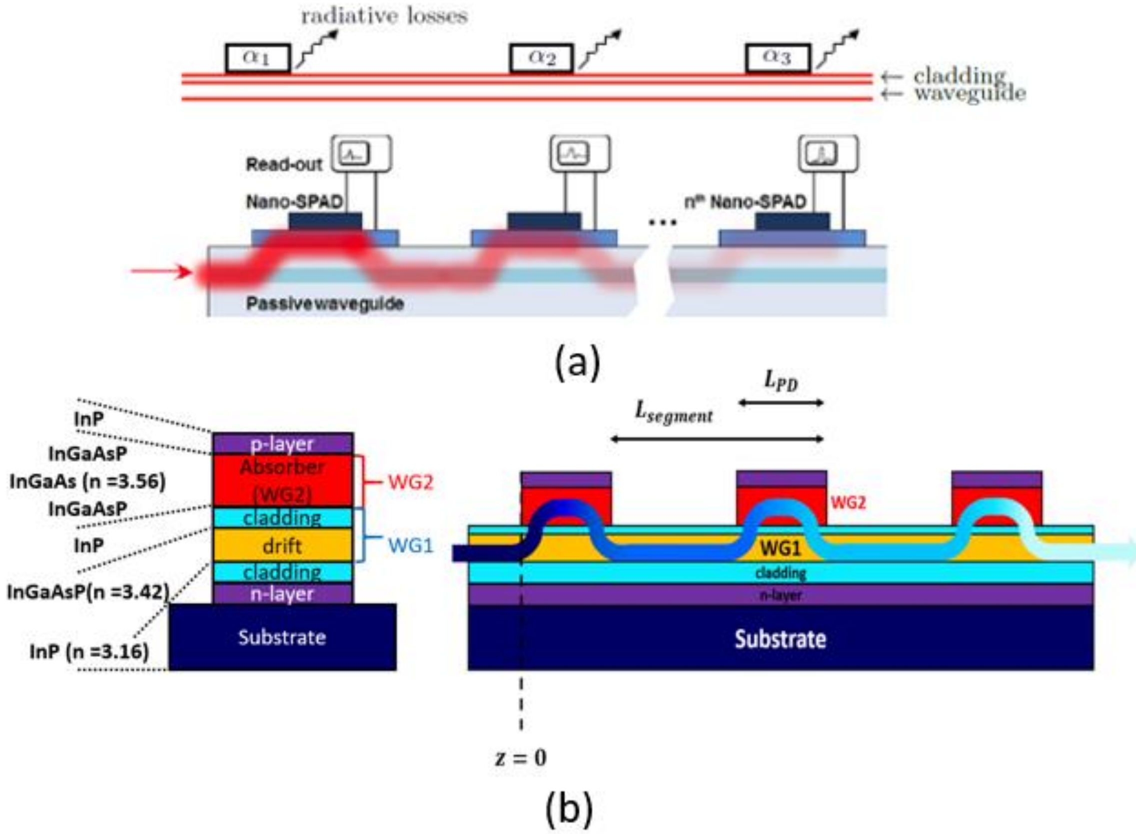

Fig. 6-1 (a) Proposed PNR system, (b) Cross-section of waveguide photodiode (left) and light propagating in the segmented waveguide photodetector (right).

In collaboration with Professor Olivier Pfister's group in physics, our group has proposed a novel PNR detector which is based on segmented waveguide PDs sharing same the waveguide while achieving high quantum efficiency in total as shown in Fig 6-1 (a). In such design, light should be absorbed in these segmented PDs with low radiation loss. Fig. 6-1 (b) shows the proposed PNR system and the designed photodiode cross-section. The passive waveguide (WG1) is embedded between two lower index cladding layers and serves as the input waveguide of the photodetector. The upper cladding layer is used to separate WG1 from the second waveguide, the absorption waveguide (WG2). Adding these extra layers does not sacrifice bandwidth performance because they serve as electron drift region similar to the collection layer in dual-depletion region [6.5] and uni-traveling carrier PDs [6.6]. The light coupling process in and out of the PD can be recognized as a co-directional coupler problem as illustrated in the figure. To ensure complete coupling, the goal is to achieve phase match, i.e. matching the propagations constants of the modes in WG1 and WG2.

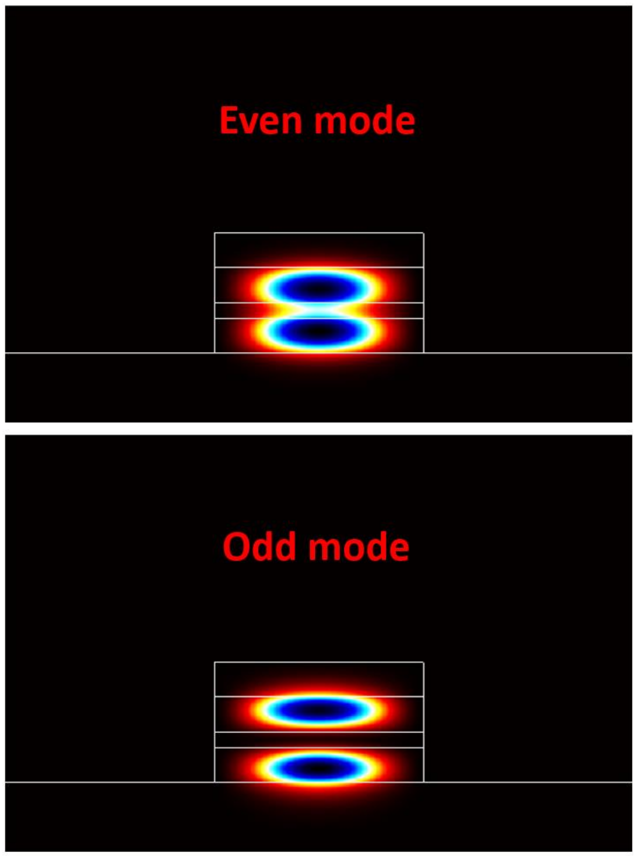

Fig. 6-2 Intensity distributions of the symmetric (even) and anti-symmetric (odd) supermodes in the cross-section.

Figure. 6-2 shows the intensity distribution of the symmetric (even) and anti-symmetric (odd) supermodes in the cross-section. Based on the theory of mode coupling [6.7-6.8], the field distribution $\emptyset_1(z)$ in WG1 and $\emptyset_2(z)$ in WG2 can be represented by adding the even mode field φ_e and the odd mode field φ_o [6.9]:

$$\emptyset_1(\mathrm{z}) = a_1\varphi_e \exp(-i\beta_e z) + a_2\varphi_o \exp(-i\beta_o z)$$

$$\emptyset_2(\mathrm{z}) = a_3\varphi_e \exp(-i\beta_e z) + a_4\varphi_o \exp(-i\beta_o z) \quad (6\text{-}1)$$

where βe and βo stand for the corresponding propagation constants of these two modes and a_1, a_2, a_3 and a_4 are the coupling coefficients. When light is launched into WG1 at z=0, it follows:

$$\emptyset_2(0) = a_3\varphi_e + a_4\varphi_o = 0 \quad (6\text{-}2)$$

In order to ensure low radiation loss, light has to completely couple back from WG2 into WG1 at the rear facet of the PD, hence it is necessary to make $\emptyset_2(l_{pd}) = 0$. Combining with the initial conditions (eq. 6-2), the propagation constant of the odd and even modes should follow:

$$\exp[-i(\Delta\beta)l_{pd}] = 1 \quad (6\text{-}3)$$

Here $\triangle\beta$ is the difference between the even and odd mode propagation constants defined as: $\Delta\beta = \beta_e - \beta_o$. Defining $\Delta\beta_r$ and $\Delta\beta_i$ to be the real and imaginary parts of $\Delta\beta$, eq. (6-3) becomes:

$$\exp(\Delta\beta_i l_{pd}) \cdot \exp(-i\Delta\beta_r l_{pd}) = 1 \quad (6\text{-}4)$$

In order to satisfy above equation, it is imperative to make $\Delta\beta_i = 0$. This means, that the propagation constants of the odd and even modes have the same imaginary part. Or, in other words, only when even and odd modes attenuate at the same rate, a complete transfer of optical power between WG1 and WG2 is possible. Moreover, the PD length l_{pd} is concluded to be multiples of the beat length L, defined as:

$$L = 2\cdot \pi/\Delta\beta_r \quad (6\text{-}5)$$

6.3 Simulation

To calculate the field distributions and propagation constants, I used the commercial software Fimmwave. In the design process I started from the simplified structure as shown in Fig. 6-1. Since changing the thickness of the cladding layer between WG1 and WG2 will change β_o and β_e simultaneously, I kept this parameter to be 220 nm to ensure sufficient field overlap between WG1 and WG2. At the same time the thickness of WG1 should be thick enough to ensure minimal field overlap with the highly doped n-contact layer and to prevent free-carrier absorption. However, a thick WG1 layer decreases the coupling efficiency from WG1 to WG2 owing to a better mode

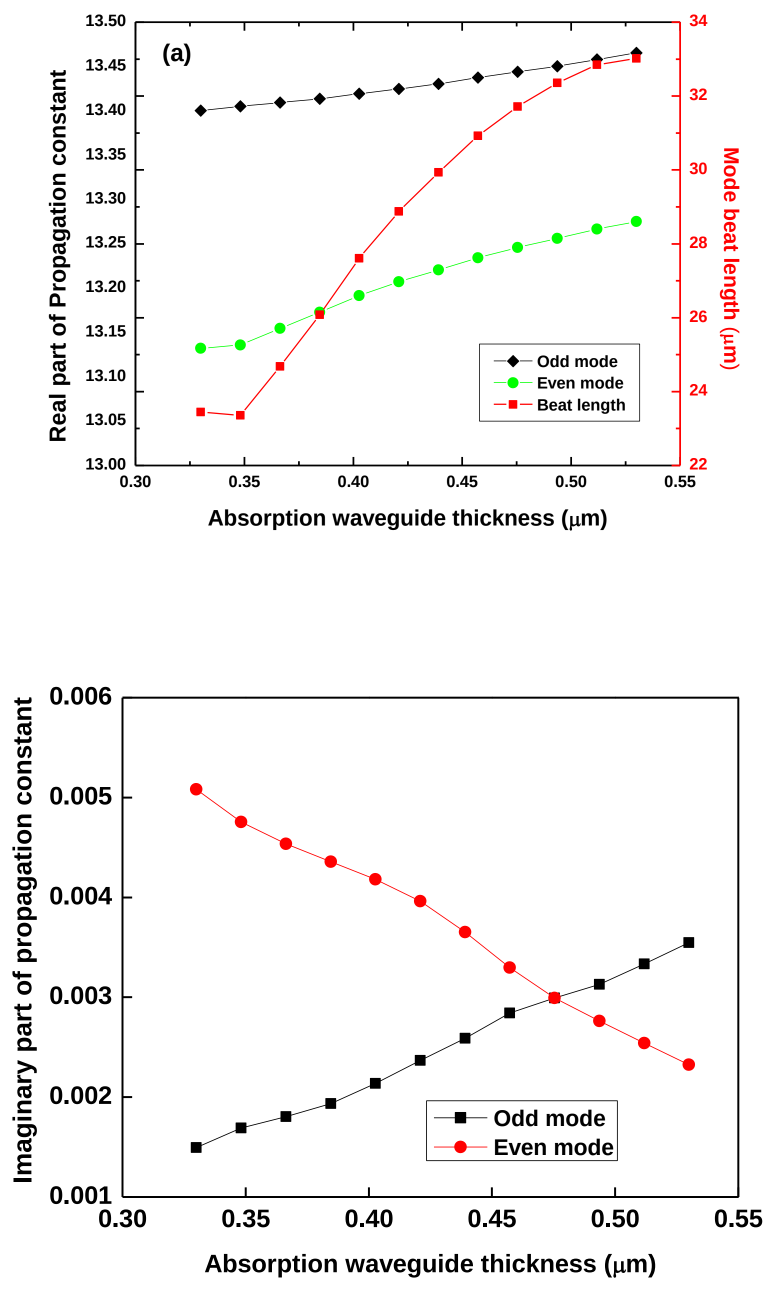

Fig. 6-3 (a) Real part of propagation constant and mode beat length vs. WG2 thickness. (b) Imaginary part of propagation constants vs. WG2 thickness.

confinement. In the design, I chose a 500 nm thick WG1 that can provide both, a low free-carrier absorption and a strong coupling. For moderate absorption in the first PD, the thickness of InGaAs in WG2 cannot be too thick. Sandwiching an only 30-nm thin InGaAs layer between the two InGaAsP layers results in a similar propagation constant of WG1 and WG2 with a low effective absorption coefficient in WG2.

After adopting two InGaAsP layers sandwiching a 30 nm InGaAs layer as WG2, the relationships between real part of the propagation constants (β_r) and thickness of WG2 are shown in Fig. 8 (a). Here, the WG2 thickness is the total thickness of the InGaAs absorption layer and the InGaAsP layers. The β_r of the odd and even mode are both linear with the thickness of WG2. Using eq. (5), the beat length determined by the difference of the even and odd modes' propagation constants is also shown in Fig. 6-3 (a). The beat lengths range from 23 μm to 33 μm when the thickness of WG2 changes from 0.3 μm to 0.55 μm. In order to ensure that light couples back from WG2 to WG1, the PD length can only be an integral multiple length of the beat length. For the 30 nm thick InGaAs layer being sandwiched by two 220 nm thick InGaAsP layers, each segmented PD element should be around 30 μm. Fig. 6-3 (b) shows the simulated imaginary part of propagation constant (β_i) of the odd and even modes. We found that β_i of the even mode increases with WG2 thickness while the odd mode behaves vice versa. When the thickness of WG2 is 470 nm, both modes exhibit the same β_i, i.e eq. (6-4) is satisfied. According to Fig. 6-3 (a), the beat length is 32 μm in this situation.

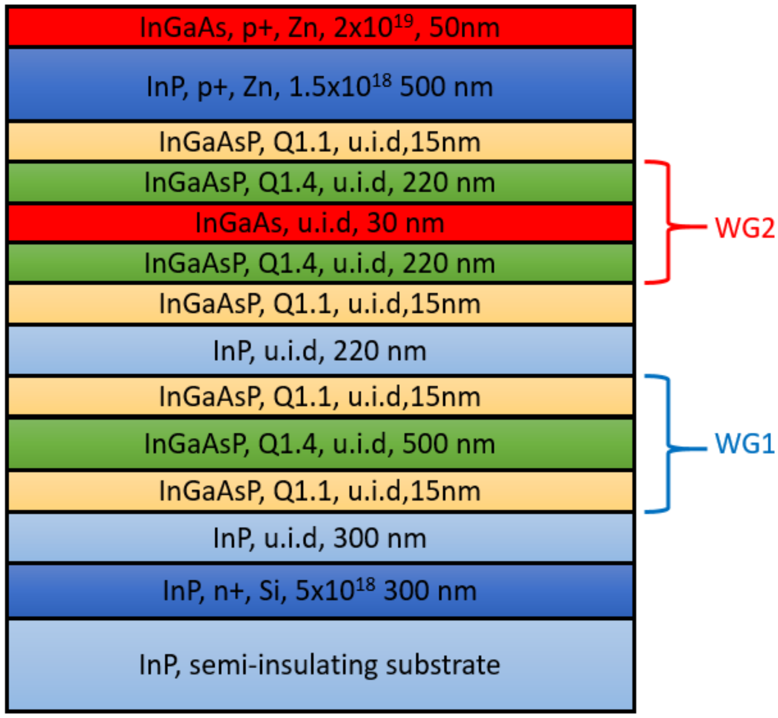

Fig. 6-4 Epitaxial layer structure for segmented waveguide photodetector.

Figure 6-4 shows the complete epitaxial layer structure of the segmented waveguide photodetector that was grown on InP substrate by metal organic chemical vapor deposition. The 300 nm thick Si-doped InP layer serves as the n-type contact layer followed by an intrinsic 300 nm thick InP layer as the lower cladding. I used a 500 nm thick intrinsic InGaAsP layer as WG1 and a 220 nm thick intrinsic InP cladding layer to separate WG1 and WG2. Two InGaAsP layers sandwich the 30 nm thick InGaAs absorption layer to form WG2. The p-type contact layer is composed of a 500 nm thick highly doped InP and a 50 nm thick top InGaAs layer. Layers of InGaAsP Q1.1 were used to reduce the band-discontinuities at the heterojunction interfaces between the InP and InGaAsP Q1.4 layers [6.10].

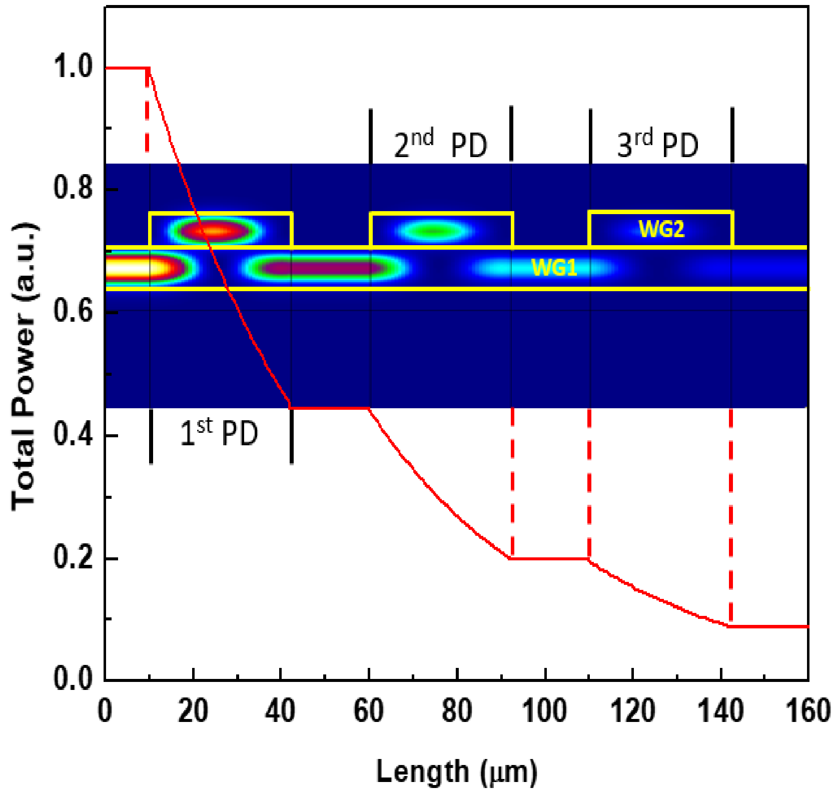

Fig. 6-5 Simulation of the total power in the segmented waveguide photodetector with 3 PDs.

Figure. 6-5 shows the simulated total power in the segmented photodetector with 3 elements. It can be seen that in each PD, the light power decays exponentially. Assuming a lossless WG1, the power remains constant in the regions between PD segments. The simulation also predicts that, the light couples completely back into WG1 at each PD's rear end.

6.4 Fabrication and characterization

A double mesa process was used to fabricate the PDs. To address the tight alignment tolerance between feeding waveguide and photodiode mesa, I developed a process that defines both features in one step. The fabrication flow is summarized in figure. 6-6. Dry etch was used here to precisely control the etching depth. After blanket deposition of the p-metal, we patterned a SiO_2 hard mask and formed a ridge structure. The first mesa etching stopped at the InP n-contact layer to define WG1. Then, the n-metal was deposited. Next, a second hard mask was used to form WG2 and the n-mesa. By this way, we achieved that WG1 and WG2 have a uniform width. AuGe/Ni/Au and Ti/Pt/Au were used for n-metal and p-metal contacts as described in chapter 2. Photodiodes were connected to gold-plated pads through air-bridges, as shown in figure 6-7. I also fabricated single PDs with coplanar waveguide RF pads to characterize the bandwidth. Finally, I cleaved the waveguide facet for input light coupling.

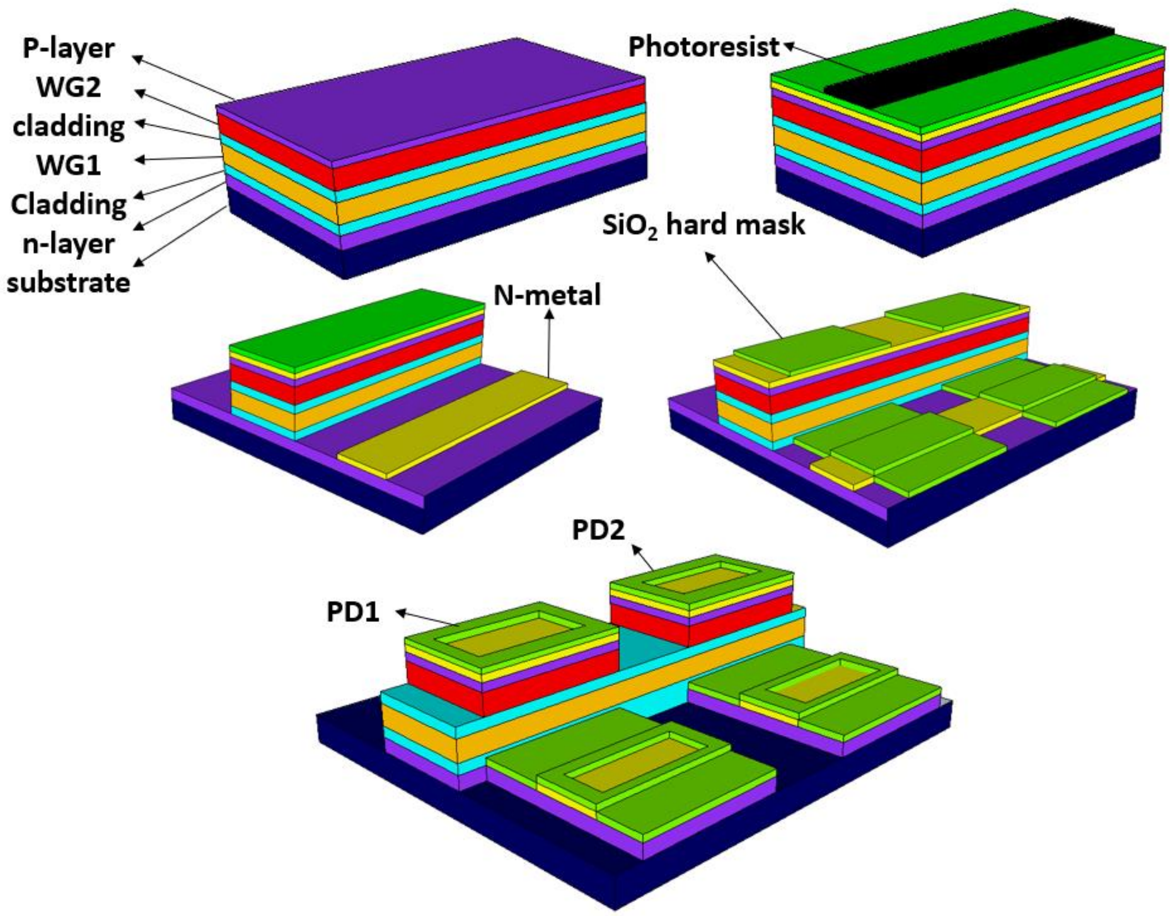

Fig. 6-6 Fabrication process to achieve uniform width for WG1 and WG2.

To account for uncertainties of the material refractive indices in the simulations arrays with photodiode's lengths ranging from 20 μm to 40 μm were fabricated. All PDs in an array were probed individually. I measured uniform I-V characteristics with dark currents of 1 μA at 3 V reverse voltage as shown in figure 6-8. I expect that the dark current can be further reduced with an appropriate side wall passivation.

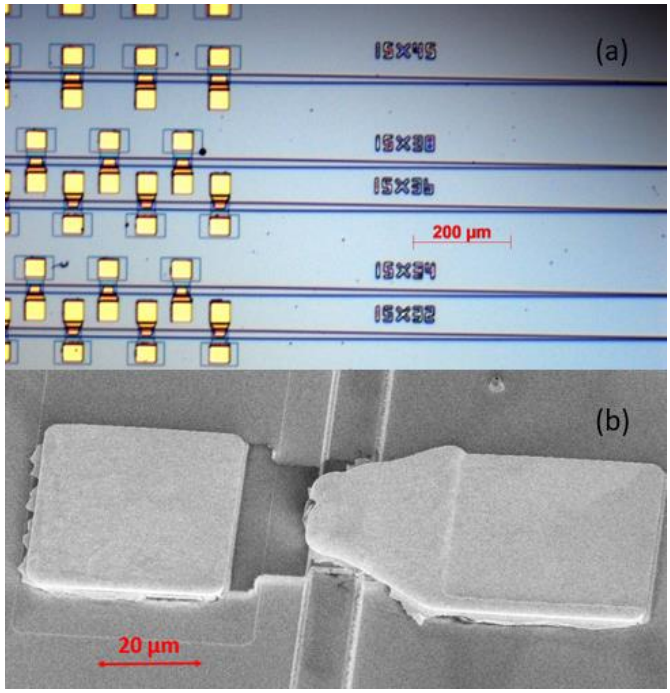

Fig. 6-7 (a) Microscope picture of fabricated segmented waveguide photodetector, (b) SEM pictures of a PD and a waveguide.

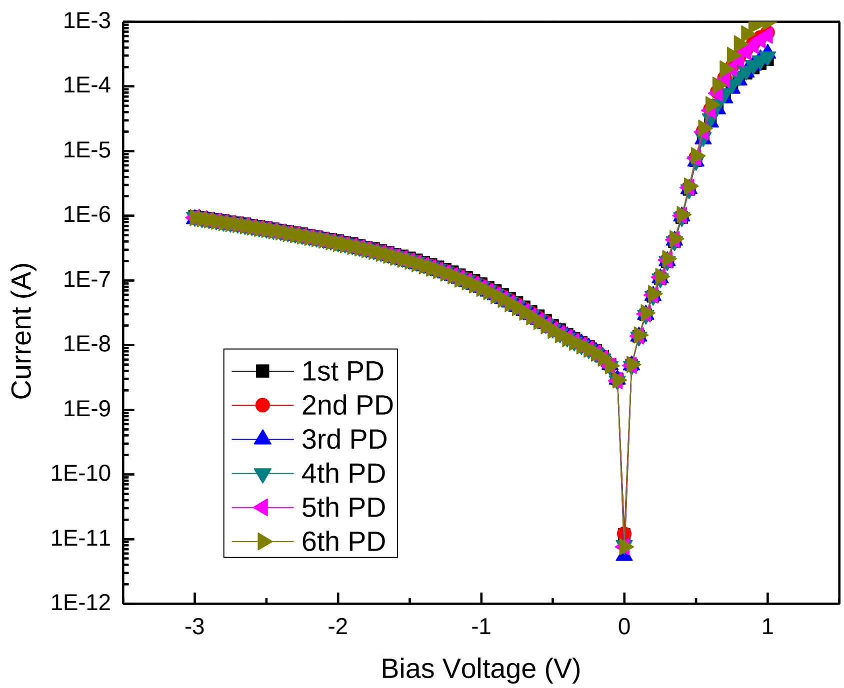

Fig. 6-8 Dark current of various sized PDs.

The frequency responses of single PDs are shown in figure. 6-9. The data was obtained under large-signal modulation by using an optical heterodyne setup at 1550 nm. It can be seen that a smaller PD area leads to higher bandwidth owing to the reduced capacitance. A photodiode with an active area of 15 x 20 μm^2 reached a bandwidth of 20 GHz.

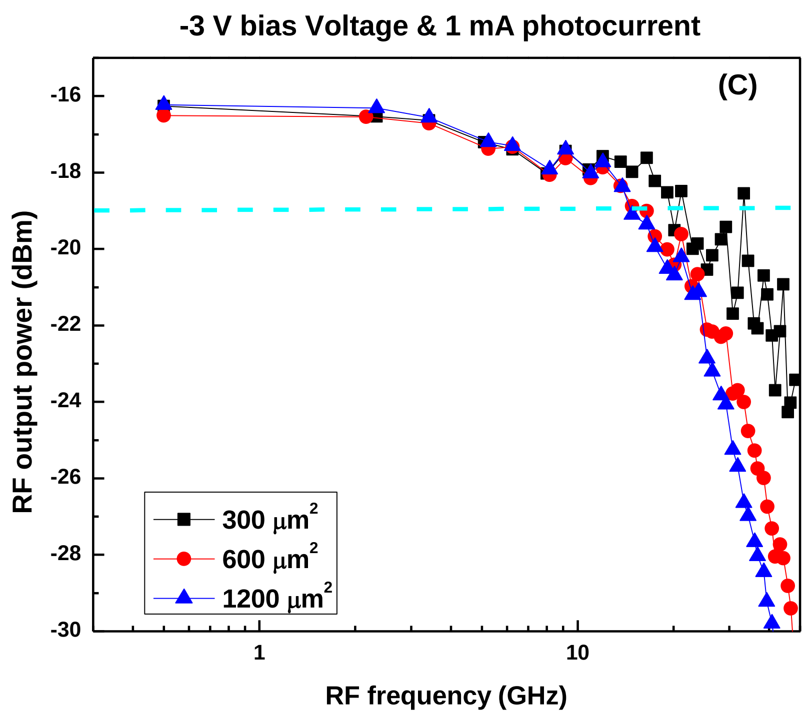

Fig. 6-9 Bandwidth measurements of single photodiodes with different areas from the same wafer.

Using a lensed fiber with 2.5 μm spot size diameter, the quantum efficiency was measured as a function of PD length in single waveguide photodiodes. At first, we measured several 300 μm long single PDs to characterize the coupling loss from the fiber to the waveguide. According to our simulation, a 300 μm long PD should have an internal QE of 99%. Based on the measured external QE of (35±2) %, the coupling loss from the fiber into the waveguide was calculated to be 4.5 dB. In the analysis, 1.5 dB loss are attributed to reflection at the facet since no anti-reflection coating was used. The remaining loss of 3 dB agrees with the simulated coupling loss due to mode mismatch from the fiber mode to the waveguide mode.

Using 4.5 dB as the coupling loss, figure. 6-10 shows the internal QE of single PDs of different length. The data shows that the QE only depends weakly on PD width. For a fixed width, longer PDs consistently show higher QE owing to the longer absorption length. As expected and due to mode beating phenomena, the QE scales in a non-linear fashion with PD length. This explains the flat region around the calculated beat length of 30 μm in figure. 6-10, which indicates that in this region the QE does not increase as light couples back into WG1.

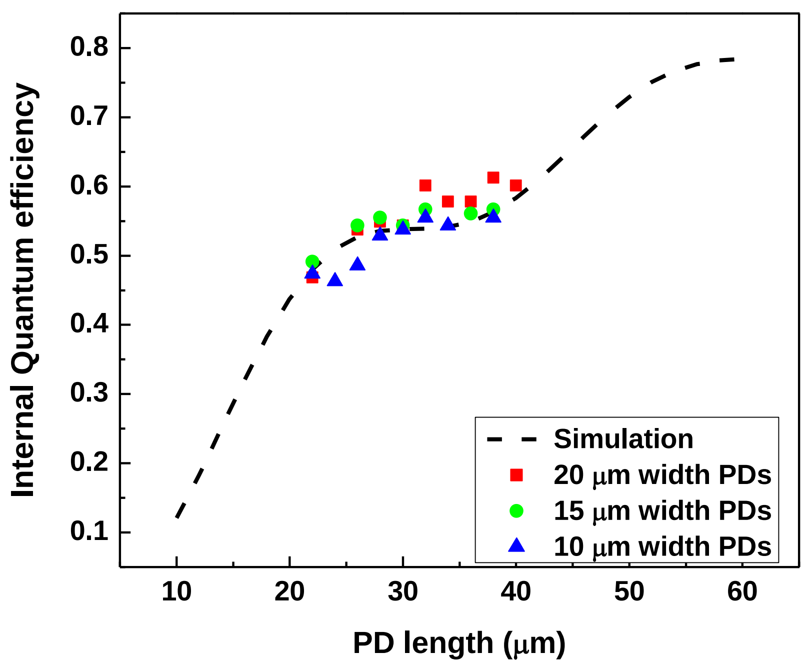

Fig. 6-10 Simulated and measured internal QE of single PDs with different widths vs. PD length.

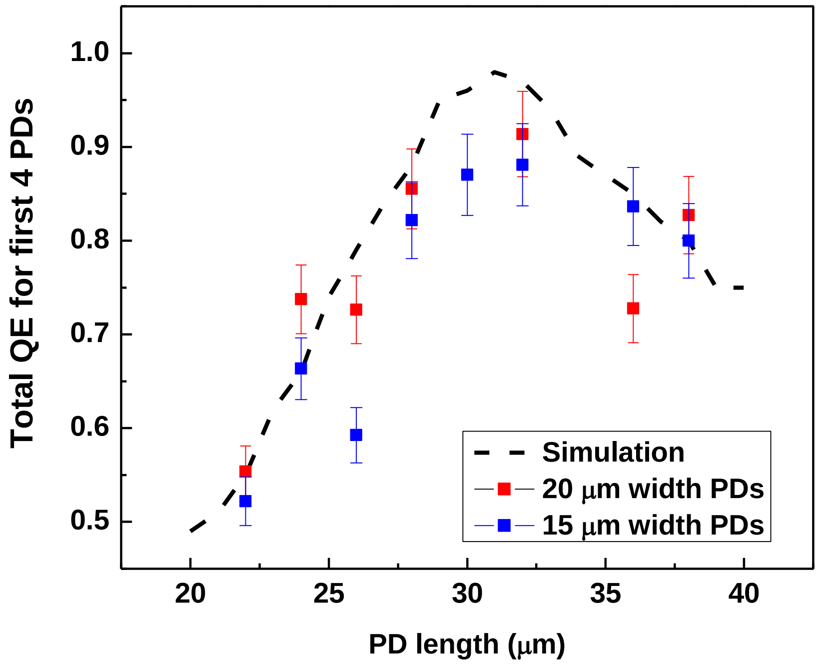

Fig. 6-11 Total internal QE of the segmented waveguide photodetector. The error bars come from the uncertainty in determining the input coupling loss.

The total QE of a 6 elements segmented waveguide photodetector is shown in figure. 6-11. To determine the IQE, I added the photocurrent of the first 4 PDs in the array that were measured simultaneously, and corrected for the 4.5 dB input coupling loss. As expected from simulation, the contributions from the 5th and the 6th PDs in the array were negligible. The results show that the total internal QE increases for PD lengths larger than are 20 μm. At 32 μm PD length, the QE reaches its peak value around 90% corresponding to 1.13 A/W. For longer PDs, the radiation loss prevails leading to a decrease in total QE. The black line in figure. 6-11 shows the total QE by simulation. It can be seen that the measurement agrees well with the simulation within the error bars. The fact that the measurement exhibits excess loss can be explained by the following reasons. First, the refractive indices that we used in the simulation may not be accurate. Together with small variations in the epitaxial layer thicknesses this may lead to a mismatch of the propagation constants of WG1 and WG2. Moreover, I did not include any waveguide loss between PD segments in the simulations.

6.5 Waveguide segmented photodetector with 50 PDs for PNR

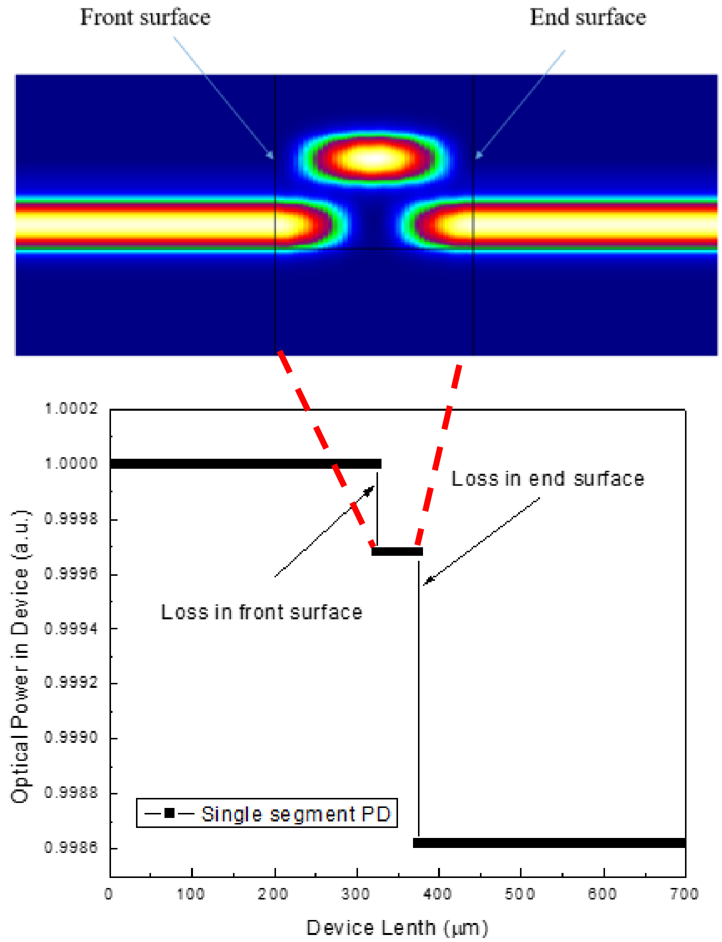

Fig.6-12 Loss analysis for one PD in the segmented detector: (a) optical intensity simulation, (b) simulated optical power during propagation

In figure 6-12, the loss analysis for one PD segment is shown. This simulated PD segment has an identical epitaxial layer stack structure as shown in the Fig. 6-4 except for changing the InGaAs layer to be InGaAsP (Q1.4). This is because a large number of photodiode elements are needed for a PNR system and therefore it is necessary to make each element only absorb small portion of the incident optical signal. When simulating the PD without absorption in the absorber, the radiation loss from the front surface (0.02%) and the end surface (0.12%) of a PD can be determined. The total loss is only 0.14% for each PD which suggests that segmented detectors with large PD count are possible. It should be mentioned that waveguide loss and metal absorption loss has not been considered in this simulation.

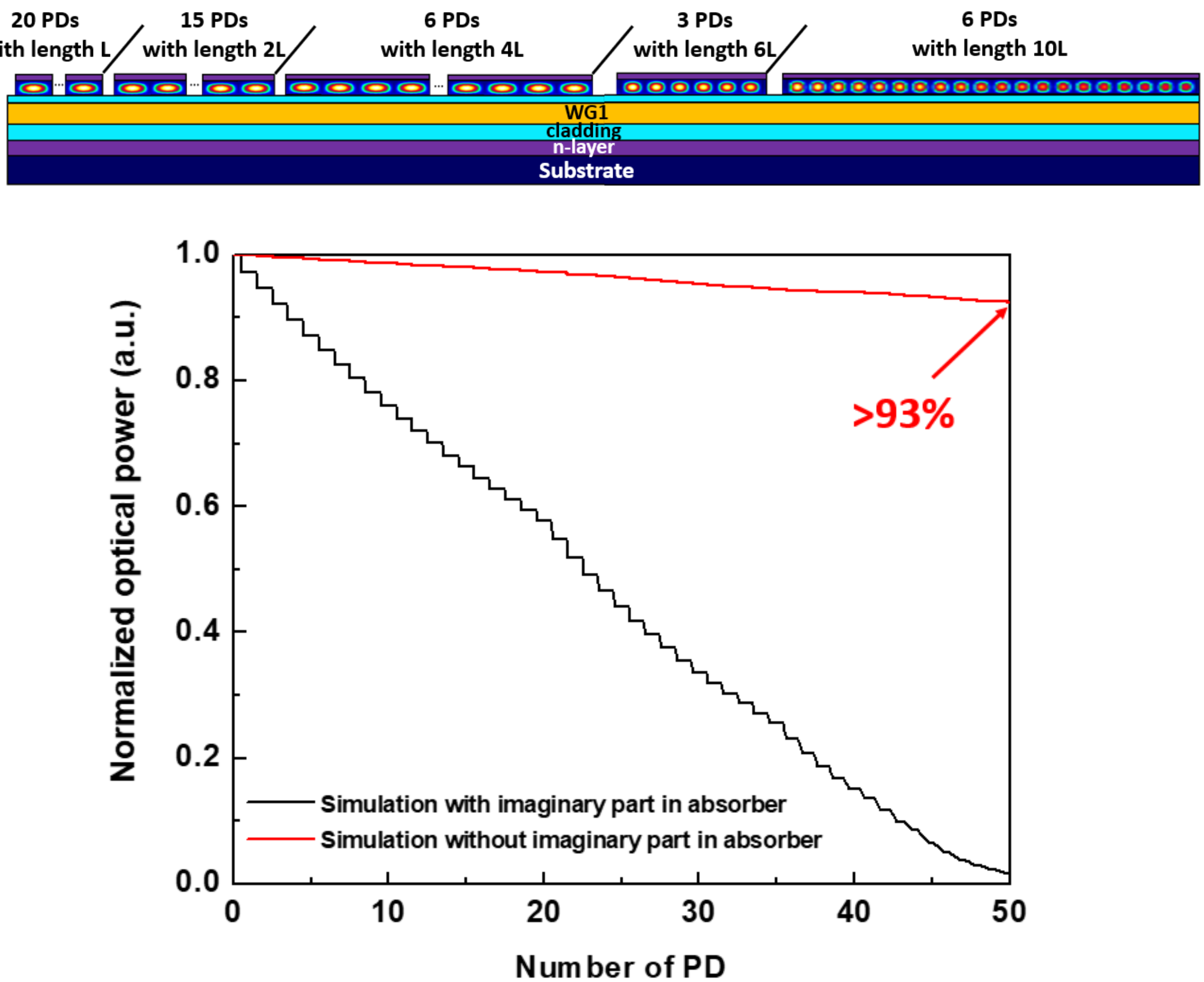

Fig.6-13 Schematic of 50 PDs with various length and simulated QE for 50 PDs.

The validity of the segmented waveguide PD was shown in the previous section for a relatively small count of discrete PDs. However, the proposed PNR system does not only need high quantum efficiency for the whole system but also much larger PD count and uniform absorption across all its elements in order to achieve high Postitive-Operator-Valued Measures (POVM) element purity [6.11]. Moreover, a small active volume is beneficial since it helps reducing the dark current, jitter, and increases the PD's count rate. In our previous design, low loss can be achieved during propagation in this segmented photodetector once the PD length is an integral multiple length of the mode beat length L. Here, 50 segmented PDs are proposed aiming for achieving high photon number resolution. There are twenty PDs with length L, fifteen 2L length PDs, six 4L length PDs, three 6L length PDs and six 10L length PDs as shown in Fig. 6-13. Different lengths of PDs are designed for achieving similar photocurrents for every PD. This is the because the optical power will decay during propagation. The lateral element needs to be longer to maintain a similar photocurrent as the previous one. I estimated the total radiation losses by simulating the photodetector without including the imaginary part in the absorber layer. From figure 6-13, 50 PDs have 7% loss in total. Here I further optimized the structure by leaving the cladding layer between WG1 and WG2 onto WG1 for less radiation loss. From figure 6-13, it also can be seen that once making device with length l_{pd} owing to 2.5% QE, light absorption will be uniform across all 50 PDs. This simulation result indicates that it is feasible to make a segmented photodetector with large number of elements and keep radiation loss low. Such a device has the potential to be used in the PNR system in ref. [6.11] to achieve high POVM element purity.

6.6 AlInAsSb APD wafer design for PNR waveguide segmented detector

A single photon avalanche photodiode is an avalanche photodiode working in the Geiger mode region as shown in Fig.6-14. In Geiger mode, the output electrical signal no longer varies with the light intensity in a linear fashion. Instead, even a single photon-generated carrier will generate considerable photocurrent by avalanche effect, which can be used for single photon detection [6.12-6.13]. In the photon number resolution system, the photodetector is required to detect photon level signals. Therefore, single-photon avalanche diodes (SPAD) are needed here.

Here I start by replacing the PIN photodiodes in the segmented waveguide photodetector with APDs and verifying whether the optical coupling mechanism still works. For the APD, the digital alloy system AlInAsSb has been proven to be a low noise material and thus provides great potential for such a system [6.14]. Figure 6-15 shows the epitaxial layer design for a separate absorption, charge and multiplication (SACM) APD. The design will be analyzed in two parts: optical and electrical.

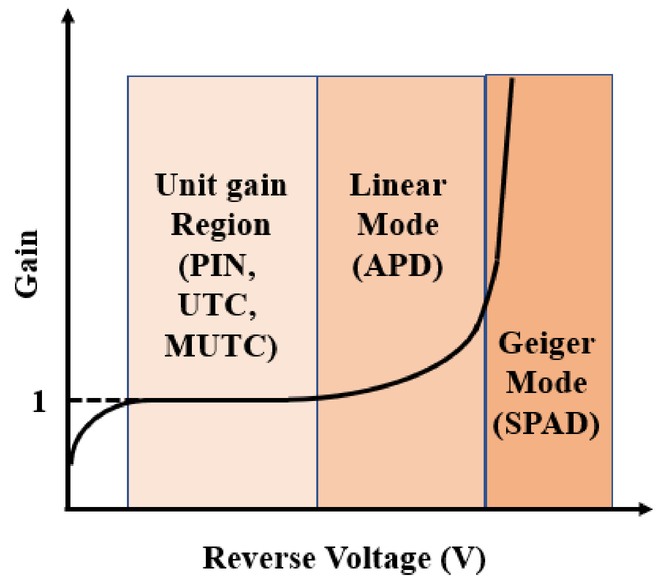

Fig.6-14 Gain versus reverse voltage curve for PDs.

In the optical design, I first reduced absorption in each element. To this end, the absorption WG consists of 6 nm $Al_{0.45}InAsSb$ sandwiched by two 191 nm $Al_{0.7}InAsSb$ layers. The absorption layer is a 6 nm-thick layer of $Al_{0.45}InAsSb$ which makes each PD element only contributing a small fraction (2.5 %) of the overall total photocurrent. The passive WG is a 750 nm-thick $Al_{0.7}InAsSb$ layer. These two waveguides are separated by a 120 nm-thick AlAsSb layer, which can be used to control the beat length L. In order to smooth the band discontinuity between $Al_{0.45}InAsSb$ and

$Al_{0.7}InAsSb$, AlInAsSb with different Al concentrations (50% and 60%) are also added in the design. The simulated loss per element is 0.3%.

In the electrical part, the 120 nm-thick AlAsSb layer that separates the two waveguides also serves as the charge layer. The charge layer is used to control the electrical field distribution in absorption region and multiplication region. The goal is to have an avalanche effect only in the multiplication layer and not in the absorption layer. In figure 6-17, the band diagrams are shown under 0 V and 40 V. The multiplication layer is chosen to be $Al_{0.7}InAsSb$ as it has been proven to provide a low k value (k = 0.01) [6.12].

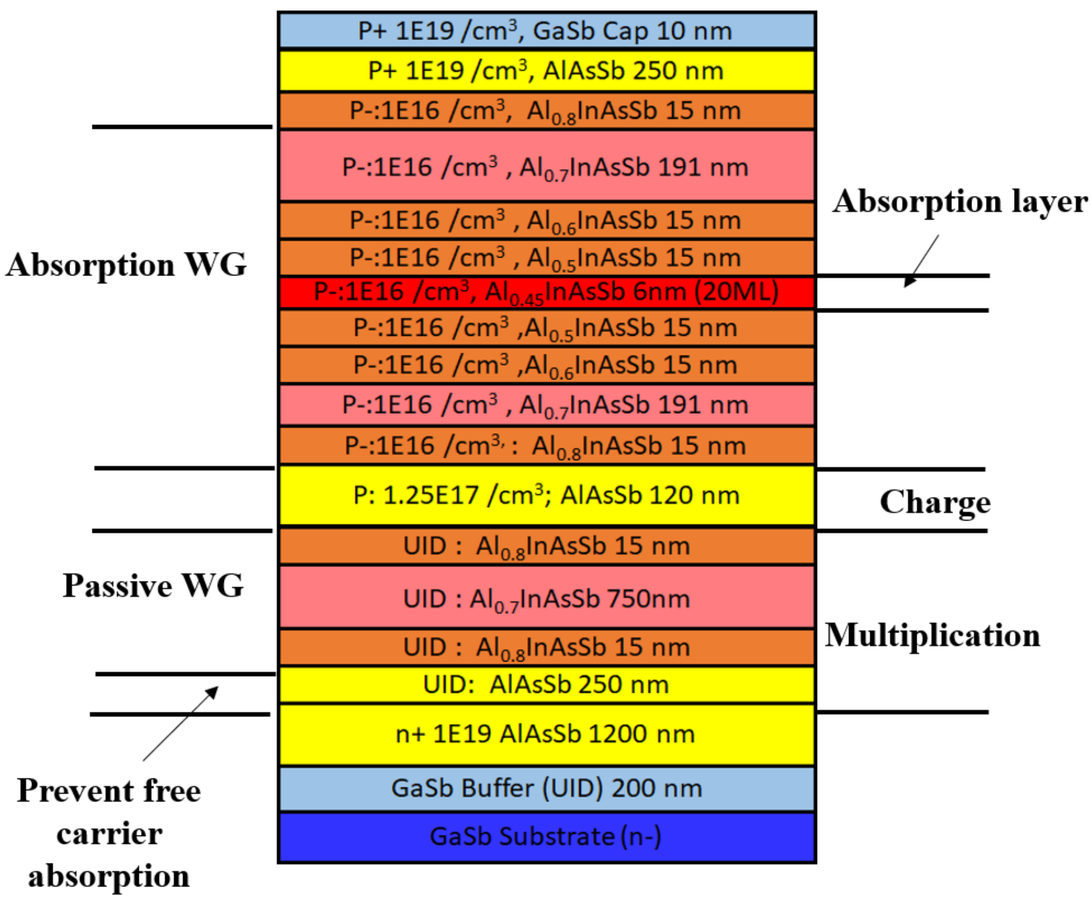

Fig.6-15 Epitaxial layer design for segmented waveguide AlInAsSb APD.

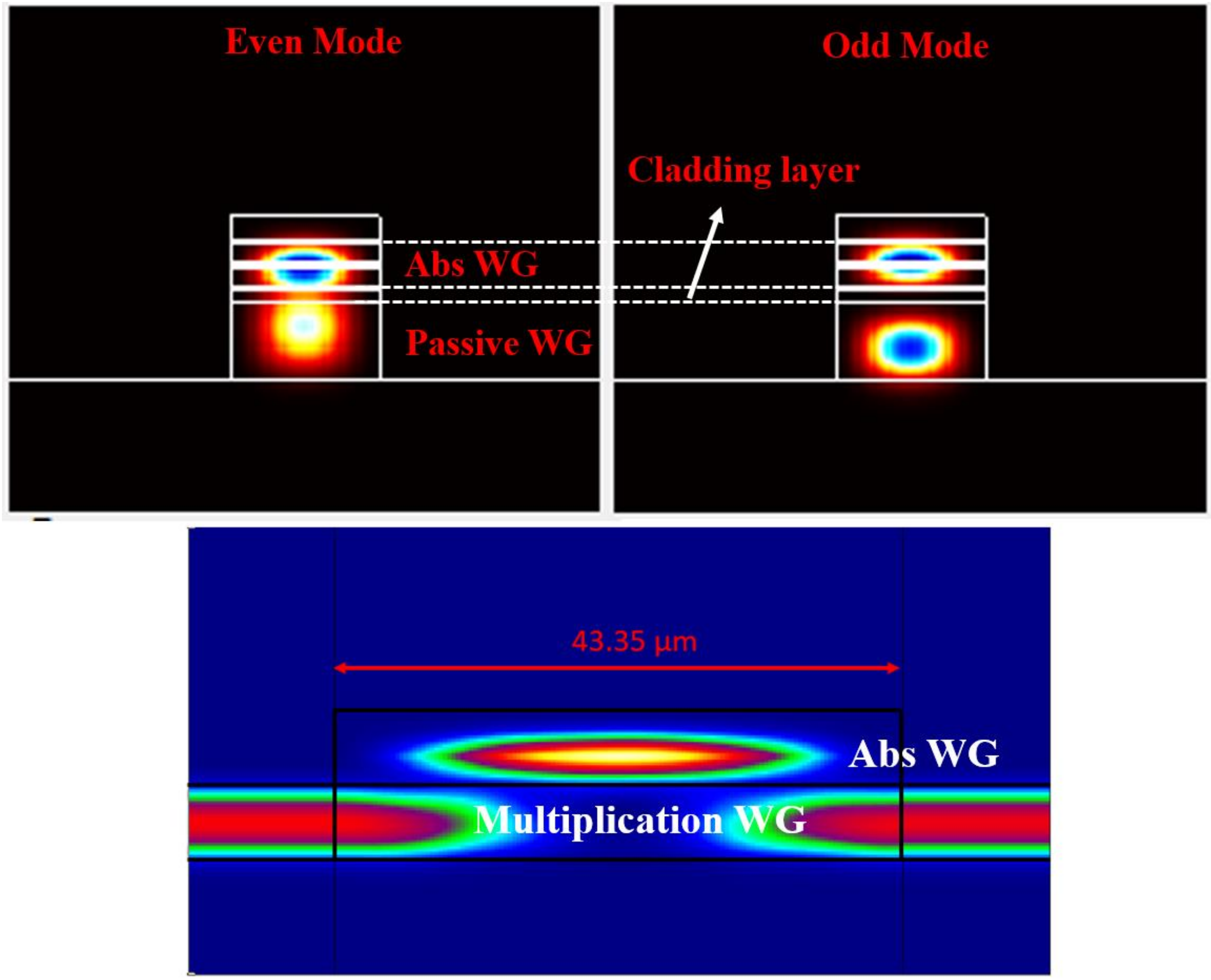

Fig.6-16 Even and odd modes in the AlInAsSb APD design and optical simulation of single element.

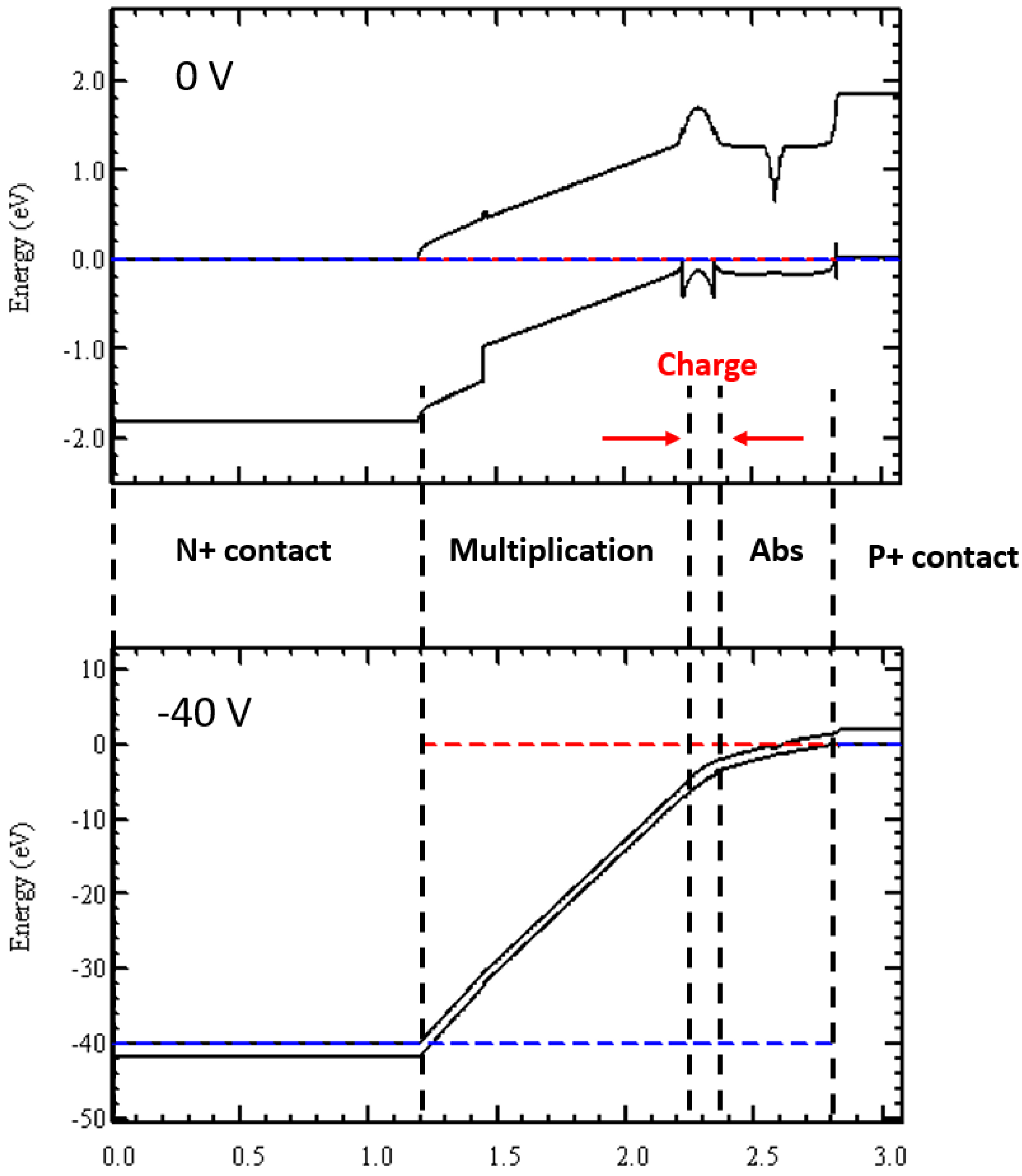

Fig.6-16 Band diagrams for the epitaxial design in figure 6-3 under 0 V and 40 V reverse voltages.

6.7 Summary

A novel segmented waveguide photodetector based on a directional coupler design has been demonstrated. By matching the imaginary parts of the propagation constants of the even and odd modes in the design, a 6-element photodiode array achieves an internal responsivity as high as 1.13 A/W in agreement with simulations. This design finds applications in traveling wave PDs and in recently proposed photon number resolving detectors that benefit from near-unity quantum efficiency and minimized active volumes. The design was optimized for a 50-element array and a waveguide SACM APD is also designed to enable single photon detection in photon number resolving systems.

References

[6.1] D. Wake, T. P. Spooner, S. D. Perrin, and I. D. Henning, "50 GHz InGaAs edge-coupled PIN photodetector," Electronics letters, 27(12), 1073-1075 (1991).

[6.2] Y. Wang, Z. Wang, Q. Yu, X. Xie, T. Posavitz, M. Jacob-Mitos, A. Ramaswamy, J. N. Erik, A. F. Gregory, A. Beling "High-Power Photodiodes With 65 GHz Bandwidth Heterogeneously Integrated Onto Silicon-on-Insulator Nano-Waveguides." IEEE Journal of Selected Topics in Quantum Electronics 24(2): 1-6 (2017)

[6.3] M. S. Islam, T. Jung, T. Itoh, M. Wu, D. L. Sivco, and Y. Cho, "Velocity-matched distributed photodetectors with pin photodiodes," in Microwave Photonics, pp. 217-220 (2000).

[6.4] R. Nehra, C. H. Chang, A. Beling, and O. Pfister , University of Virginia, are preparing a manuscript to be called "Photon-number-resolving segmented avalanche-photodiode detectors."

[6.5] F. J. Effenberger, and A. M. Joshi, "Ultrafast, dual-depletion region, InGaAs/InP pin detector," Journal of Lightwave Technology, 14(8): 1859-1864 (1996).

[6.6] Q. Li, K. Sun, K. Li, Q. Yu, P. Runge, W. Ebert, A. Beling, and J. C. Campbell, “High-Power Evanescently-coupled Waveguide MUTC Photodiode with >105 GHz bandwidth,” Journal of Lightwave Technology, 35(21), 4752-4757 (2017).

[6.7] A. Yarov, "Coupled-mode theory for guided-wave optics." IEEE Journal of Quantum Electronics 9(9): 919-933 (1973).

[6.8] V. R. Chinni, T. C. Huang, P. K. Wai, C. R. Menyuk, and G. J. Simonis, "Crosstalk in a lossy directional coupler switch," Journal of Lightwave Technology 13(7): 1530-1535 (1995).

[6.9] M. Dietrich, “Theory of the Directional Coupler,” in Theory of Dielectric Optical Waveguides (1991).

[6.10] Z. Li, H. Pan, H. Chen, A. Beling, and J.C. Campbell, "High-saturation-current modified uni-traveling-carrier photodiode with cliff layer," IEEE Journal of Quantum Electronics, 46(5): 626-632 (2010).

[6.11] R. Nehra, C. Chang, Q. Yu, A. Beling, and O. Pfister. "Photon-number-resolving segmented detectors based on single-photon avalanche-photodiodes." Optics Express 28, no. 3 (2020): 3660-3675.

[6.12] Cova, Sergio, M. Ghioni, A. Lacaita, Carlo Samori, and Franco Zappa. "Avalanche photodiodes and quenching circuits for single-photon detection." Applied optics 35, no. 12 (1996): 1956-1976.

[6.13] P. A. Hiskett, G. S. Buller, A. Y. Loudon, J. M. Smith, I. Gontijo, A. C. Walker, P. D. Townsend, and M. J. Robertson. "Performance and design of InGaAs/InP photodiodes for single-photon counting at 1.55 µm." Applied Optics 39, no. 36 (2000): 6818-6829.

[6.14] R. Min, S. J. Maddox, M. E. Woodson, Y. Chen, S. R. Bank, and J. C. Campbell. "Characteristics of $Al_xIn_{1-x}As_ySb_{1-y}$ (x: 0.3− 0.7) Avalanche Photodiodes." Journal of Lightwave Technology 35, no. 12 (2017): 2380-2384.

Chapter 7. Zero-bias surface normal 40 GHz PD

7.1. Introduction

In this chapter, I will introduce a type-II MUTC PD structure for zero-bias application. In order to achieve large bandwidth and high RF output power, conventional PDs usually necessitate a bias circuitry and are driven under a high external reverse voltage. Together with large photocurrents, this can lead to device heating and eventually thermal failure. To reduce thermal stress on the PD and to minimize system complexity and power consumption, zero-bias operation of the PD is desired. Having no bias circuit also helps to reduce the electrical cross-talk [7.1]. Previously, Umezawa et al. have reported a bias free InGaAs/InP uni-traveling carrier PD (UTC-PD) with an output power of -7 dBm at 100 GHz [7.1]. Jin-Wei Shi et al. have reported a GaAsSb/InP UTC-PD with - 13.9 dBm at 160 GHz in ref. [7.2]. In this chapter, a zero-bias GaAsSb/InP PD with 40 GHz bandwidth and high saturation power -2.8 dBm is presented.

7.2 Device design

To achieve high output power and large bandwidth at zero bias Ze Wang, a previous PHD student in our group, designed the epitaxial layer structure shown in Fig. 7-1. The design is done by choosing the type-II heterojunction material and optimizing the doping concentration to achieve high electrical fields in the device under zero bias while maintaining a small capacitance. The wafer was purchased from Intelliepi. In contrast to the high-power InGaAs/InP MUTC PD in ref. [7.2], here we used GaAsSb instead of InGaAs as the absorber material. This eliminates the discontinuity in the conduction band between the absorber and the InP drift layer which is known to impede electron transport across the interface at high photocurrent levels [7.3]. The epitaxial structure was grown on InP and consists of a 300 nm-thick lightly graded doped InP drift layer for space-charge compensation and a 250 nm-thick graded doped GaAsSb absorber. The simulated band diagrams at different photocurrents are shown in Fig. 7-2. In order to provide high bandwidth and high saturation power under zero-bias, the doping concentrations were carefully designed to achieve electron velocity over-shoot in the drift layer. The PDs were fabricated as double-mesa photodiodes by using conventional dry etching techniques. The PDs were connected to gold-plated coplanar waveguide (CPW) RF pads through an air-bridge.

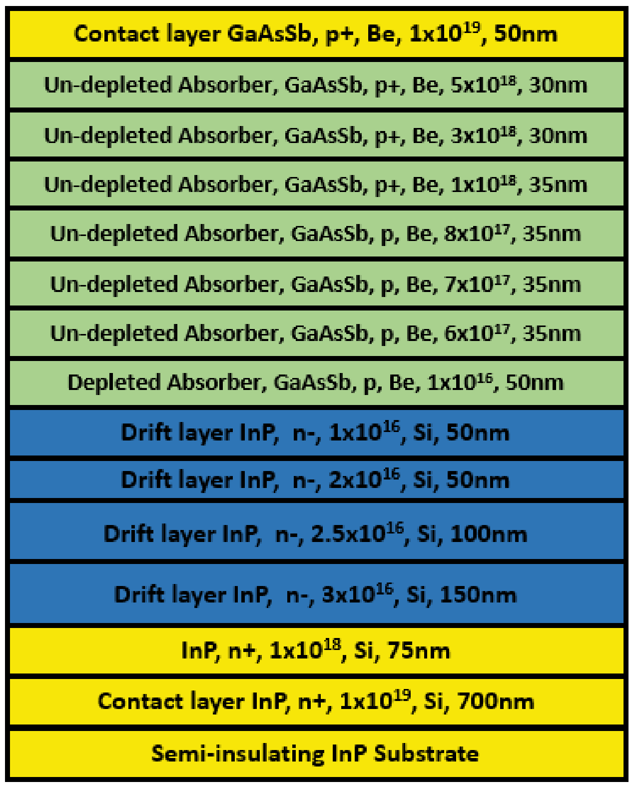

Fig. 7-1. Epitaxial structure of the PD. All layers are lattice-matched to InP.

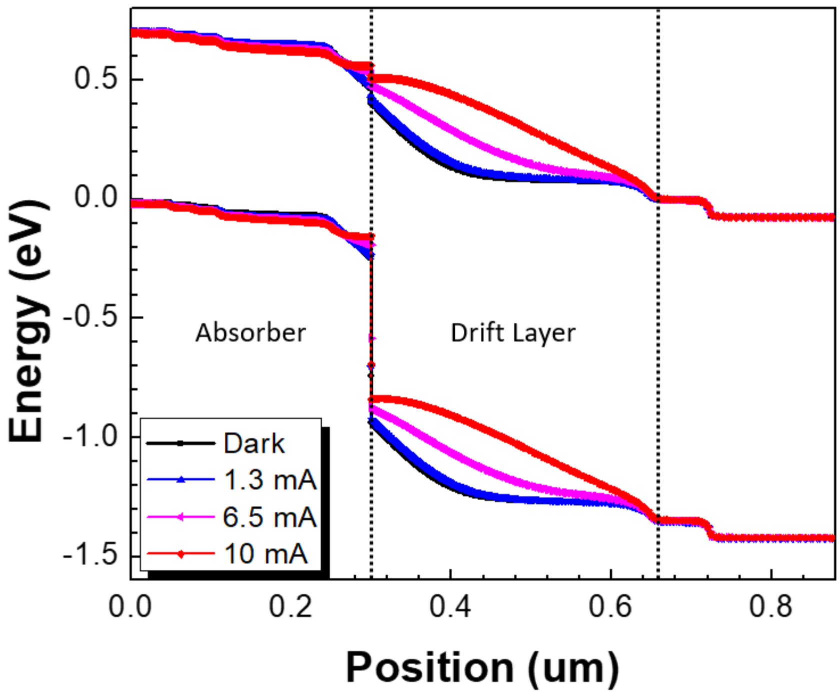

Fig. 7-2. Simulated band diagram at 0 V at different photocurrents.

7.3 Device fabrication

The PD fabrication process flow is shown in Fig. 7-3. The fabrication starts with the P-contact metal deposition with a metal stack layer of Ti/Pt/Au/Ti on the heavily-doped GaAsSb top layer by electron-beam evaporation. Then, a SiO_2 layer was deposited by (PECVD) which is used as a hard mask. With photolithography techniques, the P-mesa was formed by dry etching by ICP etch. In a similar way, the N-mesa was formed by SiO_2 deposition, photolithography and ICP etching. After the double mesas were fabricated, an air-bridge was used to connect the PD mesa to the coplanar waveguide (CPW) as shown in Fig. 7-4.

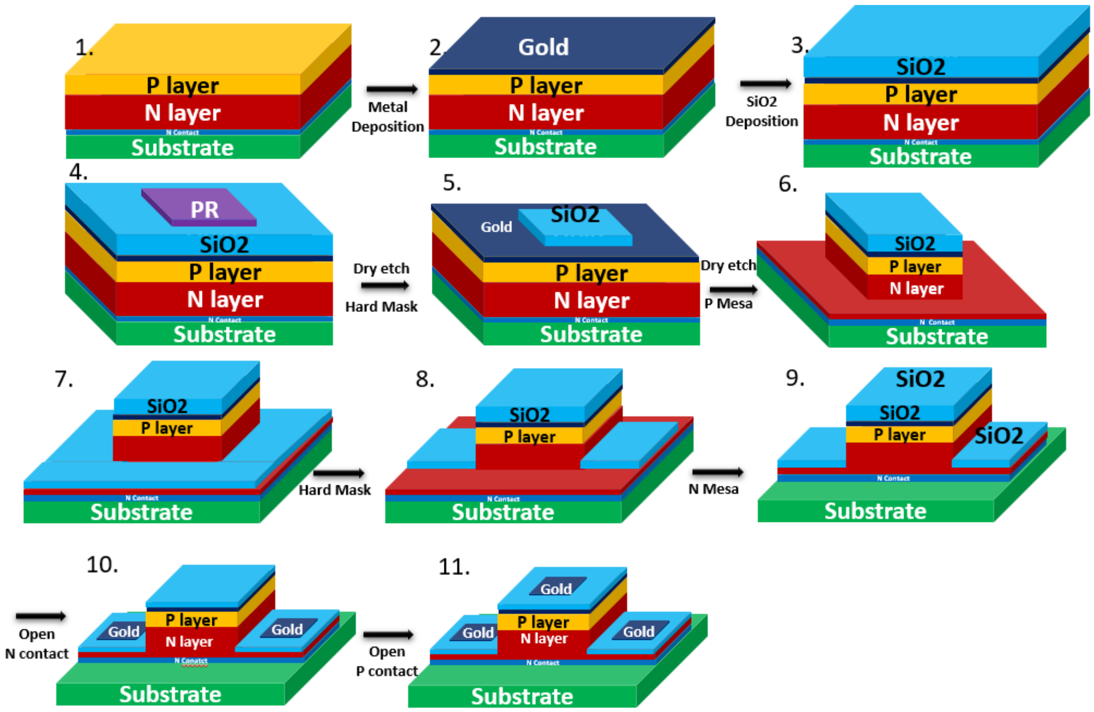

Fig. 7-3. Schematic view of fabrication flow of a double mesa PD.

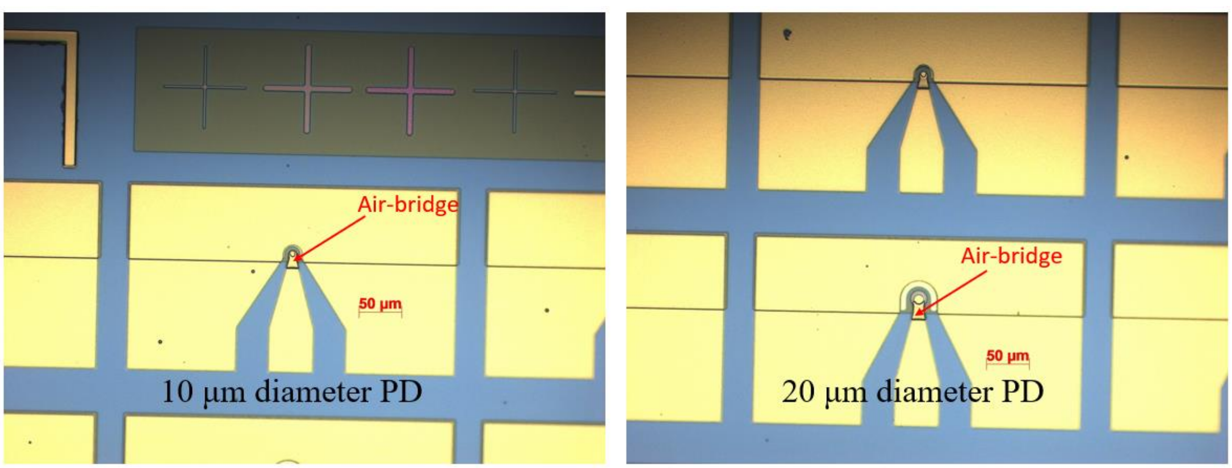

Fig. 7-4. Microscope pictures of 10 µm and 20 µm diameter PDs.

7.4 Device Characterization

The dark currents of fabricated PDs with different diameters are shown in Fig. 7-5. The dark current of a 10 µm diameter device is 20 nA at -3 V. It can be found from Fig. 7-5 that the dark current is scale with photodiode mesa. In order to study the dominant source for the dark current, the dark current versus PD diameter at -3 V is shown in Fig. 7-6.

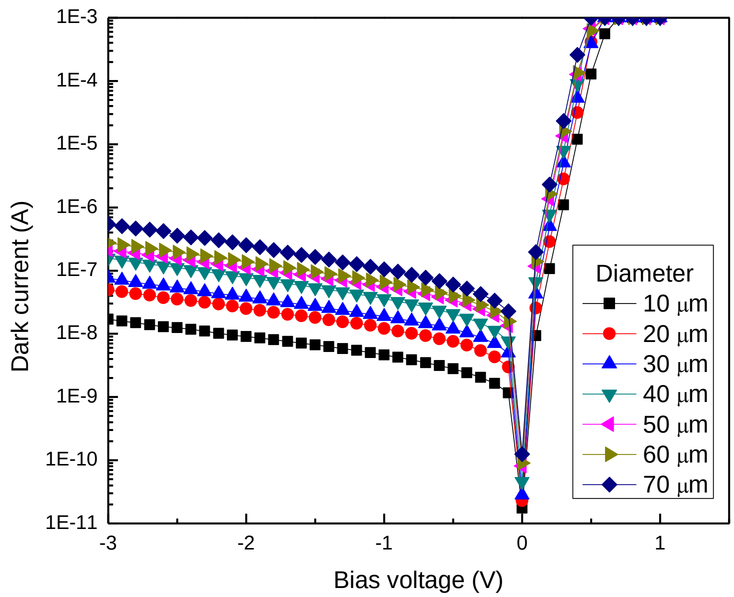

Fig. 7-5. Measured dark current versus voltage for PDs with different diameters.

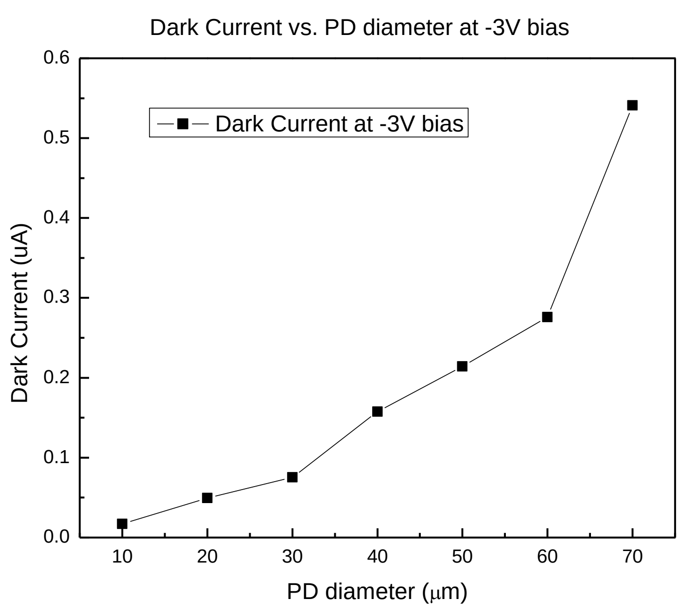

Fig. 7-6. Measured dark current versus voltage for PDs with different diameters at -3V.

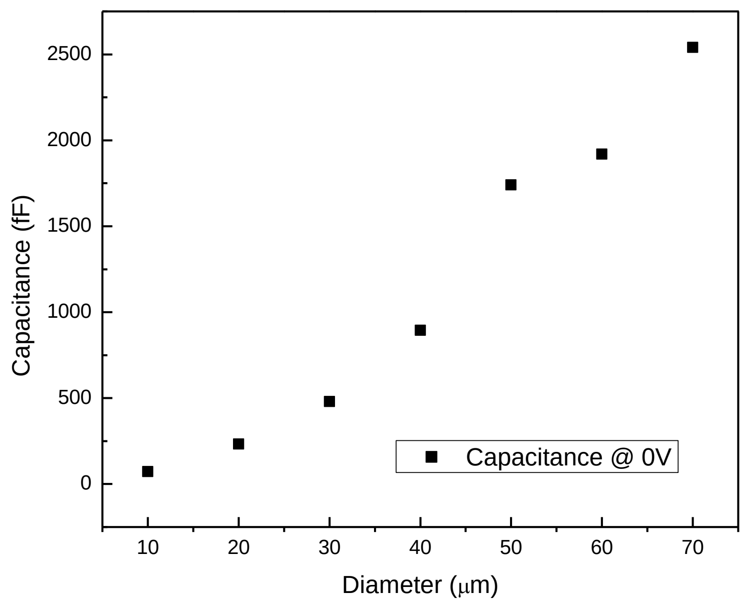

Fig. 7-7. Measured PD capacitance versus different diameters at 0 V.

Various diameter PDs' capacitance at 0 V were also characterized as shown in Fig. 7-7. Since the PD's capacitance mainly comes from the PD junction, it can be seen that the capacitance has a quadratic relationship with the PD's diameter. A capacitance of 72 fF was measured from a 10 μm diameter PD, which is much larger than expected 32 fF. This may can be explained by the doping concentration variance in real wafer as shown in Appendix IV.

The responsivity was measured to be 0.2 A/W at 1550 nm wavelength at 0 V. It can be expected that a responsivity of 0.27 A/W can be achieved once a single-layer anti-reflection coating is applied.

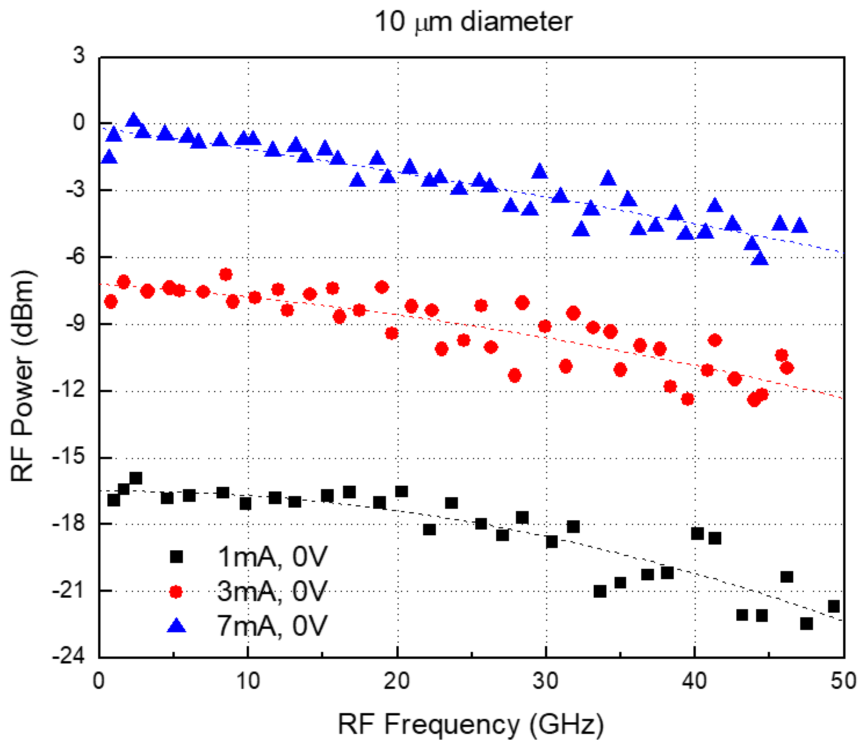

Fig. 7-8. Measured frequency responses of 10 μm diameter PD at zero bias.

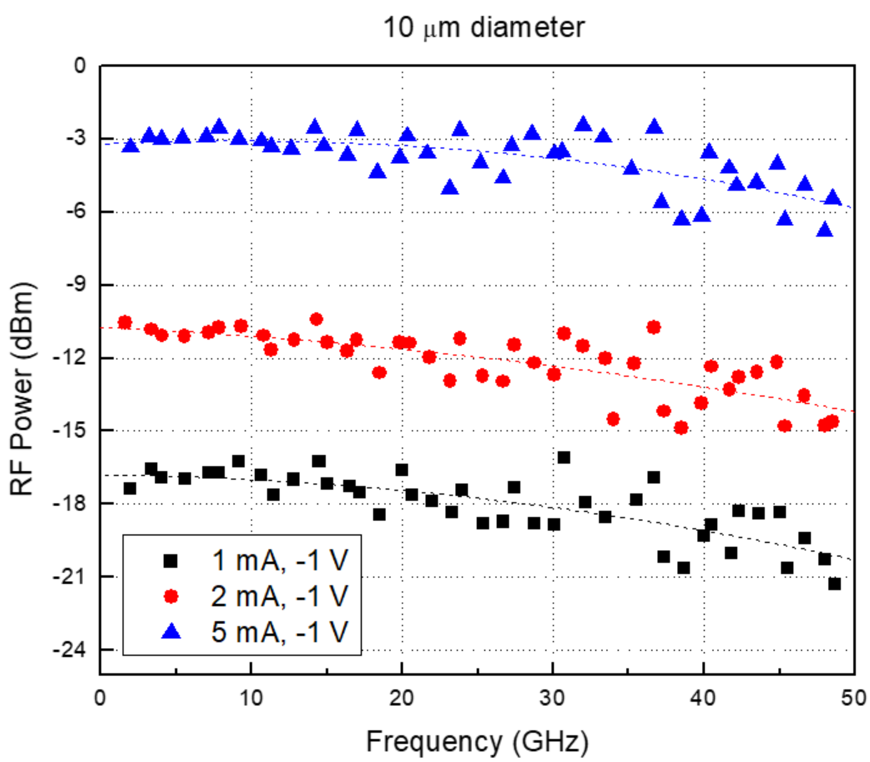

Fig. 7-9. Measured frequency responses of 10 μm diameter PD at -1 V bias voltage.

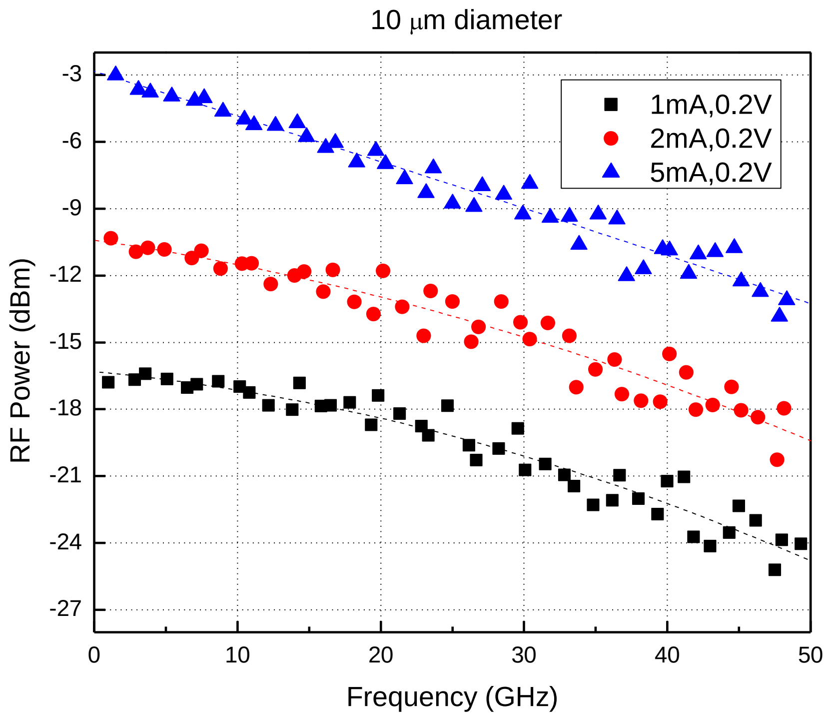

Fig. 7-10. Measured frequency responses of 10 μm diameter PD at 0.2 V bias voltage.

Figures 7-8, 7-9 and 7-10 show the measured frequency responses for different photocurrents at 0 V, -1 V and 0.2 V bias, respectively. At 0 V bias, the bandwidth is 40 GHz up to 2 mA, and 35 GHz at 5 mA. The decrease of bandwidth with higher photocurrent can be explained by the space charge effect. At -1 V bias, the bandwidth remains over 50 GHz for all measured photocurrents. The capacitance of a 10 μm diameter PD measured at 0 and -1 V bias is 72 fF and 55 fF, respectively, corresponding to an RC-limited bandwidth of 44 GHz and 57 GHz assuming a 50 Ω load. The fact that the bandwidth is limited by RC implies that a higher bandwidth can be expected by reducing the PD area. At 0.2 V forward bias, the bandwidth decreased to 25 GHz, 20 GHz, 15 GHz with 1 mA, 2 mA and 5 mA photocurrents. This can be explained by the space charge effect and the capacitance variance based on different photocurrent. I also characterized photodiode performance with 0.2 V forward bias here as shown in Fig. 7-10.

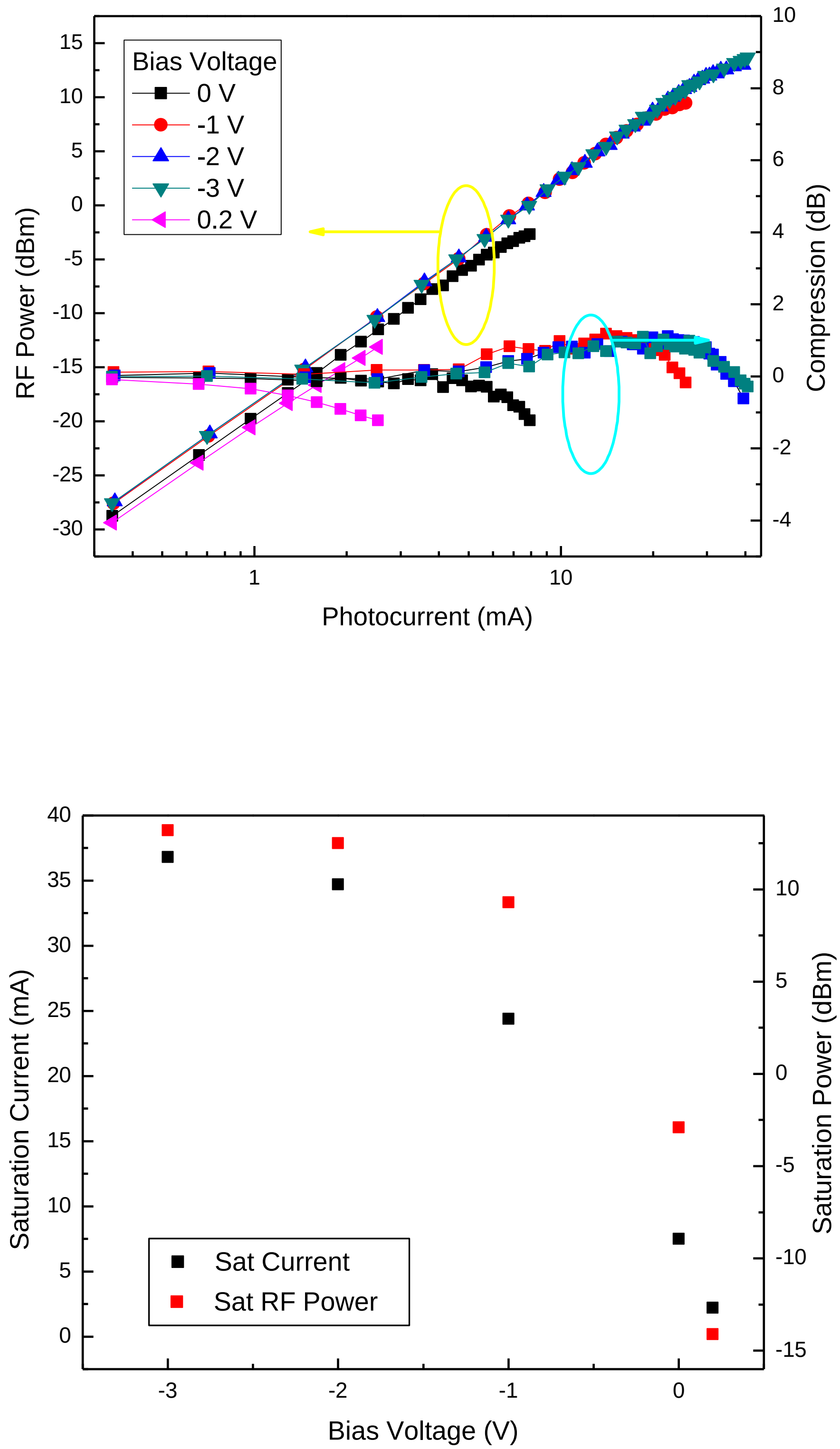

Fig. 7-11. RF output power and RF compression at different bias voltages.

Figure7-11 shows the saturation characteristics of a 10 μm diameter PD measured at 40 GHz at different voltages. I measured an RF output power of -2.8 dBm, 9.3 dBm, 12.5 dBm and 13.2 dBm at 0 V, -1 V, -2 V and -3 V, respectively. At a forward bias of 0.2 V, I obtained -14.1 dBm at 40 GHz. The saturation current of the PD is 7.5 mA under zero bias. The results indicate that the output power is mainly limited by the space charge effect in the depletion region.

7.5 Summary

By optimizing the doping concentration in a GaAsSb/InP modified uni-traveling carrier PD we demonstrated a 10 μm diameter PD with 40 GHz bandwidth, 7.5 mA saturation current and -2.8 dBm RF output power at zero-bias. The performance at other bias voltages is summarized in Table 7-1. These are the highest saturation powers that have been reported in this frequency range.

	0V	-1V	0.2V
Bandwidth (GHz)	40	>50	25
Saturation Power (dBm)	-2.8	9.3	-14.1

Table 7-1. Summary of bandwidth and saturation power at 0 V, -1 V and 0.2 V

References

[7.1] T. Umezawa, K. Akahane, N. Yamamoto, A. Kanno and T. Kawanishi. “Bias free operational UTC-PD above 110 GHz and its application to high baud rate fixed-fiber communication and W-band photonic wireless communication”, Journal of Lightwave Technology, 2016, 34(13): 3138-3147, 2016.

[7.2] J. Shi, J. Wun and Y. Zeng, "GaAs 0.5 Sb 0.5/InP UTC-PD with graded-bandgap collector for zero-bias operation at sub-THz regime." Optical Fiber Communication Conference. Optical Society of America, 2016

[7.3] Z. Li, H. Pan, H. Chen, A. Beling and J. C. Campbell, "High-saturation-current modified uni-traveling-carrier photodiode with cliff layer." IEEE Journal of Quantum Electronics, 46(5), 626-632, 2010.

Chapter 8. Summary and future work

8.1 Summary

Photodetectors have applications in many fields. Depending on their applications, photodetectors are designed to meet different performance requirements. This dissertation focuses on photodiodes designed for three kinds of photonic platforms: photonic integrated circuits based on silicon nitride, high QE and PNR detectors, and microwave photonics. To this end I developed heterogeneously integrated photodiodes on silicon nitride waveguides, segmented waveguide photodetectors, and bias-free modified uni-traveling carrier photodiodes.

For heterogeneous integration, my work mainly focuses on the development of a wafer bonding process and the demonstration of high-efficiency photodiodes on silicon nitride waveguides. Due to the lack of active optical components on silicon nitride, heterogeneous integration is the preferred choice to transfer high-performance III-V photodiodes onto silicon nitride. Among the challenges of this approach is the thick top waveguide cladding layer which can prevent efficient optical coupling into the PD. This issue was addressed by introducing a bonding window. In order to accomplish high-performance photodiodes on silicon nitride, the first step is to verify the feasibility of the bonding and fabrication processes using SU-8 wafer bonding. I demonstrated a MUTC photodiode bonded on silicon to verify the technique in chapter 3. Then, I investigated the requirements regarding the SU-8 thickness to enable high-efficiency heterogenous waveguide PDs based on simulations. After several trials, a stable SU-8 bonding process was developed yielding SU-8 thicknesses below 100 nm, which is sufficient for high-efficiency optical coupling as shown in chapter 4. Finally, I adopted the process to MUTC PDs and demonstrated record-high responsivity and high bandwidth photodiodes integrated on silicon nitride chips in chapter 5. These devices represent as key components in silicon nitride integrated photonics and it is planned to use them in a chip-scale frequency synthesizer demonstrator in collaboration with UCSB.

To achieve optical detection with photon-number resolution, I proposed a novel segmented waveguide photodetector. A proof-of-concept is presented in this dissertation, and the work shows the effectiveness of the new segmented photodetector design. The design utilizes an optical directional coupler mechanism and six photodiodes sharing the same waveguide were demonstrated to achieve 92% internal quantum efficiency. Based on these results I developed a design for a segmented waveguide photodetector based on avalanche photodiodes, which paves the way towards integrated optical detectors with PNR capability.

For microwave photonics applications I developed a bias-free GaAsSb/InP type II photodiode. This type of PD achieved high RF output power and large bandwidth and can benefit several applications that require minimized power consumption and reduced circuit complexity.

8.2 High speed photodiodes on silicon nitride

As shown in chapter 5, the bandwidth of heterogeneously integrated photodiodes on silicon nitride reached 20 GHz and was mainly limited by series resistance. A bandwidth of 28 GHz was expected from simulation. Most likely, this is caused by high contact resistance in the P-doped InP contact. In order to achieve higher bandwidth, an InGaAs P-doped contact layer can be added to the epitaxial layer structure. This is because higher doping levels can be achieved in P-doped InGaAs, which enables lower contact resistance. In addition, the structure can be reversed where the N-contact layer becomes the bottom layer as shown in Fig. 8-1. This structure has a reversed epitaxial layer stack of the design shown Fig. 5-16.

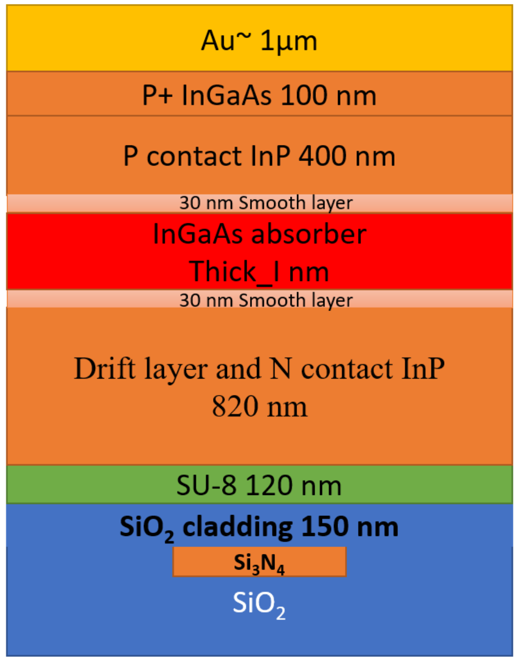

Fig. 8-1 Reversed epitaxial layer stack of Fig. 5-16 with P contact on the top after bonding.

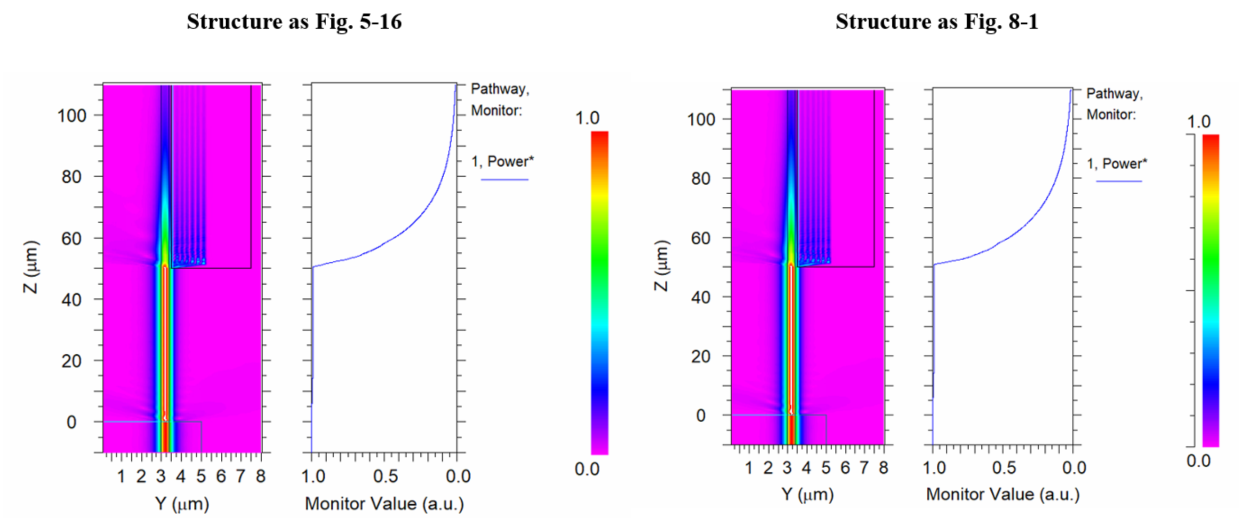

Fig. 8-2 Optical simulation of structures in Fig.5-16 and Fig.8-1.

In Fig. 8-2, I simulated the optical power change along the direction of propagation at 1550 nm. The photodiode starts at z=50 µm. The blue line indicates the total optical power in the simulation region. The decrease of total power is due to absorption in the photodiode. From the plots shown in Fig. 8-2, it can be seen that there is no significant difference by changing the structure upside down. Both devices exhibit strong absorption over 50 μm length which suggests that high responsivity can be achieved in short PDs. However, since higher doping levels can be achieved in both the N-type InP and the P-type InGaAs layers, the contact resistance issue can be mitigated.

8.3 SU-8 planarization on SOI waveguides.

In my work, the bonding process was performed on a flat surface which greatly facilitates SU-8 planarization during spin coating. However, silicon-on-insulator (SOI), the most popular silicon photonic platform, typically is not flat due to the silicon wire waveguides. In order to expand our bonding technique to SOI, this issue can be addressed in two ways. First, use SiO_2 to fill the trenches followed by chemical mechanical polishing (CMP) to achieve a flat surface before bonding. The process is shown in Fig. 8-3.

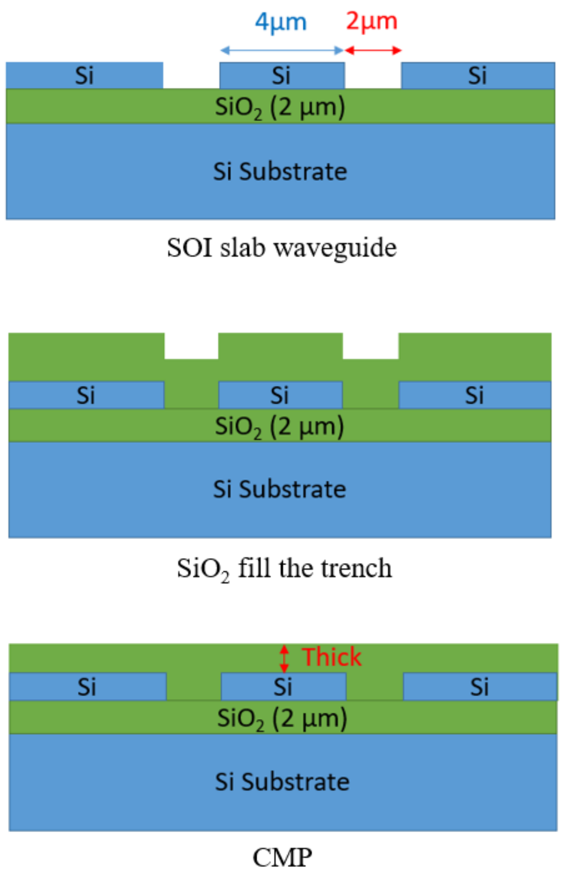

Fig. 8-3 CMP planarization process on SOI.

Another option is to use SU-8 to fill the trench and then do the planarization during the bonding process. In order to have SU-8 evenly filling the waveguide trenches, I have modified the process and added 10 seconds extra spin during time at 500 rpm at the beginning of the SU-8 spin coating process. I also changed the bonding time from 30 min to 70 min in order to make the SU-8 fully filling in the trench. The result is shown in Fig. 8-4, which shows the bonded chip with its cross-section after cleaving. From the SEM image it can be seen that the SU-8 evenly fills the trenches. No bubbles appeared during the bake process after photolithography in over 80% percent of the bonding region. These initial results indicate that our SU-8 bonding can also be applied to SOI slab waveguides that are defined by deep trenches. However, there remains a part of the wafer that is not flat (with bubbles) as shown in Fig. 8-5, which means the bonding process still needs to be optimized including the duration time of spin coating, UV exposure, post-baking and wafer bonding. Future work includes optimization of the bonding process to enable high-performance photodiodes on SOI platform.

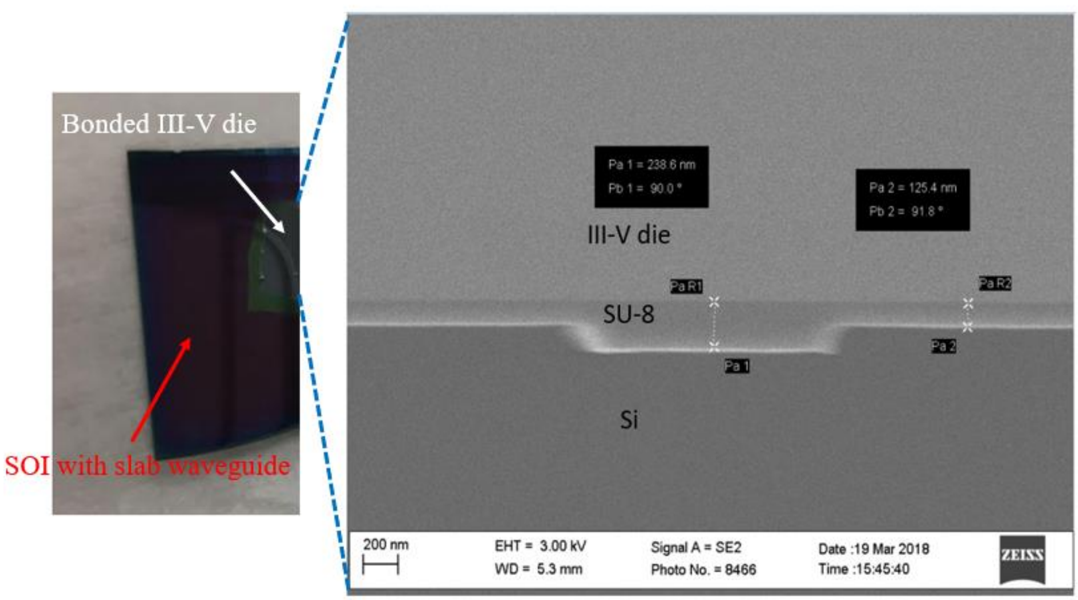

Fig. 8-4 III-V die bonded on Si slab waveguide after cleaving (left), and the SEM image of the cleaving interface (right).

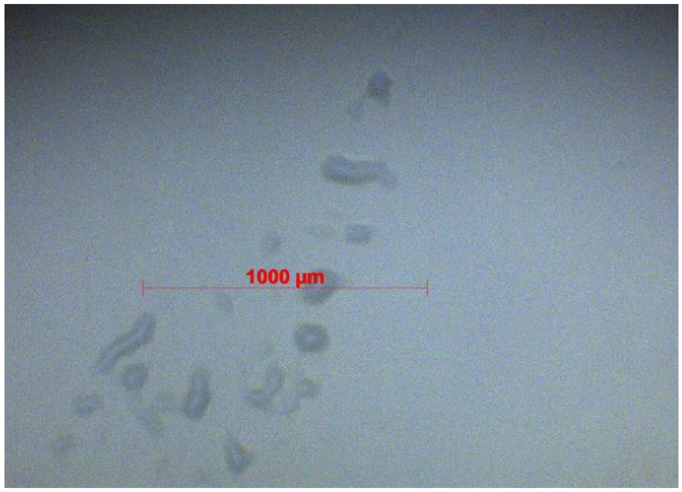

Fig. 8-5 Bubbles appear in some part of wafer.

8.4 Second harmonic generator co-integrated with high responsivity photodiode

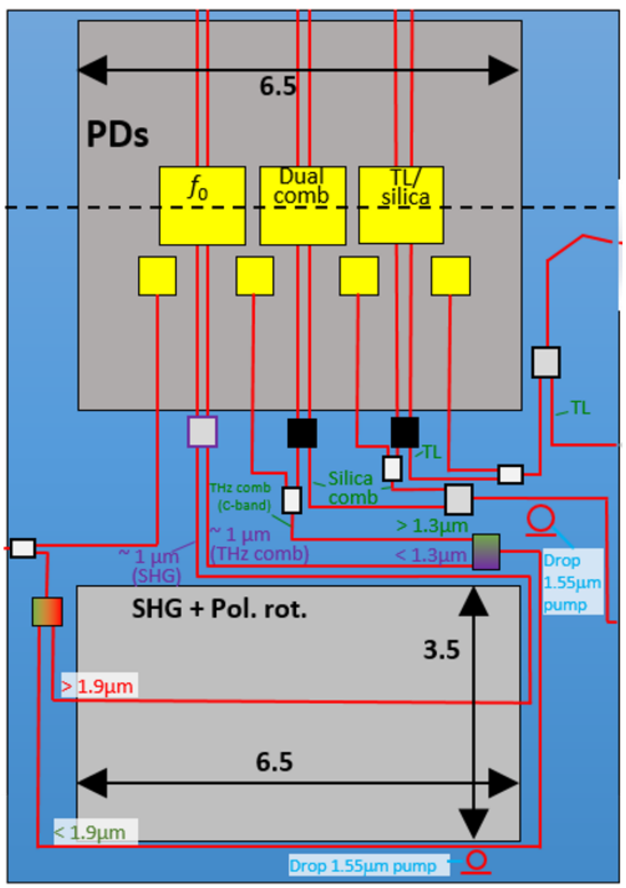

Fig. 8-6 Schematic image of interposer.

As mentioned in chapter 5, high responsivity photodiodes were designed to be integrated with a second harmonic generator (SHG) on a SiN interposer chip, which is shown in Fig. 8-6. There are two bonding windows on the interposer. One is for photodiodes, the other one is for the GaAs-based SHG. There are also some passive optical components on the interposer for filtering and guiding the light. There are three pairs of balanced photodiodes on the chip in order to detect signals from SHG and two other frequency combs.

Our collaborator UCSB first bonded and fabricated their SHG in the SHG bonding window on the chip. Afterwards, I bonded my III-V die in the PDs' bonding window and then fabricated three pairs of high-responsivity balanced photodiodes as shown in Fig. 8-7. Preliminary measurements have been done for the photodiodes on the chip, and indicated a similar performance as described in chapter 5. More measurements of PDs and SHG will be completed in the near future.

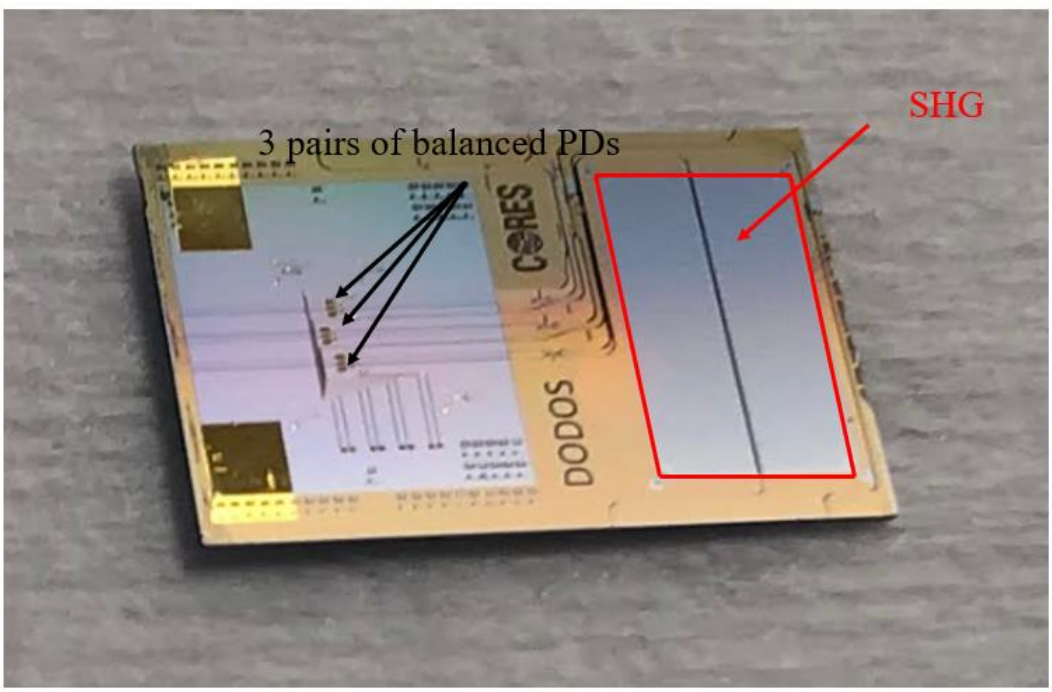

Fig. 8-7 Picture of fabricated interposer with bonded SHG and PDs.

Appendix I (250 nm SU-8)

1. SOI die cleaning:
    a. Spin cleaning by TCE, reagent alcohol and methanone.
    b. Toothpick cleaning of particles.
    c. Spin clean by AZ 400K and methanone.
    d. Check the die under microscope with 20x magnification for any particles in the bonding region.
2. III-V die cleaning:
    a. Spin cleaning by TCE, reagent alcohol and methanone.
    b. Toothpick cleaning of particles.
    c. Spin clean by AZ 400K and methanone.
    d. Check the die under microscope with 20x magnification for any particles on whole die.
3. Surface activation: Put SOI and III-V dies into O_2 plasma chamber for 5 min at 200 W.
4. Spin coating: Spin coat SU-8 6000.5 on SOI die sample at 9000 rpm for 50s.
5. Edge bead removal: Using AZ-EBR to remove edge bead and backside of SOI die.
6. Pre-bake: Bake the SOI die at 110 ℃ for 50s. The die should be attached on a copper carrier by LOR.
7. Cool down: Let SOI die on the copper carrier cool down for 5 min.
8. Exposure: UV-curing of SOI die by MJB-3 for 40s (CH2, 350 nm, 7 mW/cm^2).
9. Out-gassing: Put the III-V die and SOI die side-by-side into bonding machine. Pump down chamber for 30 min out-gassing.
10. Bonding: Attach dies and bond them at 130℃ for 40 min.

11. Cooling down: Set the temperature back to room temperature and take the bonded device out.
12. Cleaning LOR: TCE, reagent alcohol and methanone to remove the LOR.
13. Substrate removal: Use acid HCl: H_2O (3:1) to remove InP substrate.

Appendix II (120 nm SU-8)

1. Silicon nitride die cleaning:
    a. Q-tip swab clean with TCE, reagent alcohol and methanone only one time.
    b. Q-tip swab clean with ethylene glycol and methanone.
    c. Toothpick cleaning of particles.
    d. Check the die under microscope (20x) for any particles in the bonding region.
    e. Repeat steps b-c until no particles can be seen under microscope at 10x.
2. III-V die cleaning:
    a. Q-tip swab clean with TCE, reagent alcohol and methanone only one time.
    b. Q-tip swab clean with ethylene glycol and methanone.
    c. Toothpick cleaning of particles.
    d. Check the die under microscope 20x for any particles in the bonding region.
    e. Repeat steps b-c until no particles can be seen under microscope 10x.
3. Surface activation:
    a. Put silicon nitride die into PECVD for 1min SiO_2 deposition.
    b. Put III-V die into O_2 plasma chamber for 5 min at 200 W.
4. Spin coating: Spin coat SU-8-1 on SOI die sample at 9000 rpm for 40s.
5. Edge bead removal: Using AZ-EBR to remove edge bead and backside of SOI die.
6. Pre-bake: Bake the SOI die at 110 ℃ for 30 s. The die should be put on hot plates directly. (Cool down is not necessary here)
7. Exposure: UVcuring of silicon nitride die by MJB-3 for 9 s (CH2, 350 nm, 7 mW/cm^2).
8. Out-gassing: Put the III-V die and silicon nitride die side by side into bonding machine. Separate them and pump down chamber for 30 min out-gassing.

9. Bonding: Attach two dies and bond them at 130℃ for 40 min.
10. Cooling down: Set the temperature back to room temperature and take the bonded device out.
11. Cleaning LOR: Use TCE, reagent alcohol and methanone to remove the LOR by Q-tip swab.
12. Substrate removal: Use acid HCl: H_2O (3:1) at 60 ℃ to remove InP substrate without any ramps left.

Appendix III (70 nm SU-8)

1. Silicon nitride die cleaning:
    a. Q-tip swab cleaning with TCE, reagent alcohol and methanone only one time.
    b. Q-tip swab clean with ethylene glycol and methanone.
    c. Toothpick cleaning of particles.
    d. Check the die under microscope 20x for any particles in the bonding region.
    e. Repeat steps b-c until no particles can be seen under microscope 10x.
2. III-V die cleaning:
    a. Q-tip swab cleaning with TCE, reagent alcohol and methanone only one time.
    b. Q-tip swab clean with ethylene glycol and methanone.
    c. Toothpick cleaning of particles.
    d. Check the die under microscope 20x for any particles in the bonding region.
    e. Repeat steps b-c until no particles can be seen under microscope 10x.
3. Surface activation:
    a. Put silicon nitride die into O_2 plasma chamber for 4 hours at 200W.
    b. Put III-V die into O_2 plasma chamber for 5 min at 200W.
4. Spin coating: Spin coat SU-8-1 on silicon nitride die at 9000 rpm for 40s.
5. Edge bead removal: Using AZ-EBR to remove edge bead and backside of SOI die.
6. Pre-bake: Bake the silicon nitride die at 110 ℃ for 40s. The die should be put on hot plate directly. (Cool down is not necessary here)
7. Exposure: UV curing of SU-8 on silicon nitride die by MJB-3 for 16 s (CH2, 350 nm, 7 mW/cm^2).

8. Out-gassing: Put the III-V die and silicon nitride die side by side into bonding machine. Separate them and pump down chamber for 35-40 min out-gassing.
9. Bonding: Attach two dies and bond them at 130℃ for 60-90 min.
10. Cooling down: Set the temperature back to room temperature and take the bonded device out.
11. Cleaning LOR: Use TCE, reagent alcohol and methanone to remove the LOR by Q-tip swab.
12. Substrate removal: Use acid HCl: H_2O (3:1) at 40-45 ℃ to remove InP substrate without any ramp left.

Appendix IV SIMS result of zero-bias wafer

Epi Design

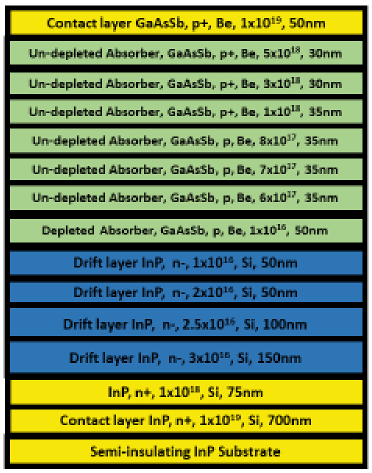

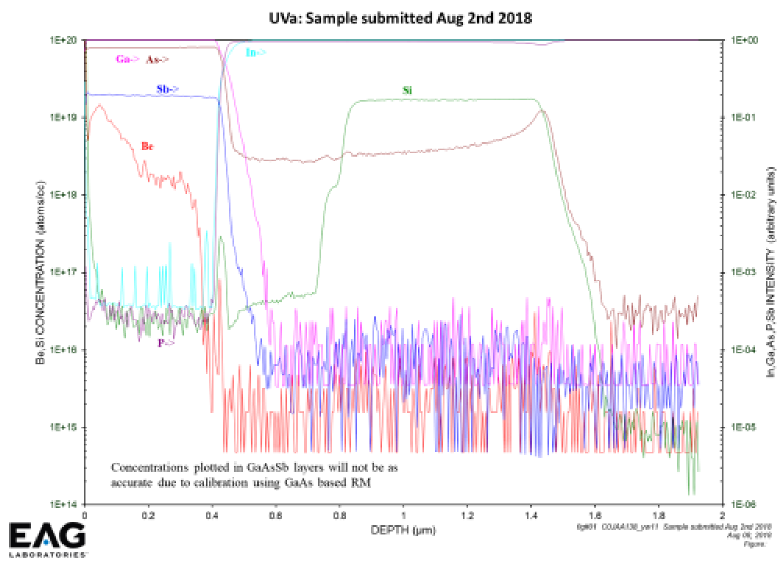

List of Publications

[1] **<u>Q. Yu</u>**, J. Gao, N. Ye, B. Chen, K. Sun, L. Xie, K. Srinivasan, M. Zervas, G. Navickaite, M. Geiselmann, A. Beling. "Heterogeneous Photodiodes on Silicon Nitride Waveguides with 20 GHz Bandwidth." In *Optical Fiber Communication Conference*, pp. W4G-1. Optical Society of America, 2020.

[2] F. Yu, K. Sun, **<u>Q. Yu</u>**, and A. Beling. "Zero-Bias High-Speed Evanescently Coupled Waveguide Type-II UTC Photodiode." In *Optical Fiber Communication Conference*, pp. W4G-6. Optical Society of America, 2020.

[3] N. Rajveer, C. Chang, **<u>Q. Yu</u>**, A. Beling, and O. Pfister. "Photon-number-resolving segmented detectors based on single-photon avalanche-photodiodes." *Optics Express* 28, no. 3 (2020): 3660-3675.

[4] V. Ashwin, **<u>Q. Yu</u>**, Y. Du, and B. Ovenstone. "Surface condensation sensor board for damp heat chamber." *Review of Scientific Instruments* 90, no. 9 (2019): 095102.

[5] **<u>Q. Yu</u>**, N. Ye, J. Gao, K. Sun, L. Xie, K. Srinivasan, M. Zervas, G. Navickaite, M. Geiselmann, and A. Beling. "High-Responsivity Photodiodes Heterogeneously Integrated on Silicon Nitride Waveguides." In *Integrated Photonics Research, Silicon and Nanophotonics*, pp. IW3A-5. Optical Society of America, 2019.

[6] A. Beling, T. Tzu, J. Gao, J. Morgan, K. Sun, N. Ye, B. Tossoun, F. Yu, **<u>Q. Yu</u>**, "High-Speed Integrated Photodiodes," *2019 24th OptoElectronics and Communications Conference (OECC) and 2019 International Conference on Photonics in Switching and Computing (PSC)*, Fukuoka, Japan, 2019, pp. 1-3.

[7] A. Beling, J. Morgan, K. Sun and **<u>Q. Yu</u>**, "High Power Integrated 100 GHz Photodetectors," *2018 International Topical Meeting on Microwave Photonics (MWP)*, Toulouse, 2018, pp. 1-4.

[8] J. Zang, X. Xie, **<u>Q. Yu</u>**, Z., A. Beling, and J. C. Campbell. "Reduction of Amplitude-to-Phase Conversion in Charge-Compensated Modified Unitraveling Carrier Photodiodes." *Journal of Lightwave Technology* 36, no. 22 (2018): 5218-5223.

[9] Z. Yang, **<u>Q. Yu</u>**, J. Zang, J. C. Campbell, and A. Beling. "Phase-modulated analog photonic link with a high-power high-linearity photodiode." *Journal of Lightwave Technology* 36, no. 18 (2018): 3805-3814.

[10] **<u>Q. Yu</u>**, Z. Wang, K. Sun, F. Yu, J. Zang, J. C. Campbell, and A. Beling. "Zero-Bias GaAsSb/InP Photodiode with 40 GHz Bandwidth." In 2018 IEEE Photonics Conference (IPC), pp. 1-2. IEEE.

[11] **<u>Q. Yu</u>**, K. Sun, Q. Li, and A. Beling. "Segmented waveguide photodetector with 90% quantum efficiency." *Optics express* 26, no. 10 (2018): 12499-12505.

[12] **<u>Q. Yu</u>**, Y. Wang, L. Xie, S. Nadri, K. Sun, J. Zang, Q. Li, R. M. Weikle, and A. Beling. "High-performance InGaAs/InP photodiodes on silicon using low-temperature wafer-bonding." In *CLEO: Science and Innovations*, pp. SM2I-1. Optical Society of America, 2018.

[13] K. Sun, R. Costanzo, T. Tzu, **<u>Q. Yu</u>**, S. M. Bowers, and A. Beling. "Ge-on-Si waveguide photodiode array for high-power applications." In *2018 IEEE Photonics Conference (IPC)*, pp. 1-2. IEEE, 2018.

[14] Q. Li. Sun, K. Li, **<u>Q. Yu</u>**, P. Runge, W. Ebert, A. Beling, and J. C. Campbell. "High-power evanescently coupled waveguide MUTC photodiode with> 105-GHz bandwidth." *Journal of Lightwave Technology* 35, no. 21 (2017): 4752-4757.

[15] Q. Li, K. Sun, K. Li, **<u>Q. Yu</u>**, J. Zang, Z. Wang, P. Runge, W. Ebert, A. Beling, and J. C. Campbell. "Waveguide-integrated high-speed and high-power photodiode with> 105 GHz bandwidth." In *2017 IEEE Photonics Conference (IPC)*, pp. 49-50. IEEE, 2017.

[16] Ye. W, Z. Wang, **<u>Q. Yu</u>**, X. Xie, T. Posavitz, M. Jacob-Mitos, Anand Ramaswamy, Erik J. Norberg, Gregory A. Fish, and Andreas Beling. "High-power photodiodes with 65 GHz bandwidth heterogeneously integrated onto silicon-on-insulator nano-waveguides." *IEEE Journal of Selected Topics in Quantum Electronics* 24, no. 2 (2017): 1-6.

[17] Z. Yang, **<u>Q. Yu</u>**, X. Xie, P. Yao, C. Schuetz, J. C. Campbell, and A. Beling. "High-gain phase modulated analog photonic link using high-power balanced photodiodes." In *Optical Fiber Communication Conference*, pp. Th1A-5. Optical Society of America, 2017.

[18] Q. Li, K Sun, K Li, **<u>Q. Yu</u>**, P. Runge, W. Ebert, A. Beling, and J. C. Campbell. "High-power waveguide MUTC photodiode with 70 GHz bandwidth." In *2016 IEEE International Topical Meeting on Microwave Photonics (MWP)*, pp. 225-228. IEEE, 2016.

[19] Wang, Y, **<u>Q. Yu</u>**, X. Xie, M. Mitos, A. Ramaswamy, E. Norberg, G. Fish, and A. Beling. "High-efficiency heterogeneously integrated photodiodes on SOI nano-waveguides." In *2016 IEEE Photonics Conference (IPC)*, pp. 254-255. IEEE, 2016.